5-2021

# Characterization of GeSn Semiconductors for Optoelectronic Devices

Hryhorii Stanchu
*University of Arkansas, Fayetteville*

Characterization of GeSn Semiconductors for Optoelectronic Devices

A dissertation submitted in partial fulfillment
of the requirements for the degree of
Doctor of Philosophy in Microelectronics-Photonics

by

Hryhorii Stanchu
Chernivtsi National University
Bachelor of Science in Physics, 2011
Chernivtsi National University
Master of Science in Condensed Matter Physics, 2012

May 2021
University of Arkansas

This dissertation is approved for recommendation to the Graduate Council.

Gregory J. Salamo, Ph.D.
Dissertation Director

Shui-Qing Yu, Ph.D.
Committee Member

Huaxiang Fu, Ph.D.
Committee Member

Min Zou, Ph.D.
Committee Member

Rick Wise, Ph.D.
Ex-Officio Member

The following signatories attest that all software used in this dissertation was legally licensed for use by Hryhorii Stanchu for research purposes and publication.

| | |
|---|---|
| Mr. Hryhorii Stanchu, Student | Dr. Gregory Salamo, Dissertation Director |

This dissertation was submitted to http://www.turnitin.com for plagiarism review by the TurnItIn company's software. The signatories have examined the report on this dissertation that was returned by TurnItIn and attest that, in their opinion, the items highlighted by the software are incidental to common usage and are not plagiarized material.

| | |
|---|---|
| Dr. Rick Wise, Program Director | Dr. Gregory Salamo, Dissertation Director |

Abstract

Germanium-tin alloys with Sn compositions higher than 8 at. % to 10 at. % have recently attracted significant interest as a group IV semiconductor that is ideal for active photonics on a Si substrate. The interest is due to the fact that while at a few percent of Sn, GeSn is an indirect bandgap semiconductor, at about 8 to 10 at. % Sn, GeSn transitions to a direct bandgap semiconductor. This is at first surprising since the solid solubility of Sn in Ge under equilibrium growth conditions is limited to only about 1 at. %. However, under non-equilibrium growth conditions, Sn concentrations in GeSn of more than 20 at. % are reported. At these high concentrations several problems arise due to severe lattice mismatch and chemistry that can have serious impact on the optical quality and stability of GeSn optical devices. As a result, it is important to understand and perhaps control the growth of GeSn semiconductors containing such high Sn concentrations. This requires an investigation of the measurement, interplay, and role of composition, strain, defects, structure, segregation, and precipitation in GeSn/Ge/Si(001) heterostructures and is the subject of this dissertation.

More specifically, in this study, the experimental and theoretical x-ray diffraction analysis is shown as a reliable technique for non-destructive and precise characterization of composition, strain, defects, structure, segregation, and precipitation in GeSn. As a result, under an annealing treatment of GeSn/Ge/Si(001) heterostructures, the interplay of these properties was correlated with the stability and optical quality. For example, the density of misfit dislocations of $\sim 2 \times 10^5$ $cm^{-1}$ in the as-grown GeSn layers was shown to be correlated to the onset of Sn segregation. These results provide insight that can be used for the growth of metastable GeSn alloys with improved Sn content, thermal stability, and optical quality.

Acknowledgements

First of all, I would like to express my sincere gratitude to my scientific advisor Professor Gregory J. Salamo for his support during the Ph.D. study and whose invaluable critique and advices shaped my scientific approach. I would also like to thank Dr. Rick Wise for accepting me into the Microelectronics-Photonics program, as well as for his guidance that helped to complete this journey.

I appreciate the help, collaboration, and mentoring of Dr. Andrian Kuchuk and Dr. Yuriy Mazur at all stages during the Ph.D. period and beyond. I am grateful to the members of my dissertation commeetee, Dr. Fisher Yu, Dr. Huaxiang Fu, and Dr. Min Zou, for their time, patience, and contributions. Moreover, I acknowledge the help of Dr. Yurii Maidaniuk and Mohammad Zamani Alavijeh for helpful advices on TEM sample preparation and AFM measurements. Special thanks go to Dr. Mourad Benamara for TEM, SEM, and EDX measurements, Oluwatobi Olorunsola for PL measurements, and Fernando Maia de Oliveira for Raman measurements. I would like to appreciate the help of Krishna Pandey with the setup of annealing experiments.

I am grateful to Febriyanti Lestari for inspiration and motivation, and to my family for the longstanding support and encouragement all over the years.

I want to acknowledge the financial support from the Institute of Nanoscale Science and Engineering, University of Arkansas, and the Multidisciplinary University Research Initiatives (MURI) Program through the U.S. Air Force Office of Scientific Research (AFOSR) grant no. FA9550-19-1-0341.

Table of Contents

List of Figures

List of Tables

# Chapter 1: Introduction

## 1.1 Background

Silicon (Si), and to a lesser extent germanium (Ge), are the central semiconductors for electronics today. Yet, modern photonic devices are based on a variety of different compound semiconductors, each of which is chosen to provide the ultimate performance for specific applications [1]. Thus, the discrete devices are manufactured by utilizing different fabrication facilities, which makes their integration with the established silicon platform technologically difficult [2], [3]. For example, heterogeneous packaging typically leads to a lower level of device performance as well as an elevated final cost per device. In this respect, germanium-tin (GeSn) alloy semiconductors have attracted considerable attention over the recent years as prospective materials for CMOS (complementary metal-oxide-semiconductor) compatible group IV photonic and electronic devices for monolithic integration on Si substrate. In particular, the tunable bandgap of GeSn is of much interest in applications within the near- and mid-infrared wavelength range. On top of that, GeSn is considered as an attractive channel material for field-effect transistors due to the potential of increasing the electron and hole mobilities in Ge by strain management and by alloying with Sn [4].

The poor light-emitting in Ge and Si is due to their indirect bandgap nature [5]–[7]. For example, the electronic band structure of bulk Si, Ge, and α-Sn are compared in Figure 1.1 [8]. Here it can be seen that the conduction bandgap minima are seen at the X and L points of the Brillouin zone for Si and Ge, respectively. Because of the slight overlapping of the conduction and valence bands at the Γ point, α-Sn is considered a negative direct bandgap material. Moreover, while Si is a strongly indirect bandgap semiconductor, the Γ valley in Ge is only

~0.14 eV above the minimum in the L valley.

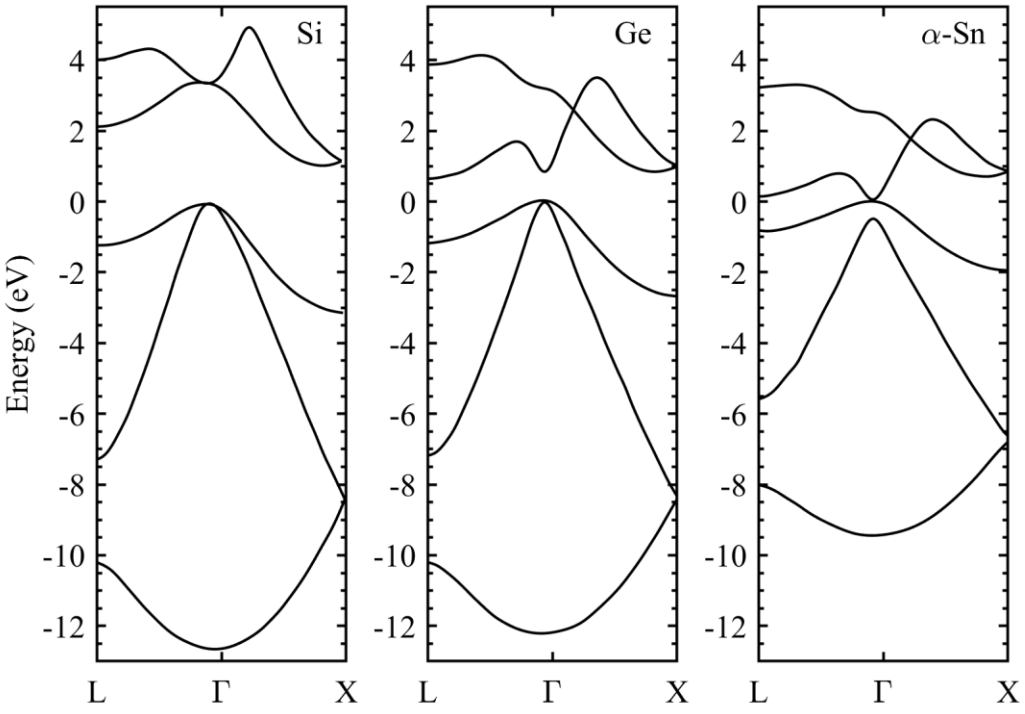


Figure 1.1. Electronic band structure of group IV semiconductors Si, Ge, and α-Sn [8].

The processes of luminescence emission from the semiconductors with direct and indirect bandgaps are shown in Figure 1.2. For a direct bandgap semiconductor in Figure 1.2a, electrons in the conduction band and holes in the valence can be found occupying states with the same $\boldsymbol{k}$ in the momentum space. The radiative electron-hole recombination does not require momentum change, as is illustrated with a downward pointing arrow. Typically, the radiative lifetime is of the order of $10^{-9}$ s [9]. For an indirect bandgap semiconductor in Figure 1.2b, the conduction band minimum and the valence band maximum appear at different crystal momentum $\boldsymbol{k}$, so that the excited electrons and holes in the conduction and valence bands, respectively, have different momentum. Since the photon momentum is negligibly small as compared to that of an electron, the photon emission would not compensate for the momentum mismatch of an electron-hole pair,

thus, prohibiting their radiative recombination. Accordingly, in an indirect bandgap semiconductor, recombination of an electron-hole pair involves emission or absorption of a phonon, as illustrated with a leftward pointing arrow in Figure 1.2b [9], [10]. In this case, radiative recombination is a second-order process with an overall lifetime of the order of milliseconds. Practically, this reduces the radiative recombination rate, so that other non-radiative processes such as energy transfer to impurities or defects may dominate.

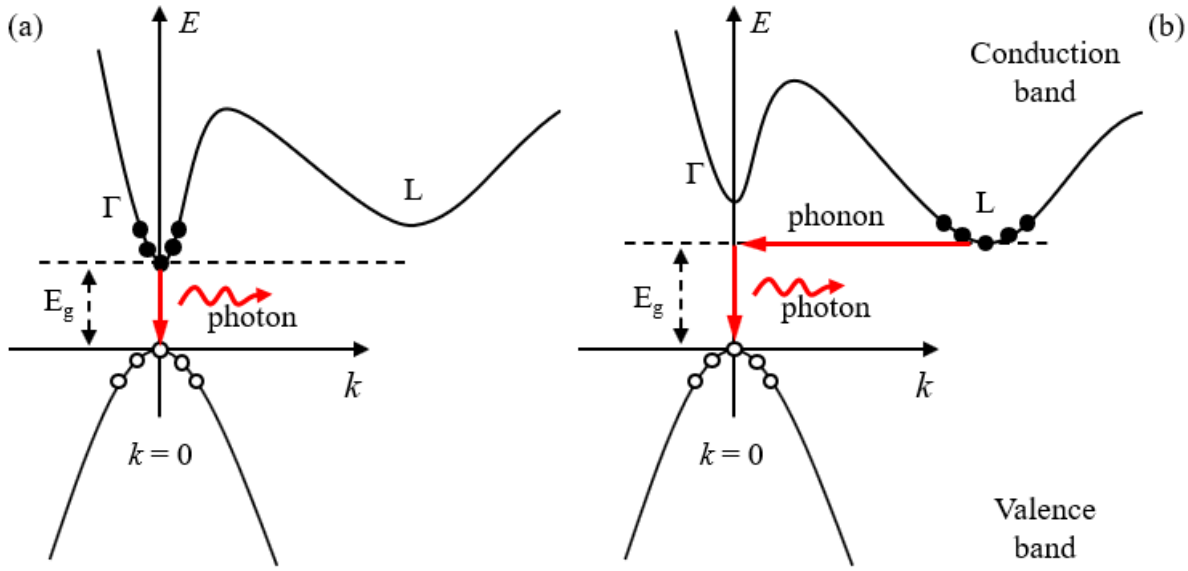


Figure 1.2. Schematic illustration of the band structure and the luminescence process for a direct (a) and indirect (b) bandgap semiconductor in energy-momentum (*E*-*k*) space. The filled and empty circles denote the excited electrons and holes in the conduction and valence band, respectively. $E_g$ is the bandgap energy.

Due to the small L-Γ energy separation in Ge, an indirect-to-direct crossover can be achieved under specific conditions [11], [12]. In particular, the bandgap energy is commonly reduced by using heavy *n*-type doping and/or biaxial tensile strain [13]. Specifically, since the bandgap in semiconductors is dependent on the lattice parameter, the introduction of tensile strain expectedly narrows the energy gap [2]. Moreover, the applied tensile strain also shrinks the energy separation between the L and Γ valley, which is in agreement with the larger value of

the deformation potential constant of the conduction band in Ge at the Γ point ($a_\Gamma$ = -8.24 eV) as opposed to that at the L point ($a_L$ = -1.54 eV) [14]. The magnitude of tensile strain that permits to level the Γ and L valleys is shown to be of the order of ~2% [4], [15], which practically is difficult to achieve due to the early plastic strain relaxation with increasing film thickness. Accordingly, this imposes a design limit for the Ge-based devices.

For moderate tensile strain, the donor concentrations of the order $10^{18}$ - $10^{20}$ $cm^{-3}$ are employed to raise the position of the Fermi level, which allows filling with electrons at the higher energy levels in the conduction band [16]. Subsequently, for not very large L-Γ separation, more electrons are allowed to populate the Γ valley, which in turn contributes to stronger direct bandgap radiative emission. Nonetheless, a disadvantage of heavy doping for light-emitting devices is related to the incorporation of large densities of impurities and crystalline defects, which generally leads to an increased recombination rate via nonradiative processes [17].

Another major limitation of the Ge-based devices is related to the narrow operating wavelength region that is restricted by the tunability of the direct bandgap within the 1.3-1.6 μm range [18], [19]. The device responsivity is drastically reduced at larger wavelengths at which indirect bandgap absorption/emission is dominating. In contrast, the compounds of group III-V (such as GaAs, InAs, etc.) and their alloys (such as InGaAs, InGaAsP, etc.) are the most mature direct bandgap material systems, which among others provide a better wavelength tunability by engineering the alloy composition [20] (Figure 1.3). However, the III-V system suffers from a higher substrate cost, while the heterogeneous integration of III-V devices on Si is complex due to the large lattice mismatch of the lattice parameters and the coefficients of thermal expansion. Additionally, the growth of polar III-V materials on non-polar Si or Ge often is accompanied by

the formation of antiphase domains (APD), which are known as charged defects [21]. Moreover, during the conventional device processing, the group III-V atoms may diffuse into the Si substrate, where these are acting as acceptor/donor species.

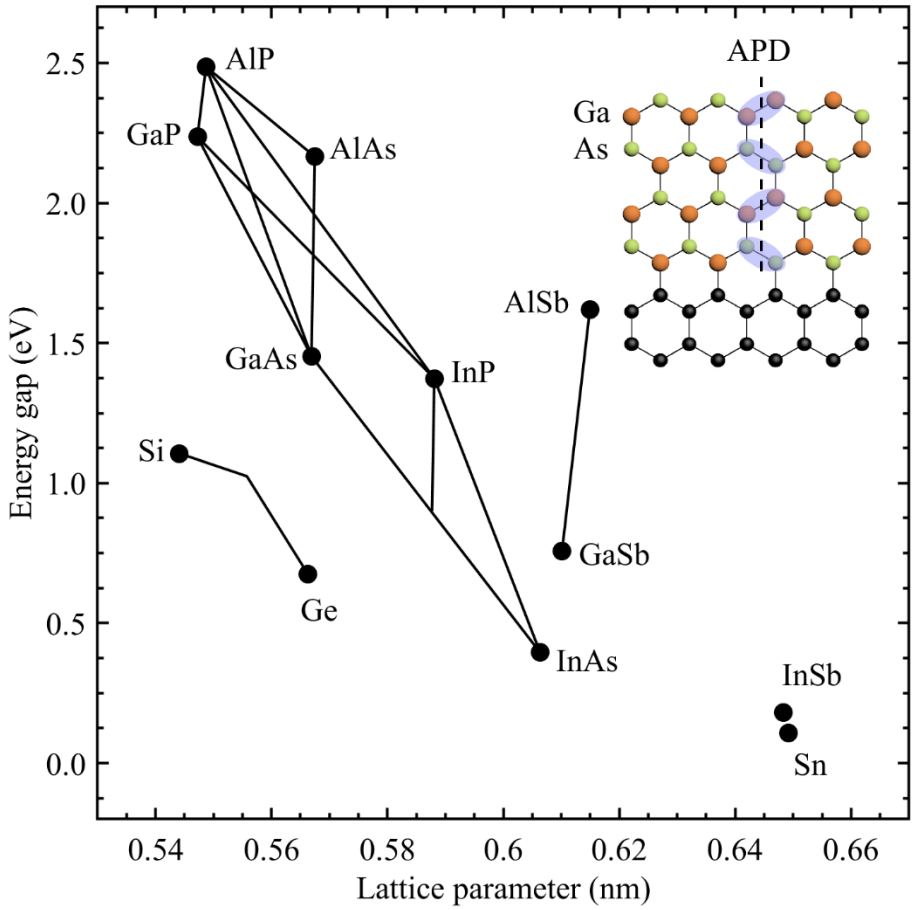


Figure 1.3. The bandgap energy as a function of lattice parameter for group III-V compounds and their alloys (solid lines) in comparison with group IV elements Si, Ge, and Sn [22]. Inset shows a schematic of the APD in the GaAs lattice grown on Si substrate.

Therefore, alloying Sn into Ge emerged as the most promising approach for achieving the indirect-to-direct bandgap transition in Ge, which also aids to extend the infrared windows far above 1.6 μm. For instance, the Sn concentration for an indirect-to-direct bandgap transition for unstrained GeSn is as low as 6% [23], which corresponds to the weighted sum of the bandgap

values of Ge and α-Sn at the Γ point (Table 1.1). The Sn molar fraction required for the direct transition increases with the compressive strain and is reported to be about 8-10% [24].

Table 1.1. Direct and indirect bandgaps for Ge, Sn, and Si [4], [25].

| Material | Γ (eV) | L (eV) |
|---|---|---|
| Ge | 0.90 | 0.76 |
| α-Sn | -0.42 | 0.14 |
| Si | 3.40 | 1.10 |

From the point of view of material growth, the preparation of high-quality GeSn alloys is subjected to several challenges. In particular, the semiconducting diamond cubic α-Sn phase is stable for temperatures below 13.2 °C. Therefore, an allotropic phase transition to the metallic β-Sn (tetragonal crystal structure) is likely to occur at higher temperatures [26], [27]. Moreover, the experimental and theoretical investigations of the Ge-Sn equilibrium system revealed a large miscibility gap [28], [29].

The temperature/composition equilibrium phase diagram of the binary Ge-Sn system can be seen in Figure 1.4. In particular, the diagram shows the phases that are in equilibrium at specific temperatures and compositions. As can be seen, the GeSn solid solutions are stable for Sn compositions below 1.1 at. % or above 99.4 at. %. The solid solubility is limited due to the different crystal structures of Ge (diamond cubic) and β-Sn (tetragonal) as well as the difference between the atomic radius of the two elements. The Sn composition lower than 1.1 at. % is far below the required Sn content of a direct bandgap GeSn alloy, while the miscibility gap sets a limit for alloy engineering.

Additionally, the Ge-Sn system shows a low eutectic temperature (231.1 °C). Moreover, this temperature is close to the melting point of Sn (232 °C), which in practice suggests unstable

thermal properties for the GeSn solid solutions. Therefore, this set a limitation for the growth and material processing temperatures [30].

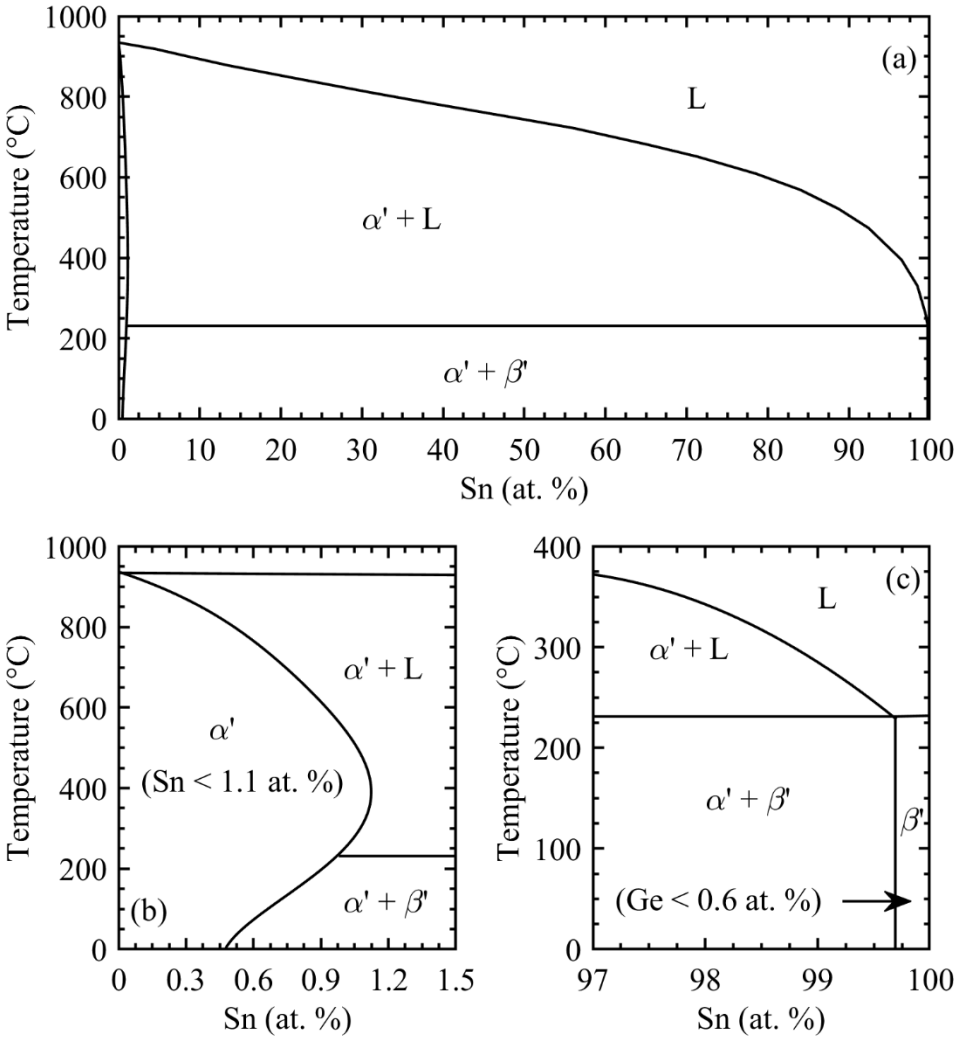


Figure 1.4. Equilibrium phase diagram of the binary Ge-Sn system (a) [28], [30]. (b) and (c) show enlarged views of the phase diagram near the Ge-rich and Sn-rich sides. α′ and β′ denote the stable $Ge_{1-x}Sn_x$ solid phases; L stands for the liquid phase.

Germanium-tin alloys with high Sn content are typically grown under non-equilibrium conditions, such as by molecular beam epitaxy (MBE) and chemical vapor deposition (CVD) [31], [32]. Moreover, since GeSn alloys are prone to segregation and Sn precipitation, the growth is restricted to relatively low temperatures. However, it is well recognized that due to the

large difference of atomic radius between Sn and Ge, inclusion of Sn atoms into Ge matrix is significantly suppressed even at non-equilibrium growth conditions [33]. At relatively high growth temperatures, Sn atoms tend to segregate on the sample surface or within the layer volume forming Sn-rich precipitates [34]. Also, the mismatch between the crystal lattice of Sn, Ge, and Si is extremely high [35]. The increase of epitaxial layer thickness gives rise to a high density of structural defects. Therefore, a chemically stable GeSn alloy with high Sn composition is difficult to achieve.

Even though, the landscape of Group IV photonics includes waveguides, modulators, photodetectors, as well as laser sources [36]. Among the recently demonstrated GeSn-based photonic devices are GeSn p-i-n near-infrared photodetectors [37], short-wave infrared GeSn/SiGeSn multi-quantum-well (MQW) light-emitting diodes (LEDs) [38], infrared GeSn/Ge p-n heterojunction diodes [39], high-speed optical modulators, high-efficiency solar cells [40], and the first demonstration of optically pumped lasing at low temperatures using direct bandgap GeSn alloys [36].

## 1.2 Crystal structure

The atomic arrangement in a crystal is determined by the valence electron configuration of constituent atoms. Group IV elements Si, Ge, and Sn are known as tetrahedral solids since their four valence electrons participate in electron sharing with four adjacent atoms, which results in four covalent bonds that form a tetrahedron shape around the central atom [41]. The schematic illustration of the electron pairs sharing for the group IV elements can be seen in Figure 1.5. The strength of the covalent structure generally decreases down the column of group IV due to the increasing atomic radius and thus, the reducing interatomic potential. For example,

the reported values for the bond energy of Si, Ge, and Sn are -13.306, -12.273, and -9.322 eV respectively [42].

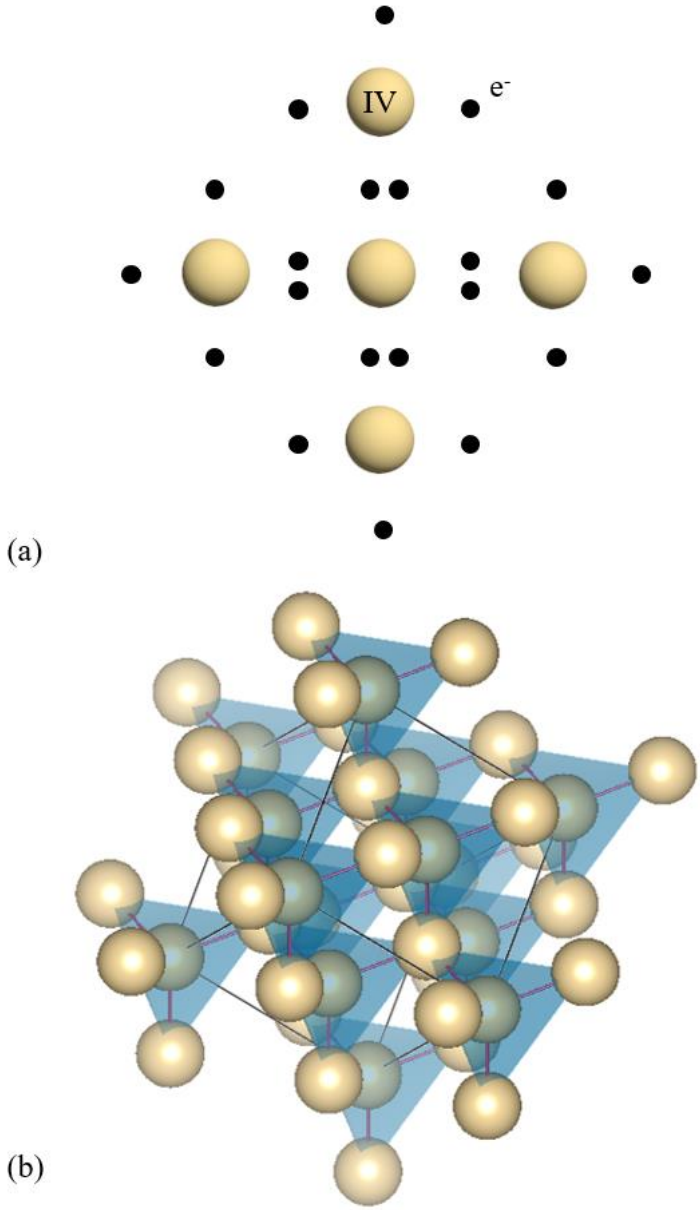


Figure 1.5. The Lewis dot structure (a) and the stick and ball model (b) showing the valence electron configuration and the covalent bonding in solids of group IV (the atomic radius and the bond length are shown not to scale).

The tetrahedral arrangement of the group IV atoms in a solid is the foundation of the diamond crystal structure. The unit cell of the diamond lattice is described by two basis atoms

each defining the basis of two interpenetrating face-centered cubic (fcc) Bravais lattices displaced along the body diagonal by a quarter of length [43], [44] (Figure 1.6a). In fractions of the unit cell, the two basis atoms are located at $[0,0,0]$ and $\left[\frac{1}{4},\frac{1}{4},\frac{1}{4}\right]$, respectively. For the alloys of group IV (e.g. GeSn, SiGe), the two fcc contain more than one sort of atoms and thus, the structure is called zinc blende. The eight lattice points that make the diamond and zinc-blende unit cells are defined by the following set of fractional coordinates [45]: $[0,0,0]$, $\left[0,\frac{1}{2},\frac{1}{2}\right]$, $\left[\frac{1}{2},0,\frac{1}{2}\right]$, $\left[\frac{1}{2},\frac{1}{2},0\right]$, $\left[\frac{1}{4},\frac{1}{4},\frac{1}{4}\right]$, $\left[\frac{1}{4},\frac{3}{4},\frac{3}{4}\right]$, $\left[\frac{3}{4},\frac{1}{4},\frac{3}{4}\right]$, and $\left[\frac{3}{4},\frac{3}{4},\frac{1}{4}\right]$. For instance, Figure 1.6b shows the top view on the (001) plane. Here, the fractions above the lattice points denote their height in terms of unit cell dimensions. The volume of the unit cell increases from Si to Ge to α-Sn due to the increasing atomic radius, $R$. The lattice constants, $a$, and the atomic radii for Si, Ge, and α-Sn are compared in Table 1.2.

Table 1.2. The lattice parameter and atomic radius for Si, Ge, and α-Sn [46].

| Material | Lattice constant (nm) | Atomic radius (nm) |
|---|---|---|
| α-Sn | 0.6489 | 0.145 |
| Ge | 0.5658 | 0.125 |
| Si | 0.5431 | 0.111 |

The principal directions in the cubic lattice are shown in Figure 1.6c. The two atoms are most closely separated along the $\langle 110 \rangle$ direction, which is given by the lattice vector $a/2\langle 110 \rangle$. Atoms in the $\{111\}$ planes are the most close-packed, with a six-fold stacking sequence AaBbCc as shown in Figure 1.6d, where atoms of adjacent layers such as Aa, Bb, and Cc are located directly over each other [47].

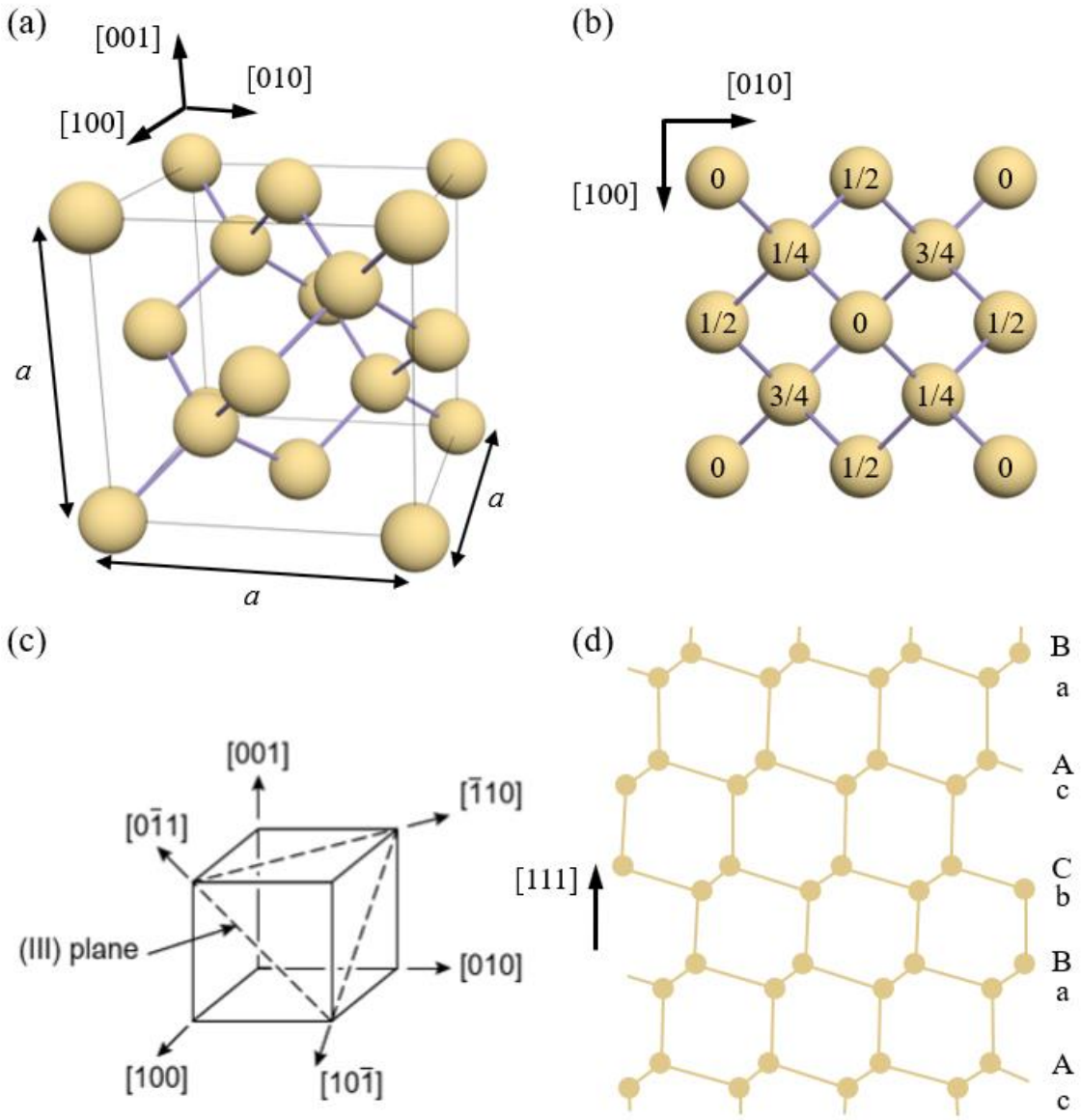


Figure 1.6. (a) Schematic illustration of the cubic unit cell. The atoms in the lattice are shown as spheres, and the relative dimensions of the cube edge and sphere radius are shown as a 2:1 proportion. (b) Projection on the (001) plane with the fractions denoting the height of the atoms above the base [44], [47].

## 1.3 Lattice parameter of the GeSn alloy

The substitution of Sn atoms with the larger atomic radius (Table 1.2) into the Ge lattice results in a sufficient increase of the unit cell volume. The equilibrium lattice parameter, $a_0$, for

a binary $Ge_{1-x}Sn_x$ compound is a function of Sn content, $x$. The value of $a_0$ can be simply estimated as a linear interpolation (Vegard's law) between the Ge and α-Sn bulk lattice constants with the bowing parameter correction as follows [48],

$$a_0 = a_{Sn}x + a_{Ge}(1-x) + bx(1-x) \qquad \text{(Equation 1.1)}$$

where $a_{Sn}$ and $a_{Ge}$ are the bulk lattice constants of α-Sn and Ge, respectively, and $b$ is the bowing parameter that accounts for the deviation from linearity. The magnitude and sign of the bowing parameter for an alloy are commonly correlated with the atomic radius mismatch and the electronegativity of the constituent atoms [49]. The reported values of $b$ for GeSn alloys fluctuate in a wide range from 0.0041 to 0.065 nm [50]. The disagreement is often attributed to an erroneous evaluation of strain and composition in the GeSn layers. The recent theoretical estimation of the bowing parameter demonstrated that the magnitude of $b$ for GeSn alloys can be as low as 0.0048 nm [49], which was later supported by experimental measurements ($b = 0.0041$ nm) [50].

The evolution of the equilibrium lattice parameter of a GeSn alloy versus Sn composition is compared in Figure 1.7a for several values of $b$. The departure of $a_0$ from the linear relationship expectedly increases with the Sn composition, reaching the highest deviation at $x$ = 50 at. %. Figure 1.7b illustrates a negligible deviation $\Delta a_0 = a_0^b - a_0^{b=0}$ from Vegard's law ($10^{-3}$ - $10^{-4}$ nm) when the Sn content is below 20 at. %, which can be considered as an upper limit for $Ge_{1-x}Sn_x$/Ge/Si epitaxy. Additionally, the value of $\Delta a_0$ is comparable with the accuracy ($10^{-4}$ - $10^{-5}$ nm) of the lattice parameter determination when using the laboratory x-ray diffraction instrument. Therefore, the bowing parameter in Equation 1.1 has only a minor contribution to the determination of strain and composition in the GeSn/Ge epitaxial layers and, therefore, the bowing correction to Vegard's law is often omitted.

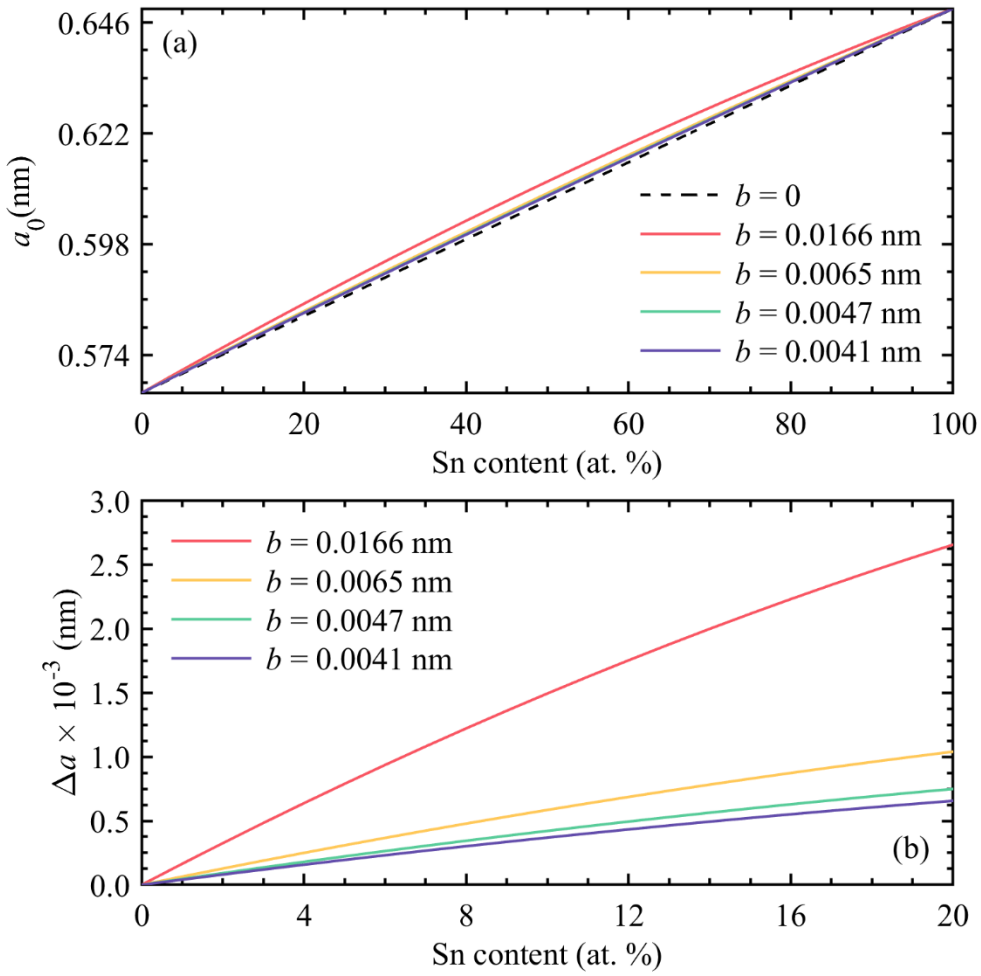


Figure 1.7. (a) The evolution of the equilibrium lattice parameter for a GeSn alloy as a function of Sn content calculated using different values of the bowing parameter. (b) The deviation of the equilibrium lattice parameter of GeSn from the linear relationship due to the bowing correction.

## 1.4 Lattice mismatch and critical thickness

Epitaxial growth of thin-film semiconductors on dissimilar substrates is an important technique that allows a combination of different materials for engineering their optical and electronic properties [51]. For instance, the energy gap of a semiconductor can be modified by the control of film thickness, strain, and alloy composition, which is permitted by advanced growth techniques such as MBE and CVD.

For materials with similar crystal structures, the lattice mismatch is the major source of

crystalline defects as well as the reason for epitaxial growth failure. The concept of a mismatched film-substrate heterosystem is illustrated in Figure 1.8. To begin with, Figure 1.8a compares the crystal lattices of a thin film with that of an infinitely thick substrate in the bulk state. The lattice parameters of the film and substrates are denoted by $a_0$ and $a_s$, respectively, and so that $a_0 > a_s$. Provided that the lattice mismatch is not very high and the thickness of the epitaxial film is much smaller as compared with the substrate thickness, the epitaxial film can undergo elastic deformation at the initial stage of growth to fit with the lattice parameter of the rigid substrate in the plane of the interface, as shown in Figure 1.8b.

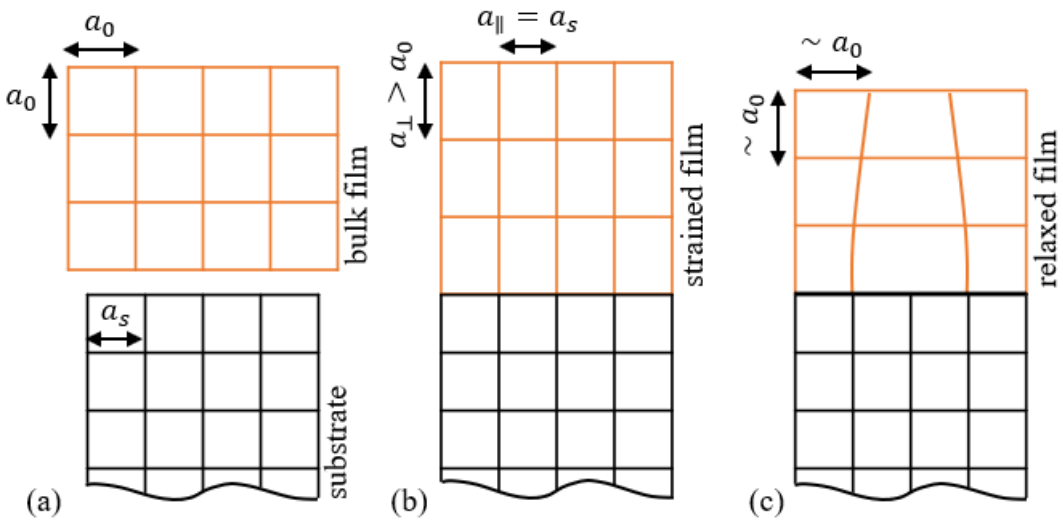


Figure 1.8. Schematic illustration of the crystal lattice of bulk (a), strained (b), and plastically relaxed (c) epitaxial film.

As the film thickness increases during the growth, the elastic energy of deformation, $E_f$, builds up by the following expression [52]

$$E_f = \frac{2\mu(1+\nu)}{(1-\nu)} hf^2 \qquad \text{(Equation 1.2)}$$

where $\mu$ is the shear modulus, $\nu$ is the Poisson's ratio, $h$ is the film thickness, and $f = 100\% \times (a_0 - a_s)/a_s$ is the lattice mismatch. A transition to the relaxed film configuration is

initiated at the critical thickness, $h_c$, at which the nucleation of misfit dislocations (MDs) is favorable. Upon further growth, the multiplication of MDs gradually reduces the mismatch strain and thus, minimizes the elastic strain energy $E_f$. Accordingly, the lattice parameter of the epitaxial film relaxes toward the bulk value as schematically shown in Figure 1.8c.

The critical thickness of epitaxial films on mismatched substrates was previously calculated using different approaches [53]–[57], among which the force and energy balance considerations proposed by Matthews and Blakeslee (M-B) [56] and People and Bean (P-B) [57], respectively, are the most routinely used. The two approaches are presented herein for the sake of completeness.

The M-B model implies a mismatched film-substrate heterostructure with pre-existing threading dislocations (TDs) propagating from the substrate. Consequently, the critical thickness of the epitaxial film is evaluated by considering the movement of the TDs under the force of mismatch strain [56],

$$F_\varepsilon = \frac{2\mu(1+\nu)}{(1-\nu)} bh\varepsilon \cos\lambda \qquad \text{(Equation 1.3)}$$

where $b$ is the magnitude of the Burgers vector, $\varepsilon$ is the in-plane strain, and $\lambda$ is the angle between the slip direction and the direction in the film plane which is perpendicular to the line of intersection of the slip plane and the interface [56]. The self-energy of MDs produces a restoring force, $F_d$, that is acting opposite to $F_\varepsilon$,

$$F_d = \frac{\mu b^2}{4\pi(1-\nu)}\left((1-\nu\cos^2\beta)\left(\ln\frac{h}{b}+1\right)\right) \qquad \text{(Equation 1.4)}$$

where $\beta$ is the angle between the Burgers vector and the dislocation line.

The propagation of TDs requires that $F_\varepsilon > F_d$. The critical thickness ($h_c^{M-B}$) that corresponds to the formation of MDs is then derived considering the force balance $F_\varepsilon = F_d$, and

is given by the following expression,

$$h_c^{M-B} = \frac{b(1-\nu\cos^2\beta)}{8\pi f(1+\nu)\cos\lambda}\left(\ln\frac{h_c^{M-B}}{b}+1\right) \qquad \text{(Equation 1.5)}$$

The schematic illustration of the model of Matthews and Blakeslee is shown in Figure 1.9, where the pre-existing TDs are shown to thread from the substrate through the epitaxial film in the presence of the mismatch strain force, $F_\varepsilon$. Under the large $F_\varepsilon$, the TDs are forced to propagate through the layer by bowing. Simultaneously, this leaves misfit segments along the layer-substrate interface that aid to reduce the magnitude of $F_\varepsilon$ by destroying the lattice coherence between the film and the substrate.

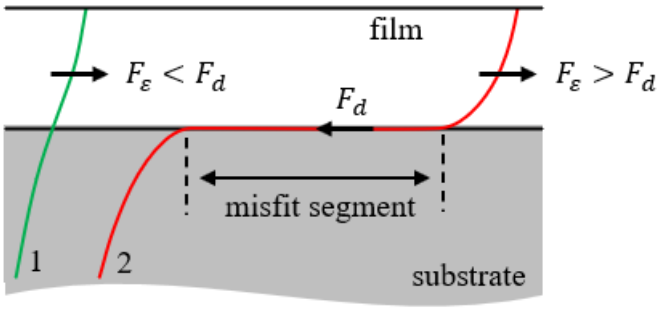


Figure 1.9. Schematic illustration of the forces acting on threading dislocations in a pseudomorphic (1) and relaxed (2) film on a lattice-mismatched substrate.

It is well recognized, however, that the measured critical thickness is often larger than the predictions made within the M-B model. An explanation of this can be attributed to a low number of TDs when the substrate is of high crystalline quality. On the contrary, the generation of strain relieving interfacial MDs within the model proposed by People and Bean [57] does not imply the existence of grown-in TDs but is determined solely by the energy balance. Herein, a misfit dislocation is generated when the magnitude of strain energy, $E_f$, in Equation 1.2 is larger than the strain energy of a dislocation,

$$E_D = \frac{\mu b^2}{8\pi\sqrt{2}a_0}\ln\frac{h}{b} \qquad \text{(Equation 1.6)}$$

The critical thickness, therefore, is derived considering the energy balance $E_f = E_d$, and is given by the following expression,

$$h_c^{P-B} = \frac{(1+\nu)}{(1-\nu)}\frac{1}{16\pi\sqrt{2}}\frac{b^2}{a_0}\frac{1}{f^2}\ln\frac{h_c^{P-B}}{b} \qquad \text{(Equation 1.7)}$$

Finally, understanding the strain relaxation processes in GeSn layers on Si and Ge substrates is important for material optimization in terms of predictable optical properties and crystalline quality.

Chapter 2: Experimental and theoretical methods

## 2.1 X-ray diffraction

The x-ray diffraction (XRD) experiment was carried out by using the Panalytical X'Pert Pro MRD diffractometer. The diffractometer is equipped with a fixed 1.6 kW x-ray tube with Cu anode that produces monochromatic Cu Kα1 radiation with the wavelength λ = 1.5406 Å. The monochromatization of the x-ray beam was achieved with the four-bounce Ge (220) monochromator and three bounce (022) channel-cut Ge analyzer. The scattered X-rays are recorded with a Pixel detector. The experimental arrangement of the key components of the diffractometer is illustrated in Figure 2.1.

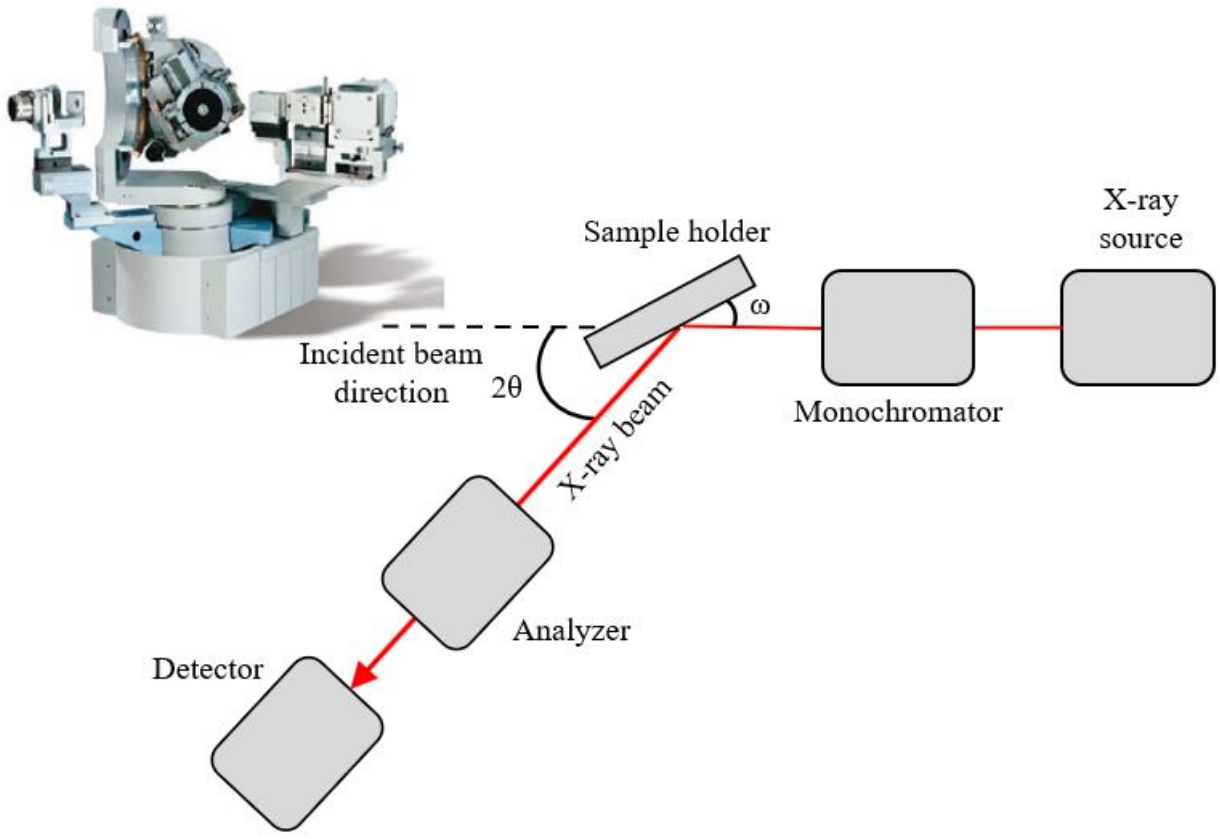


Figure 2.1. The key components of the diffractometer. ω is the incident beam angle with respect to the sample stage, and 2θ is the scattering angle.

2.1.1 X-ray diffraction ω/2θ scan

The ω/2θ scan (radial scan) is performed by simultaneously changing the incident beam angle, ω, and the scattering angle, 2θ, so that the change of the detector is rotated with a step size Δ(2θ) that corresponds to twice the step size over the ω axis (Figure 2.2a). A radial scan only varies the length of the scattering vector, **Q**, while not changing its direction (Figure 2.2b). Therefore, this type of x-ray diffraction measurement is sensitive to the variations of the lattice spacing and is typically executed to determine the strain state, chemical composition, crystalline phases, and epitaxial layer thickness [58]. The scattering geometry for ω/2θ scanning is shown in Figure 2.2.

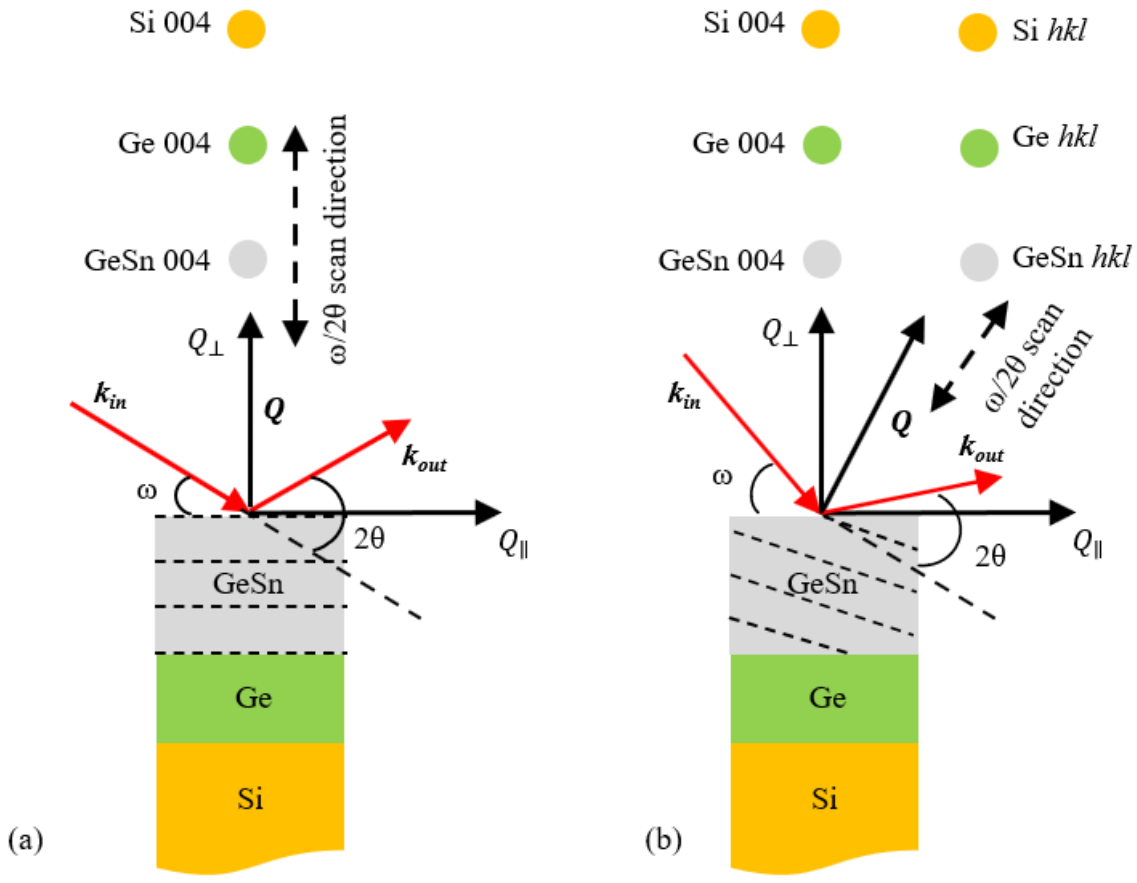


Figure 2.2. The scattering geometry for an ω/2θ scan for the case of symmetrical (a) and asymmetrical (b) reflection.

2.1.2 X-ray diffraction ω and ϕ scans

The ω scan (or rocking curve) is performed by rocking the sample around the ω axis, while the detector remains at a fixed position so that the magnitude of vector, **Q**, is fixed. In reciprocal space, the ω scan corresponds to the rotation of the scattering vector that is centered at the origin. Accordingly, the ω spectra are sensitive to lattice inclination, which often reflect the density of defects.

By performing a ϕ scan, the sample stage is rotated around the $\phi$ axis, while the ω and 2θ angles are kept fixed. The scattering geometry for ω and $\phi$ scanning is shown in Figure 2.3.

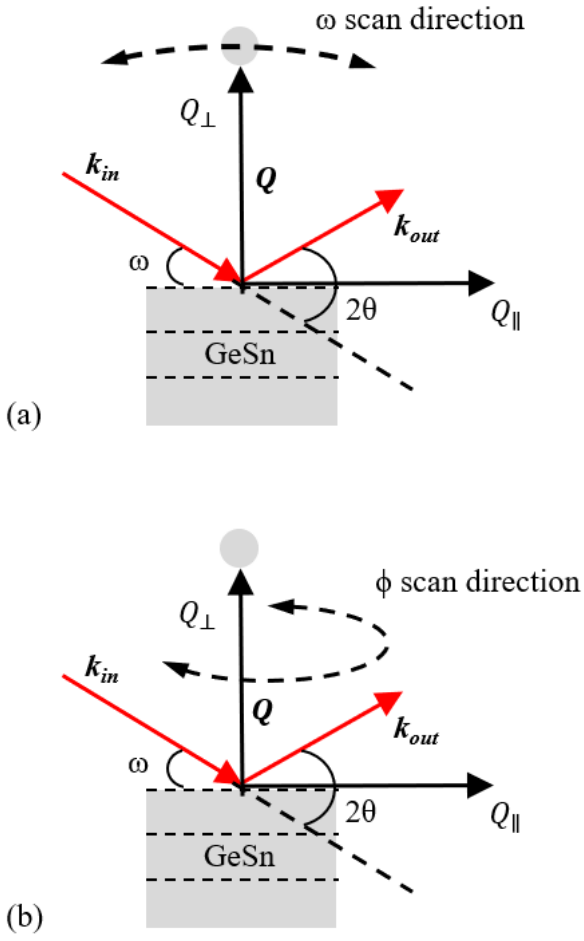


Figure 2.3. The scattering geometry for an ω (a) and ϕ scan (b).

2.1.3 Reciprocal space mapping

A reciprocal space map (RSM) is an important type of scan that allows an exploration of a two-dimensional region of the reciprocal space. Accordingly, the RSM of an asymmetrical reflection reveals the lateral and vertical lattice parameters for an epitaxial layer and substrate simultaneously. The RSM measurement can be carried out by a combination of ω (rocking curve) and ω/2θ scans. For example, an ω scan is performed by rocking the sample about the ω axis over a broad angular range, while the detector remains in a static position [58]. Afterward, the length of the scattering vector, ***Q***, is changed by altering the detector rotation angle 2θ (ω/2θ scan), and the ω scan is repeated. The schematic of the scattering geometry for an RSM is shown in Figure 2.4.

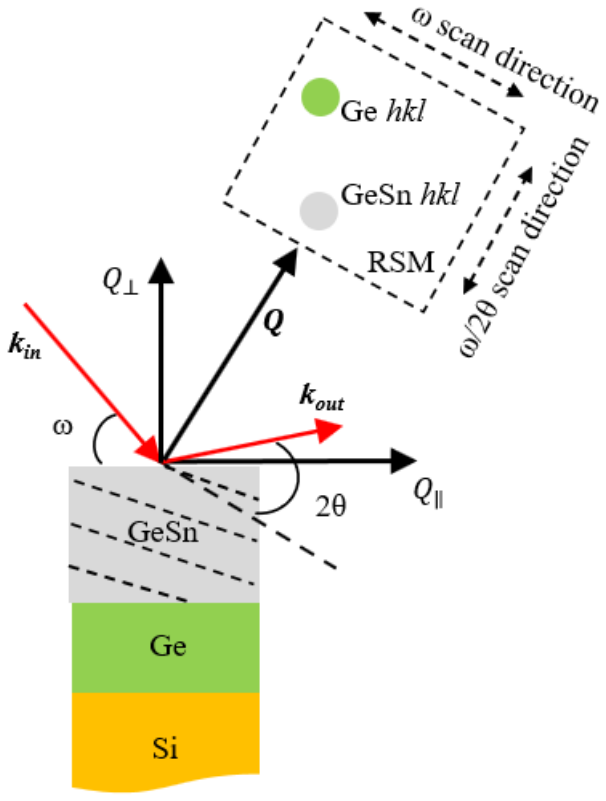


Figure 2.4. The scattering geometry for an RSM measurement across an asymmetrical *hkl* reflection.

2.1.3 X-ray diffuse scattering simulations

The RSM of an asymmetrical reflection contains a wealth of information about the defect configuration of an epitaxial layer, which allows the determination of the densities of defects in addition to the strain and elemental composition distribution. For a GeSn/Ge heterosystem, the GeSn layer is grown under compressive strain due to the 15% lattice mismatch between α-Sn and Ge. This compressive strain is relieved upon the critical thickness for strain relaxation, which is accompanied by an increasing density of misfit and threading dislocations. For example, the schematic illustration of an epitaxial layer of a diamond-like crystal with several MDs and TDs is shown in Figure 2.5. The displacement fields that arise around such defects significantly alter the distribution of scattered intensity, as compared with the scattering from an ideal crystal [59].

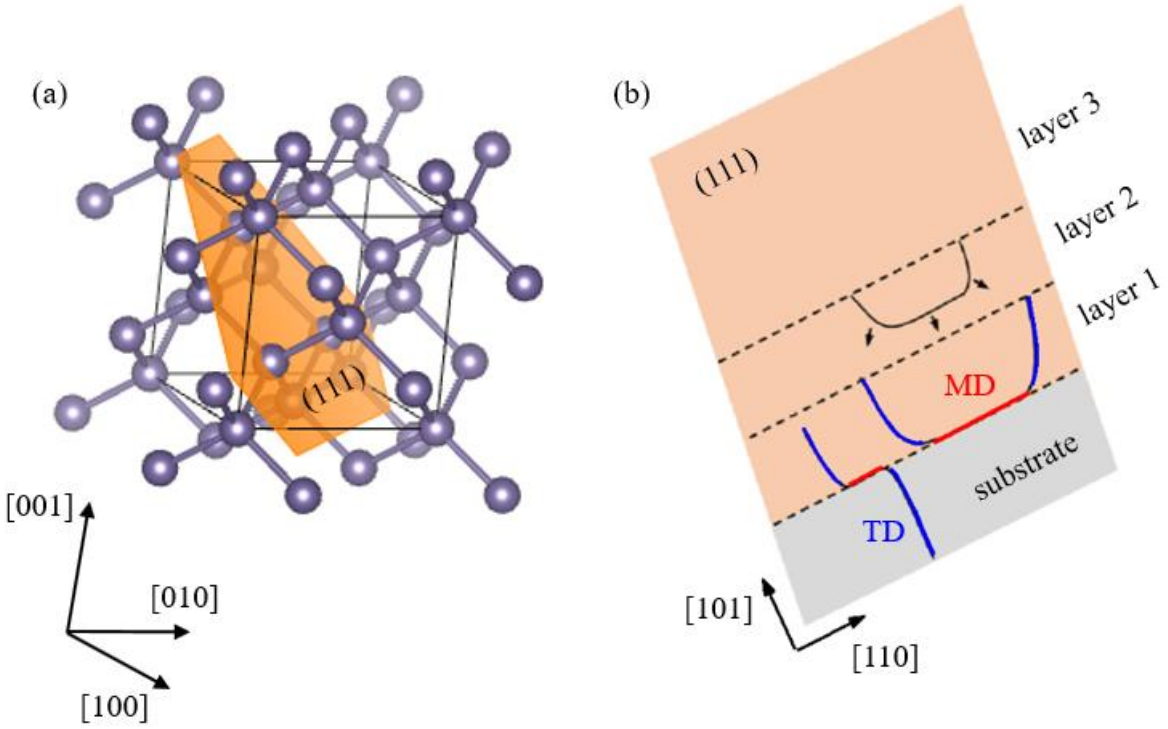


Figure 2.5. The unit cell of a diamond-like crystal (a) and the schematic illustration of the (111) plane for an epitaxial heterostructure containing dislocation loops (b).

The x-ray scattering intensity for a strongly dislocated crystal is usually calculated within the framework of kinematic theory for x-ray scattering. Typically it is assumed that MDs are stronger defects than the TDs, and the latter are omitted in the calculations [60]. The expression for the scattering intensity from an epitaxial layer with a grid of MDs located at the layer-substrate interface is given in the limit of a high density of MDs as follows [61],

$$I(q_x, q_z) = \pi \int_0^h \frac{dz}{\sqrt{det\hat{w}}} \exp\left(-\frac{1}{4} w_{ij}^{-1} (\boldsymbol{q} - \boldsymbol{q_0})_i (\boldsymbol{q} - \boldsymbol{q_0})_j\right) \quad \text{(Equation 2.1)}$$

where $h$ is the epitaxial layer thickness, $\boldsymbol{q} = \boldsymbol{Q} - \boldsymbol{Q_0}$ is the deviation of the scattering vector $\boldsymbol{Q}$ from the reciprocal lattice vector $\boldsymbol{Q_0}$, $\hat{w}$ is a symmetrical matrix composed of $w_{ij}$ elements with $i, j = x, z$. The $q_{0x}$ and $q_{0z}$ are the shifts of the diffraction peaks due to MDs, and are given by,

$$q_{0x} = \rho Q_x b_x \quad \text{(Equation 2.1)}$$

$$q_{0z} = -\frac{2\nu}{1-\nu} \rho Q_z b_x + q_z^c \quad \text{(Equation 2.3)}$$

where $\nu$ is the Poisson ratio, $\rho$ is the density of MDs, $b_x$ is the $x$ component of the Burgers vector, $q_z^c = \frac{1+\nu}{1-\nu} Q_{0z} f(z)$ is the shift of the diffraction peak related with alloy composition, and $f(z)$ is the lattice mismatch. The expressions for $w_{ij}$ determine the shape of diffuse scattering in the reciprocal space, and were defined by Kaganer et al. [61] as follows,

$$w_{xx}(z) = \frac{\rho}{2} \sum_{\sigma=x,z} \int_{-\infty}^{\infty} dx \left(Q_x^2 u_{x,x}^{(\sigma)2} + Q_z^2 u_{z,x}^{(\sigma)2}\right) \quad \text{(Equation 2.4)}$$

$$w_{xz}(z) = \frac{\rho}{2} Q_x Q_z \sum_{\sigma=x,z} \int_{-\infty}^{\infty} dx \left(u_{x,x}^{(\sigma)} u_{z,z}^{(\sigma)} + u_{x,z}^{(\sigma)} u_{z,x}^{(\sigma)}\right) \quad \text{(Equation 2.5)}$$

$$w_{zz}(z) = \frac{\rho}{2} \sum_{\sigma=x,z} \int_{-\infty}^{\infty} dx \left(Q_x^2 u_{x,z}^{(\sigma)2} + 2Q_z^2 u_{z,z}^{(\sigma)2} + Q_x^2 u_{x,z}^{(y)2}\right) \quad \text{(Equation 2.6)}$$

where $\rho$ is the density of MDs, $u_{i,j} = \partial u_i / \partial x_j$, and $u$ are displacements due to MDs lying

parallel to the surface and their expressions are given in Appendix B of Ref. [61].

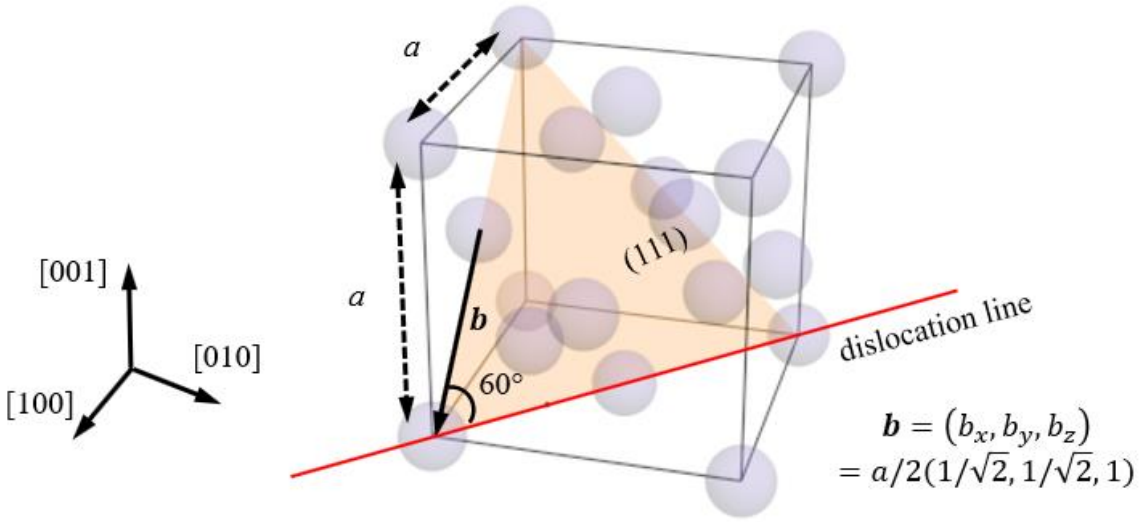


Figure 2.6. The geometry of a 60° misfit dislocation in a diamond-like crystal lattice.

The theory of X-ray diffuse scattering for a multilayer heterosystem was extended by Kopp et al. [62]. It implies that in a multilayer heterosystem the MDs are located at multiple interfaces. Accordingly, the contribution from MDs at each interface is considered in the expressions for $q$ and $w$ by the introduction of a Heaviside function, $H$, as follows,

$$q_{0x}(z) = Q_x b_x \sum_k \rho_k H(d_k - z) \qquad \text{(Equation 2.7)}$$

$$q_{0z}(z) = -\frac{2\nu}{1-\nu} Q_z b_x \sum_k \rho_k H(d_k - z) + q_{kz}^c \qquad \text{(Equation 2.8)}$$

$$w_{ij}(z) = \sum_k \left[ w_{ij}^k(z) H\left(d_j - z\right) + \widetilde{w}_{ij}^k(z) H(z - d_k) \right] \qquad \text{(Equation 2.9)}$$

where $k$ is the number of interfaces, $d_k$ is the thickness of the $k$th layer, $\rho_k$ is the density of MDs at the $k$th interface. The expressions for $w_{ij}^k(z)$ and $\widetilde{w}_{ij}^k(z)$ correspond to the layers above and below the $k$th interface.

## 2.2 Micro-Raman spectroscopy

The micro-Raman experiment was caried out at room temperature under backscattering configuration with the incident and scattered beams normal to the sample surface. The micro-Raman spectra were excited with a 632.8 nm He-Ne laser and an output power of 5 mW. The diameter of the laser spot was focused down to 1 μm using Olympus BX41 (AmScope, Irvine, CA) microscope equipped with an objective lens with 100x magnification. The Raman scattered light from the sample surface was dispersed by a dispersion grating with 1800 grooves/mm. Then the light was focused on a 0.75 m long spectrometer Horiba Jobin-Yvon LabRam HR800 (Horiba, United Kingdom) and detected with a thermoelectrically cooled Si charge-coupled device (CCD) camera. A notch filter was inserted to remove the elastically scattered laser light. The software Horiba LabSpec was used for data collection, where the signal was acquired five times before averaging. An exposition of 100 seconds was employed in each cycle. The spectra were acquired from seven different locations on the sample surface.

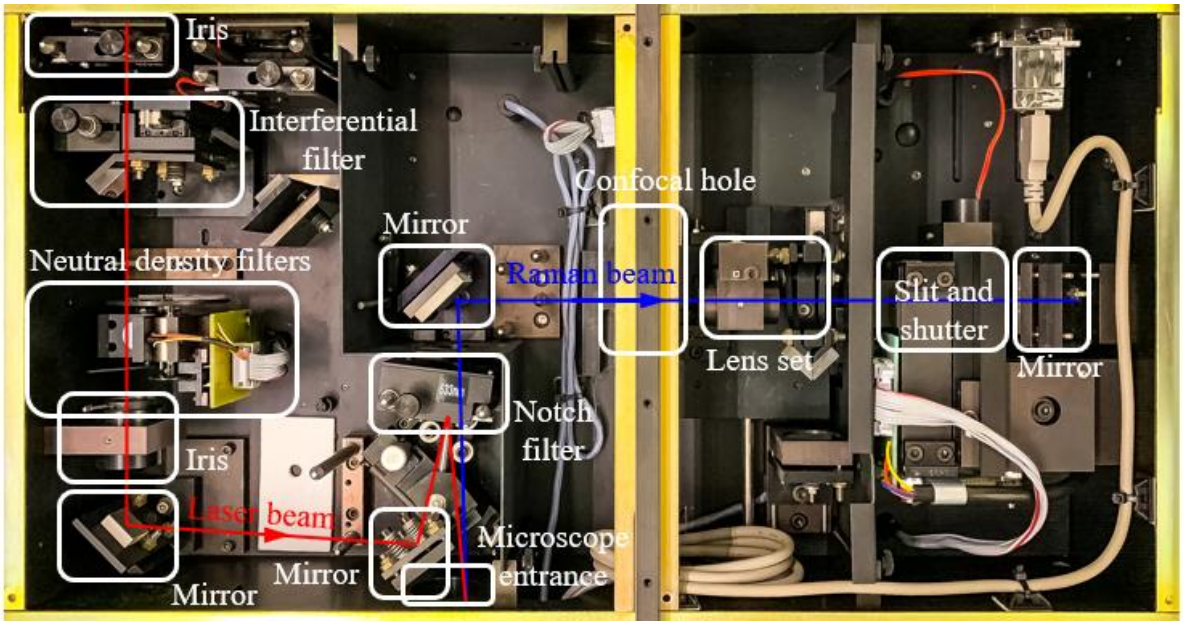


Figure 2.7. The key components of the micro-Raman setup.

## 2.3 Atomic force microscopy

Atomic force microscopy (AFM) is a characterization technique that is routinely used for topographical studies of the sample surface at the nanoscale. The AFM depends on the forces between the sample surface and the probing tip that is attached to a cantilever. The cantilever bends during the image acquisition due to an interacting force between the tip and surface, which is detected by a laser diode and a photodetector. A schematic illustration of the AFM assembly is shown in Figure 2.8.

In this work, the AFM measurements were carried out using the NanoScope IIIa Dimension 3000 scanning probe microscope (Bruker, former Digital Instruments, Billerica, MA) in tapping mode. The sample surface was probed with a silicon cantilever with a tip diameter of about 10 nm. For all samples, the AFM measurements were taken over the areas of 10 × 10 microns, with 512 measurements along each direction.

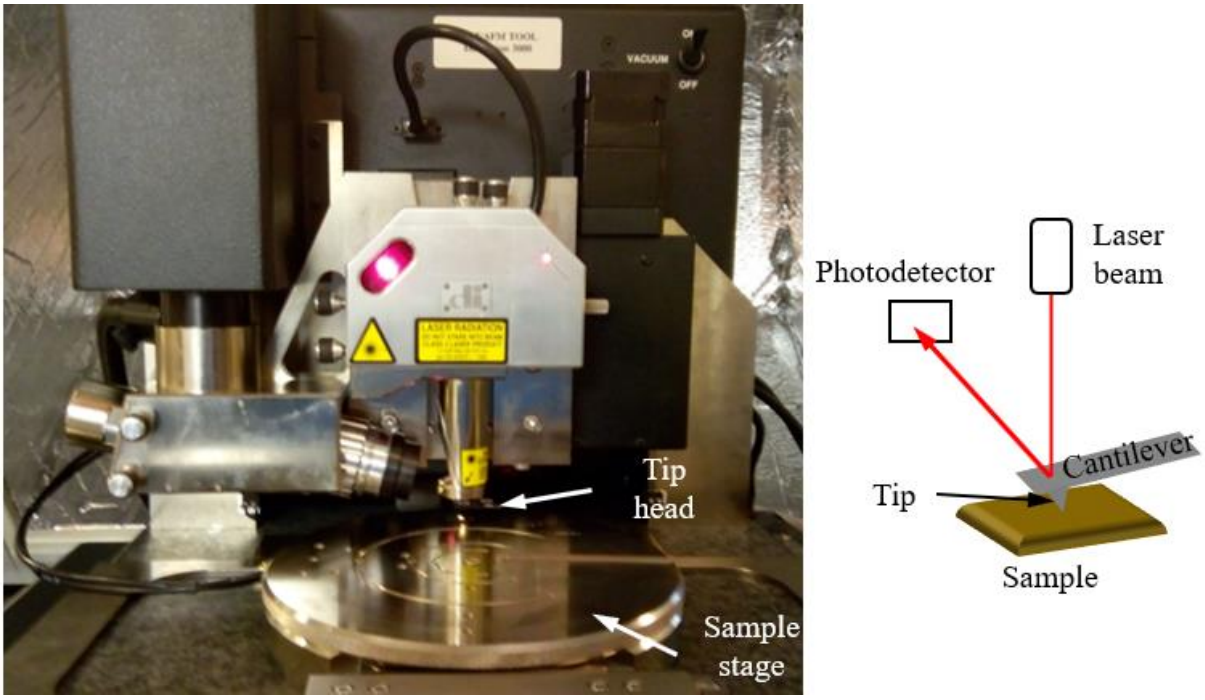


Figure 2.8. The photograph and schematic of the AFM assembly.

## 2.4 Scanning electron microscopy and energy dispersive x-ray analysis

Scanning electron microscopy (SEM) was performed using the FEI Nova Nanolab 200 SEM (FEI, Hillsboro, Oregon) for surface characterization. An XFlash 5010 detector (Bruker, Germany) was attached to the SEM for the energy-dispersive x-ray spectroscopy (EDX) analysis. In this work, EDX was used for the elemental mapping of the sample surface.

The basic principle of EDX is shown in Figure 2.9. The EDX is based on the analytical analysis of the x-ray emission that is related to electron transitions to the core levels. The core-level electrons are displaced from their shells after bombarding the sample surface with high energy electrons. Thereafter, the holes on the K shells are filled with the electrons from the higher levels. This electron transition is accompanied by the emission of characteristic x-rays (e.g., $K_\alpha$ and $K_\beta$).

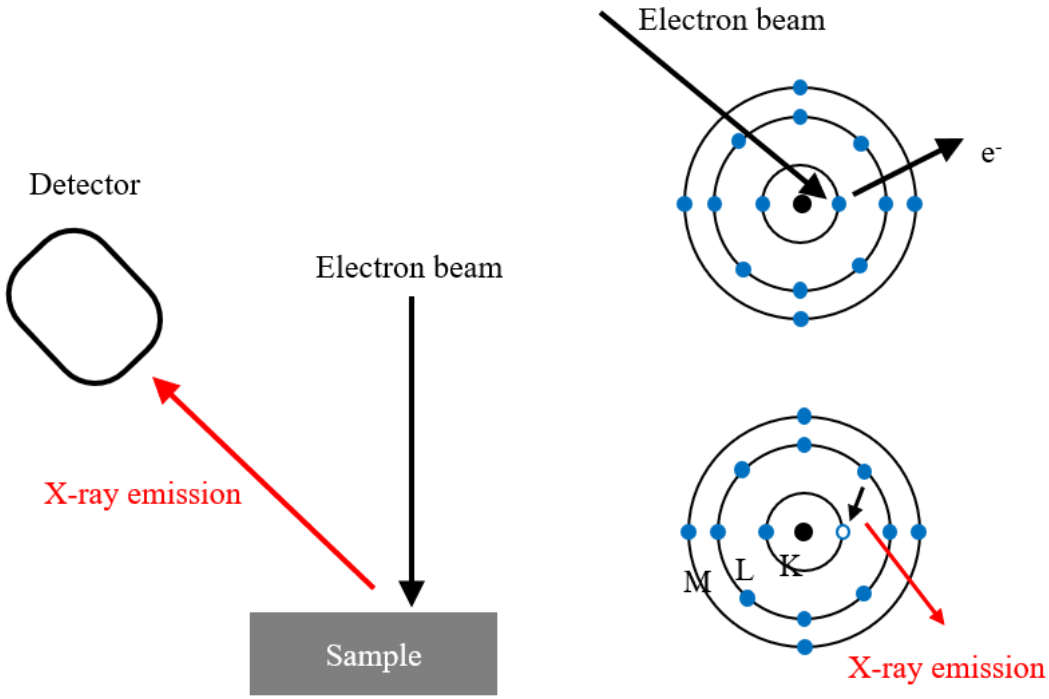


Figure 2.9. Energy-dispersive x-ray spectroscopy.

## 2.5 Photoluminescence spectroscopy

The photoluminescence (PL) measurements were conducted in a standardized off-axis PL arrangement enabled by a lock-in technique (chopped optically at 400 Hz). The PL spectra were recorded with a spectrometer connected to an InSb detector with a cut-off response of 3.0 μm. Two excitation laser beams with different penetration depth and laser emission at 532 nm continuous wave and a 1064 nm pulsed laser were used. For 532 nm laser excitation, the spot diameter and the average power were 64 μm and 500 mW, respectively. For 1064 nm laser excitation, the spot diameter and the average power were 51 μm and 300 mW, respectively.

# Chapter 3: The interplay of compressive strain and Sn composition in GeSn/Ge/Si(001) heterostructures

## 3.1 Introduction

Epitaxial growth of $Ge_{1-x}Sn_x$ layers on Ge is affected by the built-in compressive strain that is the result of large mismatch (15%) between the crystal lattice of Ge and α-Sn. Accordingly, the magnitude of strain in a $Ge_{1-x}Sn_x$ layer is a function of Sn composition and, thus, increases with the Sn content. The compressive strain relief during the growth favors an enhanced Sn incorporation into the $Ge_{1-x}Sn_x$ lattice, which was previously reported for the CVD growth of GeSn/Ge/Si(001) heterosystems [33], [63]. In particular, the spontaneous Sn enrichment is proven as a technique for growing Sn-rich $Ge_{1-x}Sn_x$ layers [33]. At the same time, the variation of the lattice spacing due to the changes of strain and Sn content has a significant impact on the material band structure and, as a result, on its optical and electronic properties. For example, the transition between direct and indirect bandgap GeSn semiconductors can be controlled by tailoring both the Sn composition and the strain state. Consequently, the quantification of the strain relief and Sn incorporation is important for the design and growth of GeSn for optoelectronic devices.

## 3.2 Samples description

All samples were grown on Si(001) substrates by CVD using an ASM Epsilon 2000 Plus reduced pressure system (ASM, Phoenix, AZ). Initially, the Si substrate was covered with a 700 nm thick Ge buffer layer, which was grown in two steps at 375 °C and 600 °C. Subsequently, the Ge buffer was annealed at 800 °C, which was followed by the GeSn growth at ~300 °C. Tin

and Ge species were delivered by $SnCl_4$ and $GeH_4$ precursors. Different thicknesses of the GeSn layers, such as 130 nm for sample S1, 750 nm for S2, and 1100 nm for S3, were achieved by varying the deposition time. The $SnCl_4/GeH_4$ molar flow fraction was kept constant for all samples to achieve GeSn layers with Sn composition of about 6.6 at. %. The GeSn layers of samples S2 and S3 were covered with a thin (10 nm) Ge layer. The $SnCl_4/GeH_4$ molar flow fraction, the growth temperature, and the deposition time for samples S4-S10 were varied to tune the Sn content from 4 to 15 at. % and the GeSn layer thickness. The schematic illustration of the sample structure is shown in Figure 3.1 for sample S1.


Figure 3.1. Schematic illustration of the sample structure.

## 3.3 Biaxial strain relationships

High-resolution XRD is routinely used for non-destructive analysis of strain state and elemental composition in epitaxial thin films. In particular, the conventional ω/2θ scans and RSMs are employed to measure the spacing, $d_{hkl}$, between the planes with Miller indices $h$, $k$, and $l$. For a tetragonal lattice, $d_{hkl}$ is related with the lateral, $a_{\parallel}$, and vertical, $a_{\perp}$, lattice

parameters of the unit cell by the following expression,

$$\frac{1}{d_{hkl}^2} = \frac{h^2 + k^2}{a_{\parallel}^2} + \frac{l^2}{a_{\perp}^2} \quad \text{(Equation 3.1)}$$

The magnitude of the lattice parameter $a_{\perp}$ is typically estimated from the peak positions on the measured XRD spectrum across the symmetrical 004 reflection ($h = k = 0$) by using Bragg's law,

$$2d_{hkl} \sin\theta_0 = n\lambda \quad \text{(Equation 3.2)}$$

where $\theta_0$ is the Bragg angle, $\lambda$ is the wavelength of the incident x-ray beam, and $n$ is the reflection order. The lateral lattice parameter is determined thereafter from the RSM of an asymmetrical reflection using the following relations between the scattering vector, $\boldsymbol{Q_{hkl}}$, and the interplanar spacing,

$$|\boldsymbol{Q_{hkl}}| = \sqrt{Q_{\parallel}^2 + Q_{\perp}^2} = \frac{2\pi}{d_{hkl}} \quad \text{(Equation 3.3)}$$

where

$$Q_{\parallel} = 2\pi \sqrt{\frac{h^2 + k^2}{a_{\parallel}^2}} \quad \text{(Equation 3.4)}$$

and

$$Q_{\perp} = 2\pi \frac{l}{a_{\perp}} \quad \text{(Equation 3.5)}$$

are components of the scattering vector, $\boldsymbol{Q_{hkl}}$, of a tetragonal lattice. The reciprocal space coordinates $Q_{\parallel}$ and $Q_{\perp}$ are related to the incident angle, $\omega$, and scattering angle, $2\theta$, by the following expressions [64],

$$Q_{\parallel} = \frac{2\pi}{\lambda}\{\cos\omega - \cos(2\theta - \omega)\} \quad \text{(Equation 3.6)}$$

$$Q_{\perp} = \frac{2\pi}{\lambda}\{\sin\omega + \sin(2\theta - \omega)\} \quad \text{(Equation 3.7)}$$

In the general form, the stress, $\sigma_{ij}$, and strain, $\varepsilon_{kl}$, components are related by the elastic stiffness constants, $C_{ijkl}$ [65],

$$\sigma_{ij} = C_{ijkl} \times \varepsilon_{kl} \quad \text{(Equation 3.8)}$$

For a cubic crystal, $C_{ijkl}$ is reduced into three independent elastic constants, $C_{11}$, $C_{12}$, $C_{44}$, as,

$$C_{ij} = \begin{pmatrix} C_{11} & C_{12} & C_{12} & 0 & 0 & 0 \\ C_{12} & C_{11} & C_{12} & 0 & 0 & 0 \\ C_{12} & C_{12} & C_{11} & 0 & 0 & 0 \\ 0 & 0 & 0 & C_{44} & 0 & 0 \\ 0 & 0 & 0 & 0 & C_{44} & 0 \\ 0 & 0 & 0 & 0 & 0 & C_{44} \end{pmatrix} \quad \text{(Equation 3.9)}$$

The relationship between the strain and stress components for a cubic lattice with its $z$ axis aligned along the $\langle 001 \rangle$ direction can be further simplified assuming that the epitaxial layer is under biaxial stress. In this case, the lattice is deformed in the $(x, y)$ plane to adapt with the lattice parameter of the underlying substrate. Such biaxial deformation is described by constant forces [65]

$$\sigma_{xx} = \sigma_{yy} = (C_{11} + C_{12})\varepsilon_{\parallel} + C_{12}\varepsilon_{\perp} \quad \text{(Equation 3.10)}$$

and vanishing forces

$$\sigma_{zz} = 2C_{12}\varepsilon_{\parallel} + C_{11}\varepsilon_{\perp} = 0 \quad \text{(Equation 3.11)}$$

Accordingly, the lateral and vertical strains $\varepsilon_{\parallel}$ and $\varepsilon_{\perp}$ are related by the elastic constants $C_{11}$ and $C_{12}$ as follows,

$$\varepsilon_{\perp} = -2\frac{C_{12}}{C_{11}}\varepsilon_{\parallel} \quad \text{(Equation 3.12)}$$

$$\varepsilon_{\perp} = \frac{a_{\perp} - a_0}{a_0} \quad \text{(Equation 3.13)}$$

$$\varepsilon_{\parallel} = \frac{a_{\parallel} - a_0}{a_0} \quad \text{(Equation 3.14)}$$

where $a_0$ is the lattice parameter for the unstrained lattice.

For a $Ge_{1-x}Sn_x$ alloy, the lattice parameter, $a_0$, and the elastic constants vary with Sn composition, $x$, almost linearly. Therefore, these are approximated using Vegard's law,

$$a_0 = x a_{Sn} + (1 - x) a_{Ge} \quad \text{(Equation 3.15)}$$

$$C_{11} = x C_{Sn}^{11} + (1 - x) C_{Ge}^{11} \quad \text{(Equation 3.16)}$$

$$C_{12} = x C_{Sn}^{12} + (1 - x) C_{Ge}^{12} \quad \text{(Equation 3.17)}$$

where $a_{Sn} = 0.6489$ nm and $a_{Ge} = 0.5658$ nm are the lattice parameters of bulk α-Sn and Ge, respectively, $C_{Sn}^{11} = 69$ GPa, $C_{Sn}^{12} = 29.3$ GPa, $C_{Ge}^{11} = 126$ GPa, and $C_{Ge}^{12} = 44$ GPa are the relevant elastic constants [66].

## 3.4 Crystallographic tilt

According to the expressions for $Q_{\parallel}$ and $Q_{\perp}$, one can determine the values of both $a_{\parallel}$ and $a_{\perp}$ from a single RSM of an asymmetrical reflection. However, in the presence of lattice inclination, such as a miscut (or crystallographic tilt), this may lead to an erroneous determination of the lattice parameters. The crystallographic tilt in epitaxial layers is typically associated with an unequal density of dislocations with opposite Burgers vector. Particularly, the miscut of the underlying substrate either increases or decreases the angle between the Burgers vector of the dislocation and the surface normal, which results in different shear stress. This favors the preferential nucleation of dislocations with the particular Burgers vector [67]. In reciprocal space, the miscut is associated with an inclination of the scattering vector by an angle, $\alpha$, which also can be seen as a shift of the diffraction peak along the $Q_{\parallel}$ and $Q_{\perp}$ axis as shown in

Figure 3.2.

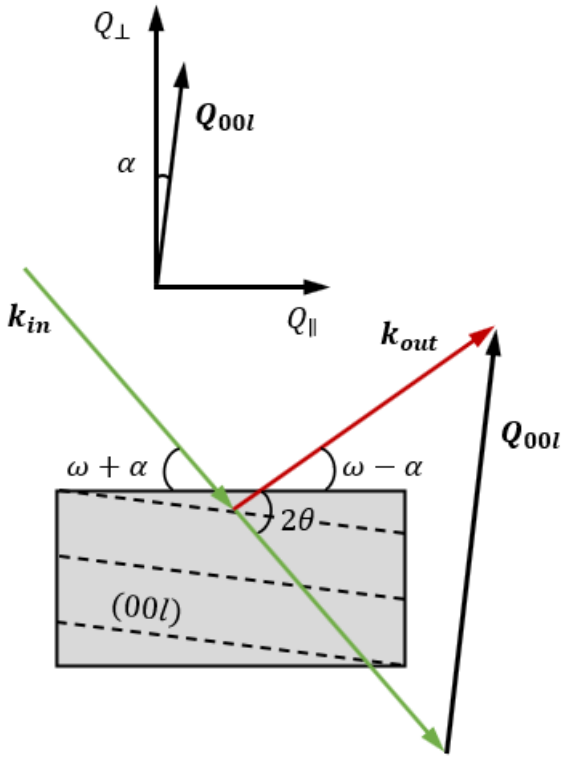


Figure 3.2. Schematic illustration of the effect of lattice miscut on the orientation of the scattering vector. $\boldsymbol{k_{in}}$ and $\boldsymbol{k_{out}}$ are the wavevectors of the incident and scattered X-ray beam.

To study the miscut of the Si(001) planes, as well as the crystallographic tilt between the Si(001) and Ge(001) planes and between the Ge(001) and GeSn(001) planes, a series of ω scans were measured for sample S3 across the 004 reflection of Si, Ge, and GeSn at different azimuthal angles, $\phi$ (Figure 3.3). Substantial shifts of the 004 Si peaks from the Bragg's position at $\omega_0$ = 34.5646 deg can be seen on the ω spectra in Figure 3.3a, measured for 0, 90, 180, and 270 deg azimuthal angles, which signifies a considerable miscut angle. The shifts of the 004 peaks on the ω spectra measured for the Ge (Figure 3.3b) and GeSn (Figure 3.3c) layers are close to those of Si substrate, which indicates that the (001) planes of Ge and GeSn are parallel to the (001) planes of Si.

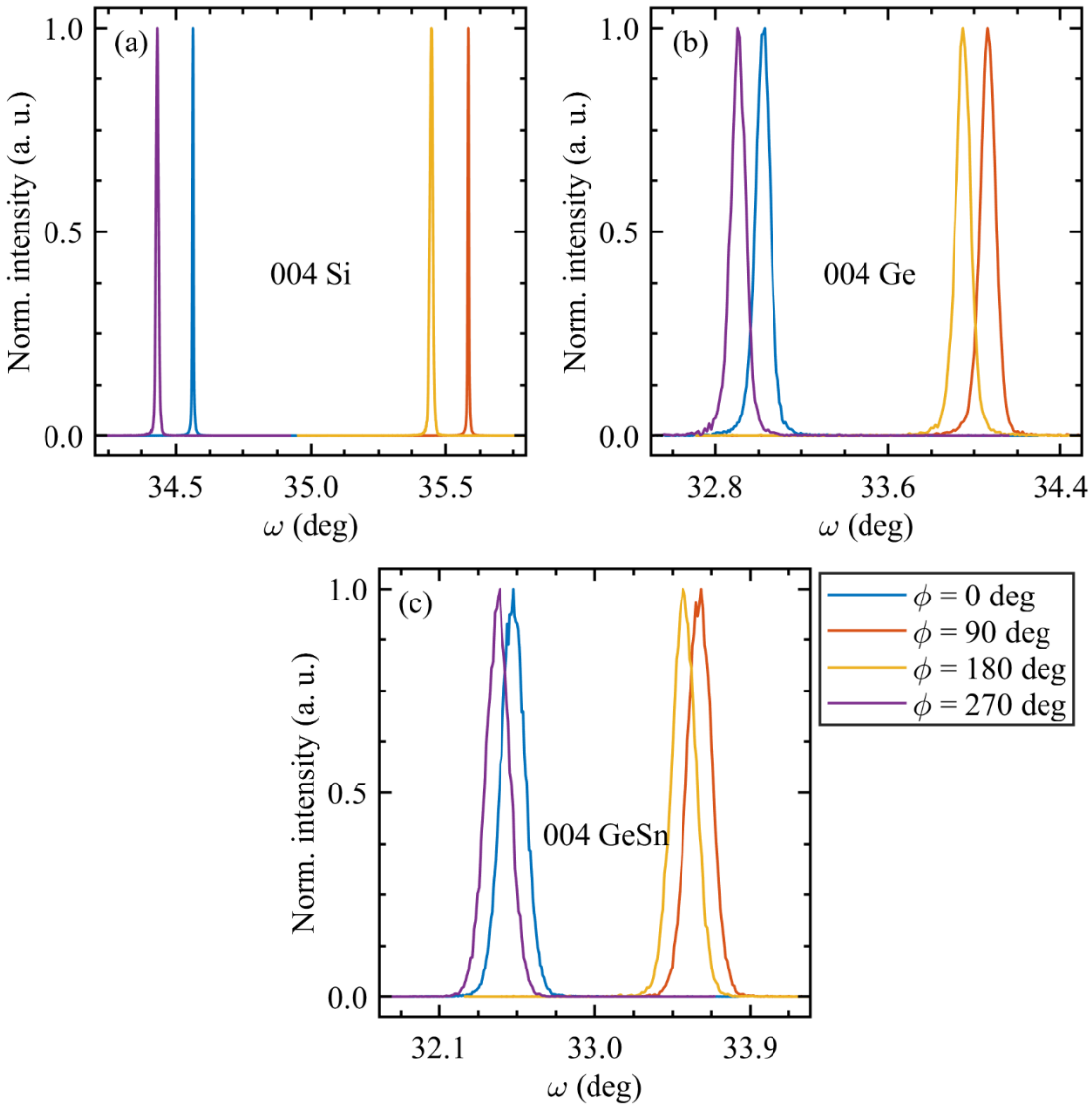


Figure 3.3. X-ray diffraction ω scans measured for the 004 reflection of Si (a), Ge (b), and GeSn (c) at different azimuthal angles $\phi$ for sample S3.

Quantitatively, the miscut and crystallographic tilt angles were studied by fitting the 004 ω spectra with Pseudo-Voigt functions as follows [68],

$$PV(\omega) = (1 - f)G(\omega) + fL(\omega) \qquad \text{(Equation 3.18)}$$

where $f$ is the profile shape factor and $G(\omega)$ and $L(\omega)$ are the Gaussian and Lorentzian functions,

$$G(\omega) = A \exp\left(-\frac{(\omega - \omega_c)^2}{W^2} 4\ln(2)\right) \quad \text{(Equation 3.19)}$$

$$L(\omega) = \frac{A}{[\pi \ln(2)]^{1/2}} \left(\frac{1}{4\frac{(\omega - \omega_c)^2}{W^2} + 1}\right) \quad \text{(Equation 3.20)}$$

Here, $W$ is the full width at half maximum, $\omega_c$ is the mean of the distribution, and $A$ is the peak area. For sample S3, the measured and fitted ω spectra at $\phi$ = 0 deg are shown in Figure 3.4.

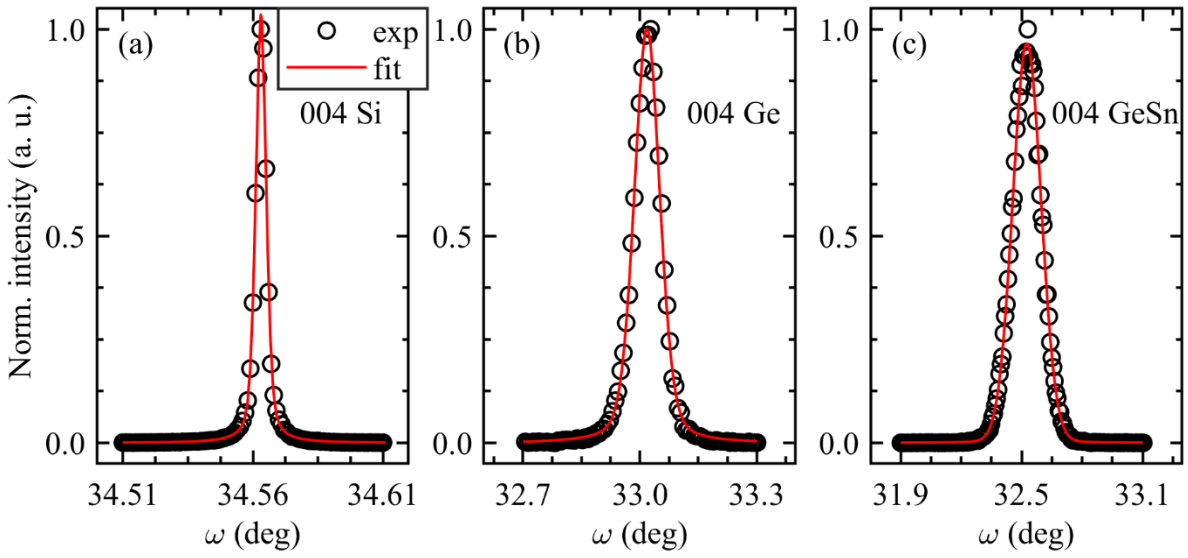


Figure 3.4. Measured (symbols) and fitted (line) 004 ω scans for the Si (a), Ge (b), and GeSn (c) layers of sample S3.

Figure 3.5 shows the variation of $\omega_c$ as a function of azimuthal angle, $\phi$. The values of $\omega_c$ decrease from Si to Ge to GeSn according to Bragg's law in Equation 3.2 due to the relative increase of the vertical lattice parameter, $a_\perp$. Moreover, the positions of the 004 peaks are shifted toward the higher angles, $\omega_c$, while rotating the sample up to about $\phi$ = 130 deg. The lowest angles, $\omega_c$, are revealed after the 180 deg rotation, which corresponds to the opposite direction of the sample. Therefore, the miscut angles can be estimated as $(\omega_{130} - \omega_{310})/2$ [67].

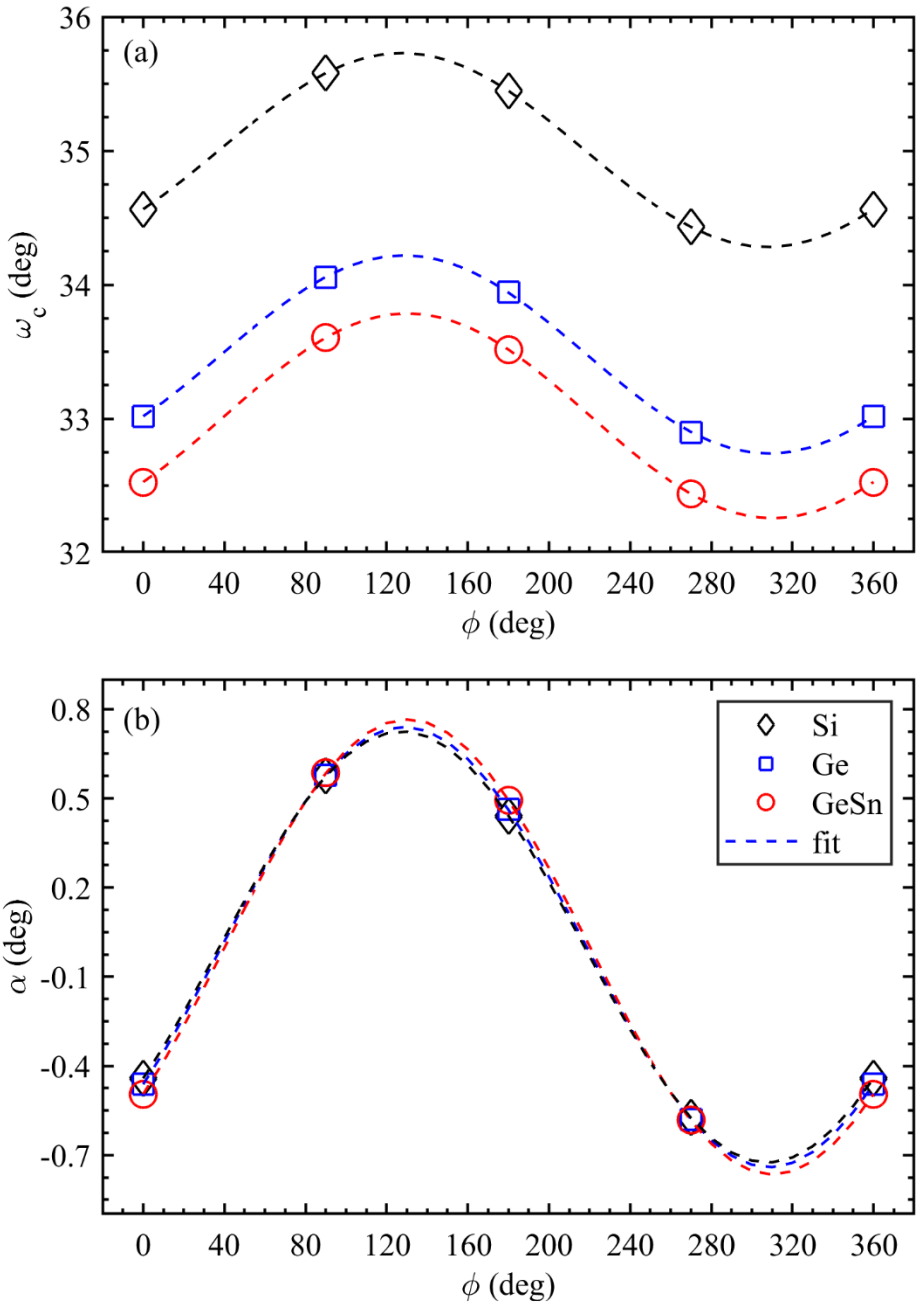


Figure 3.5. The peak positions (a) and miscut/tilts (b) of Si (004), Ge(004), GeSn (004) measured as a function of sample rotations.

More precisely, the miscut/tilt angle, $\alpha_0$, of the (001) lattice planes is determined by fitting the experimental data in Figure 3.5a over the range of azimuthal angles from 0 to 360 deg, with the following expression [69],

$$\tan(\alpha + c_1) = \cos(\phi + c_2) \times \tan(\alpha_0) \qquad \text{(Equation 3.21)}$$

where $\alpha$ is the offset angle, and $c_1$ and $c_2$ are fitting parameters related to the mounting of the sample on the sample stage.

Fittings of the experimental data in Figure 3.5a revealed that the miscut angle, $\alpha_0$, for the Si (001) planes is as large as 0.73 deg, and the miscut of the Ge and GeSn (001) planes is 0.74 and 0.77 deg, respectively. Accordingly, the miscut of Ge and GeSn is mostly representative of the Si miscut. At the same time, the crystallographic tilt between the Si and Ge as well as between Ge and GeSn is negligibly small, 0.01 and 0.03 deg, respectively. This can be seen in Figure 3.5b, which compares the orientational tilt $\alpha$ for the (001) planes of Si, Ge, and GeSn. In practice, this allows studying the strain and composition in the GeSn layer without considering the corrections for crystallographic tilt.

## 3.5 Characterization of the role of compressive strain on the compositional gradient in GeSn/Ge/Si(001) heterostructures

For samples S1, S2, and S3, the XRD ω/2θ spectra from the symmetrical 004 planes are shown in Figure 3.6. For all samples, the XRD spectra were normalized with respect to Si (004) substrate with the Bragg's angle positioned at $\theta_0$ = 34.5646 deg. Since the interplanar spacing $d_{004}$ increases down the periodic tables, the respective peaks associated with the Si, Ge, and GeSn can be seen in the order of decreasing scattering angle following Bragg's law in Equation 3.2. The vertical dashed line in Figure 3.6 marks the Bragg position of bulk Ge at $\theta_0$ = 32.9956 deg. The peak associated with the Ge buffer is seen shifted towards higher angles from the angular position of bulk Ge, which indicates that the unit cell of the Ge buffer layer is compressed in the vertical direction. An additional diffraction maximum is observed as a

shoulder near the Ge buffer peak for samples S3 and S2, which was associated with the 10 nm thin Ge cap layer. For sample S1, the Ge peak asymmetry at the side of higher scattering angles was attributed to SiGe alloying near the Ge/Si interface that forms during the deposition of the Ge buffer. A similar asymmetry was also reported elsewhere [70].

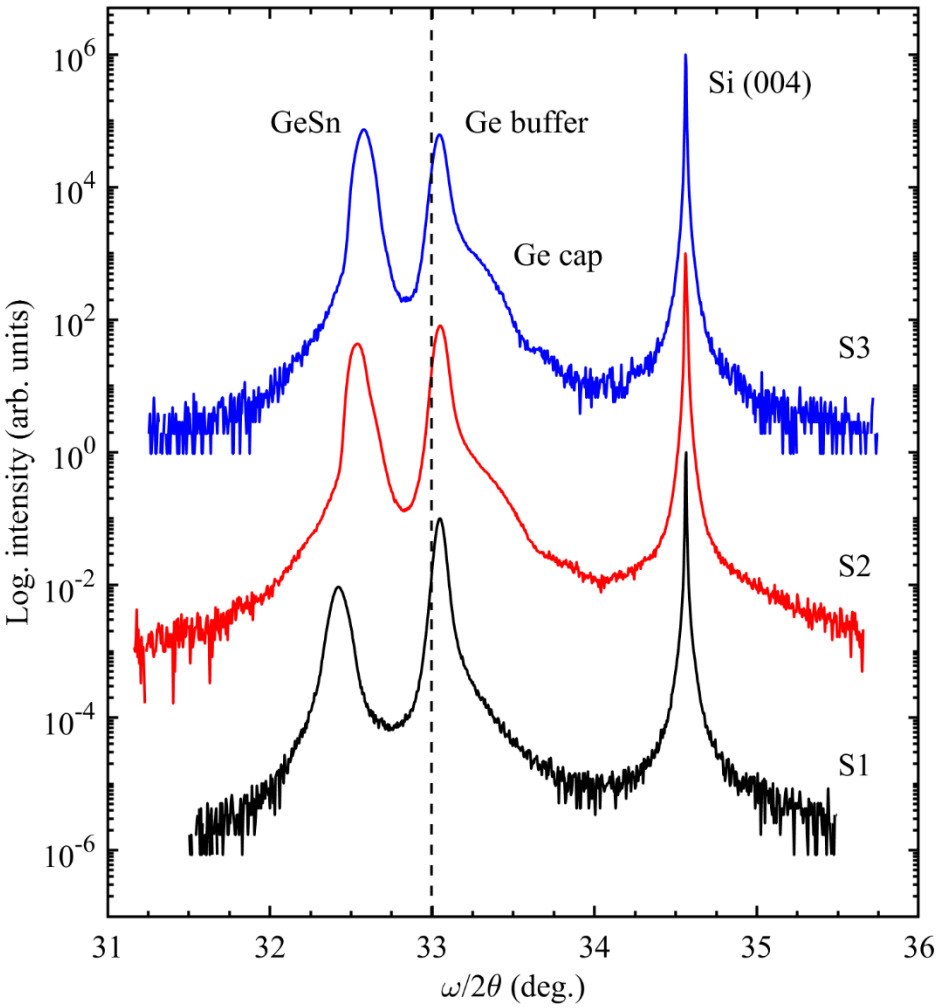


Figure 3.6. Measured x-ray diffraction ω/2θ scans of the symmetrical 004 reflection for samples S1 (black line), S2 (red line), and S3 (blue line). The vertical dashed line shows the peak position for bulk Ge [71].

The lattice parameters $a_\perp$ for the Ge buffer, GeSn, and Ge cap were calculated by fitting the respective peaks in Figure 3.6 with Gaussian functions to determine the Bragg's angle $\theta_0$.

The value of $a_\perp$ was then calculated by substituting the measured $\theta_0$ and Equation 3.1 in Equation 3.2,

$$a_\perp = \frac{2\lambda}{\sin\theta_0} \qquad \text{(Equation 3.22)}$$

The measured lattice parameters, $a_\perp$, are compared in Figure 3.7 for all samples. As it can be seen, the lattice spacing, $a_\perp$, in the Ge buffer does not exhibit significant changes among the samples, which indicates that the growth of the GeSn layer does not significantly affect the strain state of the Ge buffer. The strain in the Ge buffer was estimated by using the measured $a_\perp$ in Equation 3.13 and Equation 3.12. For all samples, the Ge buffer layer was found tensile strained in the plane of the interface, with the magnitude of lateral strain, $\varepsilon_\parallel = 0.2 \pm 0.01$ %. This is the typical value of residual strain reported for the growth of Ge on Si [72], where it is attributed to the mismatch of thermal expansion coefficients between the two materials.

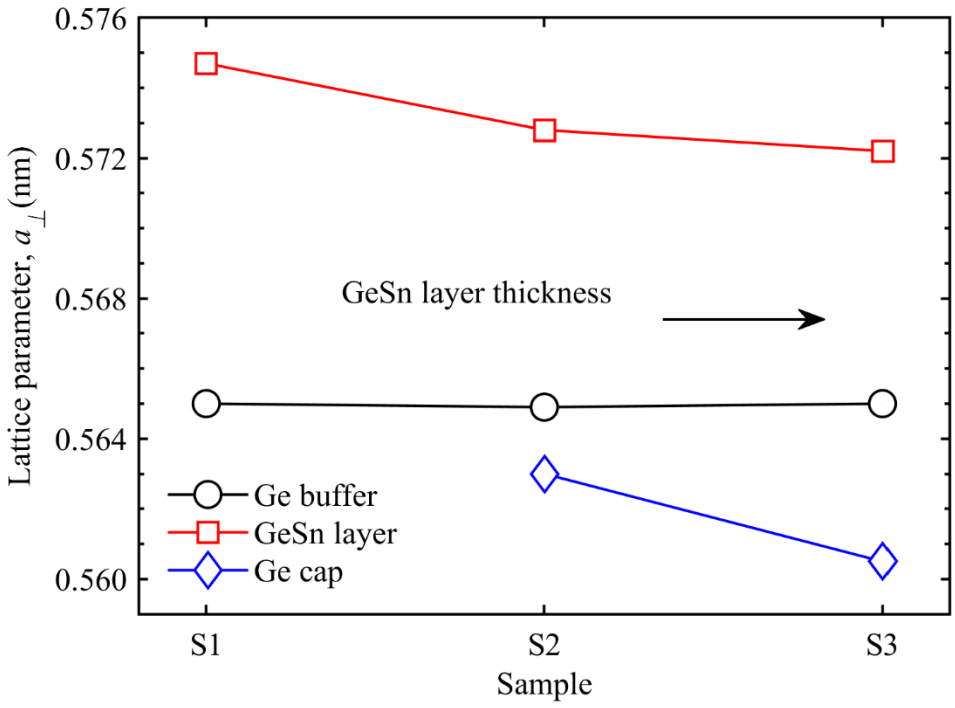


Figure 3.7. Measured vertical lattice parameters in the Ge cap, GeSn, and Ge buffer layers of samples S1, S2, and S3.

In Figure 3.7, the magnitude of $a_\perp$ in the GeSn and Ge cap layers decreases from sample S1 and S2 to S3 following the increasing GeSn layer thickness. It should be noted that the decrease of $a_\perp$ in the GeSn layer can be attributed both to stain relaxation as well as to the decrease of Sn content, since both reduce the magnitude of $a_\perp$. However, the Sn composition in the GeSn layer cannot be resolved from an ω/2θ scan of the 004 reflection since this is not sensitive to $a_\parallel$. At the same time, according to the biaxial strain relation in Equation 3.12, the decrease of $a_\perp$ in the Ge cap can be correlated to the increase of the lattice parameter $a_\parallel^{Ge\ cap}$.

The magnitude of $\varepsilon_\parallel$ in the Ge cap was estimated to be 0.7 ± 0.01 % and 1.3 ± 0.03 % for sample S2 and S3, respectively. Since the 10 nm thin Ge cap layer must be fully strained to the underneath GeSn layer ($a_\parallel^{GeSn} = a_\parallel^{Ge\ cap}$), the increase of $\varepsilon_\parallel$ was considered as a direct indication of the increasing $a_\parallel^{GeSn}$ and, therefore, of the increasing degree of strain relaxation in the GeSn layer underneath the Ge cap. The GeSn layer of sample S3 experiences even a larger degree of strain relaxation that is related to its larger thickness as compared with the GeSn layers of samples S1 and S2.

As mentioned above, the strain state in the GeSn layers cannot be resolved from a single 004 ω/2θ scan using the same approach as for the Ge buffer and the Ge cap. This is related to the different Sn composition in the as-grown and designed GeSn layers and, thus, to the unknown bulk lattice parameter, $a_0$, in Equation 3.15. For example, Figure 3.8 shows the relationship between Bragg's angle, $\theta_0$, strain, and Sn composition on the example of several GeSn layers with Sn content of 10, 8, and 6 at. %. As can be seen, the magnitude of $\theta_0$ decreases with both the increase of Sn composition and $\varepsilon_\perp$ strain.

The lateral lattice parameter, $a_\parallel$, is commonly determined from the RSM of an asymmetrical reflection, which according to Equation 3.1 is sensitive to both $a_\parallel$ and $a_\perp$.

Accordingly, the RSMs were measured in the vicinity of Ge $\bar{2}\bar{2}4$ reflection to capture the peaks from the Ge buffer and GeSn layers (Figure 3.9), which also reveals the epitaxial relationship between the crystal lattices of the two layers. The Ge buffer is seen on the RSMs as a high-intensity peak on the top left corner near the location of bulk Ge, which is shown with a star symbol. The Ge buffer is under residual strain, which is concluded from the respective peak position on the RSMs. This agrees with the Ge peak shift on the 004 ω/2θ scans in Figure 3.6. The Ge cap layers can be observed on the RSMs of sample S2 (Figure 3.9b) and S3 (Figure 3.9c) as weak diffraction spots. Because of the different strain state, these are located at lower $|Q_{\parallel}|$ relative to the Ge buffer. The peak from the GeSn layer is positioned below the Ge buffer in agreement with the larger $a_{\perp}$ in Figure 3.7.

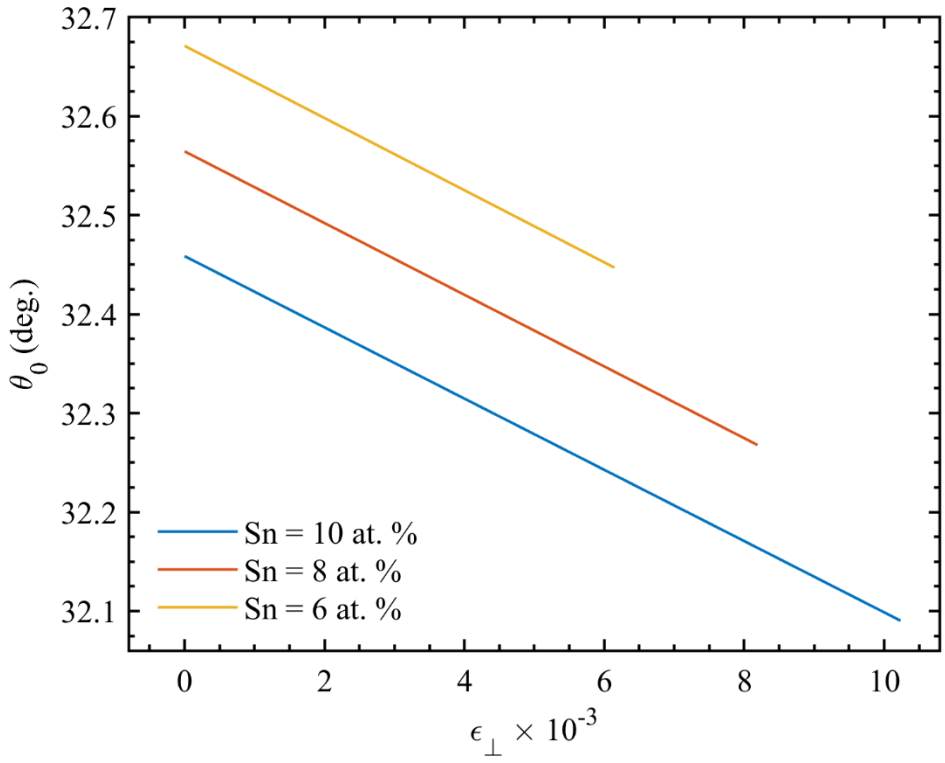


Figure 3.8. The relationship between the vertical strain and Bragg's angle calculated for the 004 reflection of several $Ge_{1-x}Sn_x$ alloys on Ge substrate.

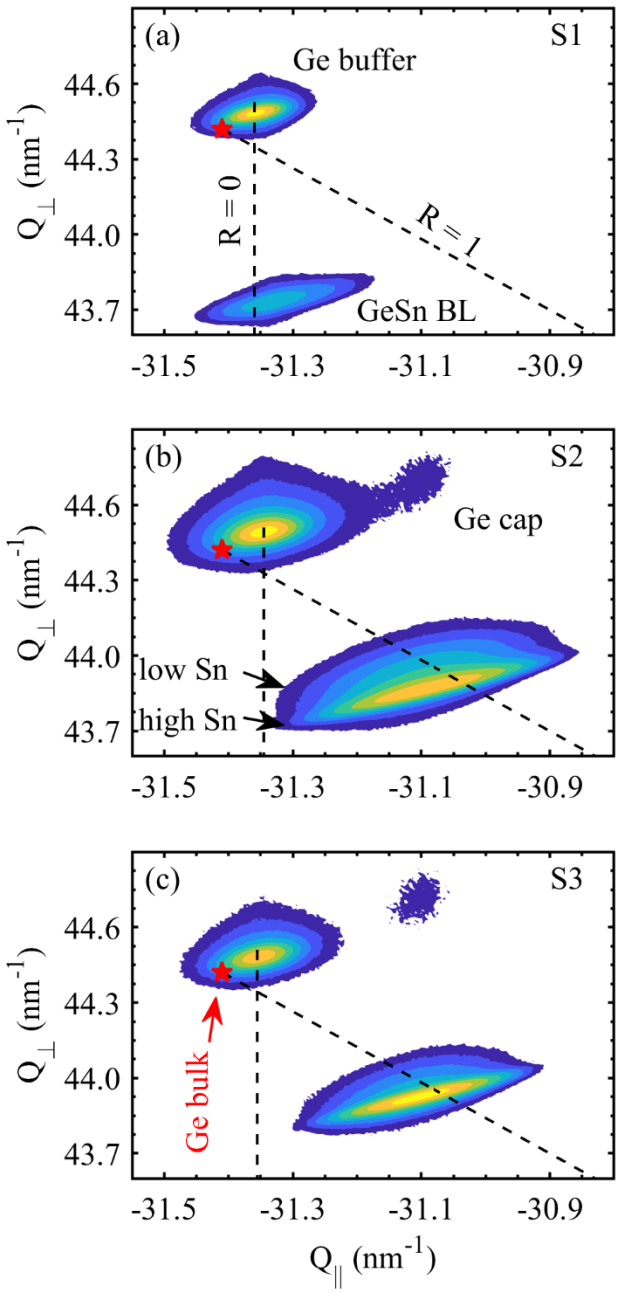


Figure 3.9. Measured XRD RSMs showing the $\bar{2}\bar{2}4$ reflection of Ge and GeSn layers for samples S1 (a), S2 (b), and S3 (c). The dashed line marked as R = 0 and R = 1 show the location of fully strained and fully relaxed $Ge_{1-x}Sn_x$, respectively [71].

The reciprocal space coordinates for the fully relaxed and pseudomorphic $Ge_{1-x}Sn_x$ alloys are shown as vertical (R = 0) and inclined (R = 1) dashed lines, respectively, for a large range of Sn compositions. As can be seen in Figure 3.9a, the GeSn peak of sample S1 is near the vertical

dashed line (R = 0), which indicates that the GeSn layer is almost fully strained to the Ge buffer. The GeSn peak shifts in the direction of the (R = 1) line for sample S2 and sample S3 due to the strain relief in the GeSn layers.

The layer thickness is also reflected in the peak intensity on the RSM so that the peak intensity ratio between the GeSn and Ge peak increases from sample S1 and S2 to S3. The GeSn peak for sample S3 appears on the RSM as the most intensive peak (Figure 3.9c), which is related with the larger relative thicknesseses of GeSn and Ge layers. It is noticeable that the diffraction spot from the Ge cap is located above the GeSn peak at the same $Q_{\parallel}$ value, which confirmed that the thin Ge cap is fully strained to the GeSn layer.

The migration of the GeSn peak to the R = 1 line is accompanied by the broadening of the diffraction spot along the $Q_{\parallel}$ and $Q_{\perp}$ axes, which can be seen by comparing the RSM of sample S1 with that of samples S2 and S3. Commonly, this is attributed to the increasing density of dislocations in a relaxed epitaxial layer [73]. At the same time, the peak width decreases with increasing layer thickness. This explains the much narrower GeSn peak for sample S3 in comparison with that of sample S2. It can be noticed that the diffuse scattering around the Ge buffer peak closely follows that of the GeSn layer. However, the fixed peak position of the Ge buffer for different samples indicated the absence of additional misfit dislocations in the Ge buffer. Accordingly, the diffuse scattering around the Ge peak was attributed to the misfit dislocations at the GeSn/Ge interface. For instance, this effect was considered in Ref. [62] for an XRD study of plastic strain relaxation in SiGe layers.

An additional broadening was observed along the scattering vector $\boldsymbol{Q}$, which was related to a spontaneous change of composition during the growth [63]. On the RSMs in Figure 3.9, these regions were associated with the high and low Sn content GeSn peaks. More explicitly, the

regions with enhanced Sn composition in the GeSn layer of samples S2 and S3 can be seen in Figure 3.10, which shows the extracted $Q$ scans over the $\bar{2}\bar{2}4$ GeSn peak on the RSMs.

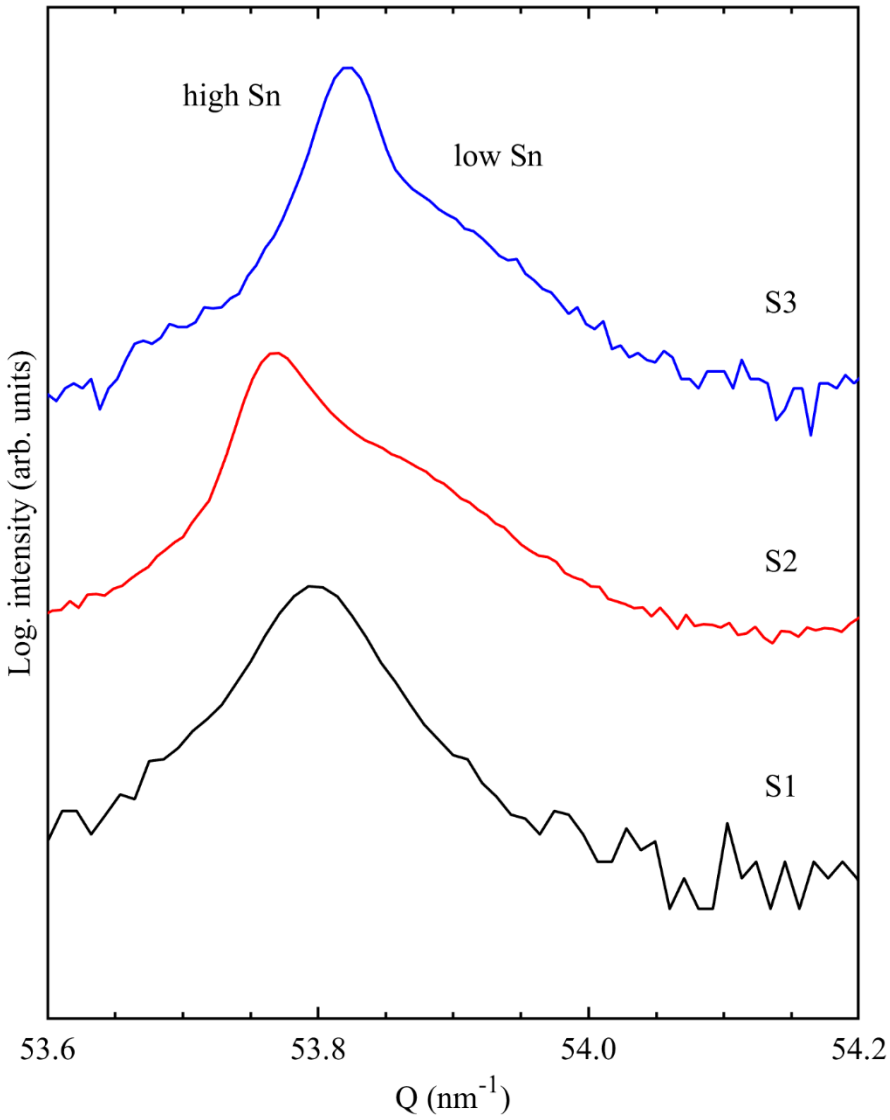


Figure 3.10. Extracted spectra over the GeSn peak region on the $\bar{2}\bar{2}4$ RSMs of samples S1 (black), S2 (red), and S3 (blue).

The lattice parameter, $a_{\parallel}$, in the GeSn layer was calculated according to Equation 3.4 by measuring the $Q_{\parallel}$ position of the GeSn peaks on the RSM. Afterward, the substitution of $a_{\parallel}$ in Equation 3.12 allowed determination of the unstrained lattice parameter, $a_0$, for the $Ge_{1-x}Sn_x$

alloy of unknown Sn composition, $x$, as follows,

$$a_0 = \frac{a_\perp + 2\frac{C_{12}}{C_{11}}a_\parallel}{1 + 2\frac{C_{12}}{C_{11}}} \qquad \text{(Equation 3.23)}$$

The Sn composition (Table 3.1) was subsequently calculated by the replacement of $a_0$, $C_{11}$, and $C_{12}$ in Equation 3.23 with their expressions from Equations 3.15, 3.16, and 3.17, respectively.

Table 3.1. The measured Sn content and lateral strain in the GeSn layer of samples S1, S2, and S3 using the GeSn peak position on the $\bar{2}\bar{2}4$ RSM.

| Sample | Sn content, $x$ (at. %) | Lateral strain, $\varepsilon_\parallel \times 10^{-3}$ |
|---|---|---|
| S1 | 6.8 | -7.4 |
| S2 | 6.9 | -0.4 |
| | 7.9 | -1.3 |
| S3 | 6.5 | -0.1 |
| | 7.3 | -0.8 |

As can be seen in Table 3.1, the measured RSMs provided an estimate of the Sn compositions of the GeSn layers that are close to the designed value of 6.6 at. %. Additionally, the lateral strain was seen to decrease with increasing GeSn layer thickness, which explained the decrease of the lattice parameter, $a_\perp$, in Figure 3.7. The increase of strain relaxation was accompanied by the enhanced Sn incorporation in the GeSn layers of samples S2 and S3. However, due to the relatively small change of the Sn content, the GeSn peaks that correspond to the regions of high and low Sn content on the RSM were strongly overlapped. In conjunction with increasing diffuse scattering around the GeSn peaks, this leads to an erroneous determination of the peak position and, as a result, of the Sn content and strain state. For example, while the peak position of the high Sn region on the RSMs in Figure 3.9 can be

determined with high accuracy, the low Sn peak is hindered by the diffuse scattering. Therefore, the theory of diffuse scattering due to misfit dislocations [61] was applied for the current samples to obtain a better estimate of Sn composition, strain, and density of misfit dislocations.

Figure 3.11 compares the measured (a) and simulated RSMs (b)-(d) for sample S2. In particular, the RSM in Figure 3.11b was calculated for a 400 nm thick GeSn layer with a uniform Sn composition of 7.1 at. %. The 60° MDs were located at the GeSn/Ge interface in order to simulate the strain relaxation that is the origin of the peak shift with respect to the line of pseudomorphic growth (R = 0). As can be seen, the diffuse scattering around the GeSn peak on the simulated RSM is much stronger as compared with that on the measured one. Since the peak widths, $\Delta Q_{\parallel}$ and $\Delta Q_{\perp}$, scale with the density of MDs, $\rho$, and the layer thickness, $d$, as $\sim\sqrt{\rho/d}$ [61], the large diffuse scattering suggested an overestimated density of MDs or underestimated GeSn layer thickness.

It is well known that for cubic crystals with low compressive lattice mismatch (< 2%), the 60° MDs are considered the dominant type of strain relieving dislocations [62]. Therefore, the RSM fitting was further improved by altering only the GeSn layer thickness, which was increased to 670 nm. This resulted in a reduced peak width (Figure 3.11c) that is comparable with that of the measured RSM. Yet, the comparison of the peak shapes of the simulated and measured RSMs suggested that the GeSn layer of sample S2 is composed of regions with different Sn content. Therefore, the RSM simulation was refined by altering the depth distribution of Sn.

Figure 3.11d shows the simulated RSM that was obtained assuming that the GeSn layer is composed of a bottom layer (BL), graded layer (GL), and top layer (TL). The Sn content is uniform in BL and TL, while gradually changes in GL. The simulated RSM in Figure 3.11d

displays the closest resemblance with the measured RSM in Figure 3.11a.

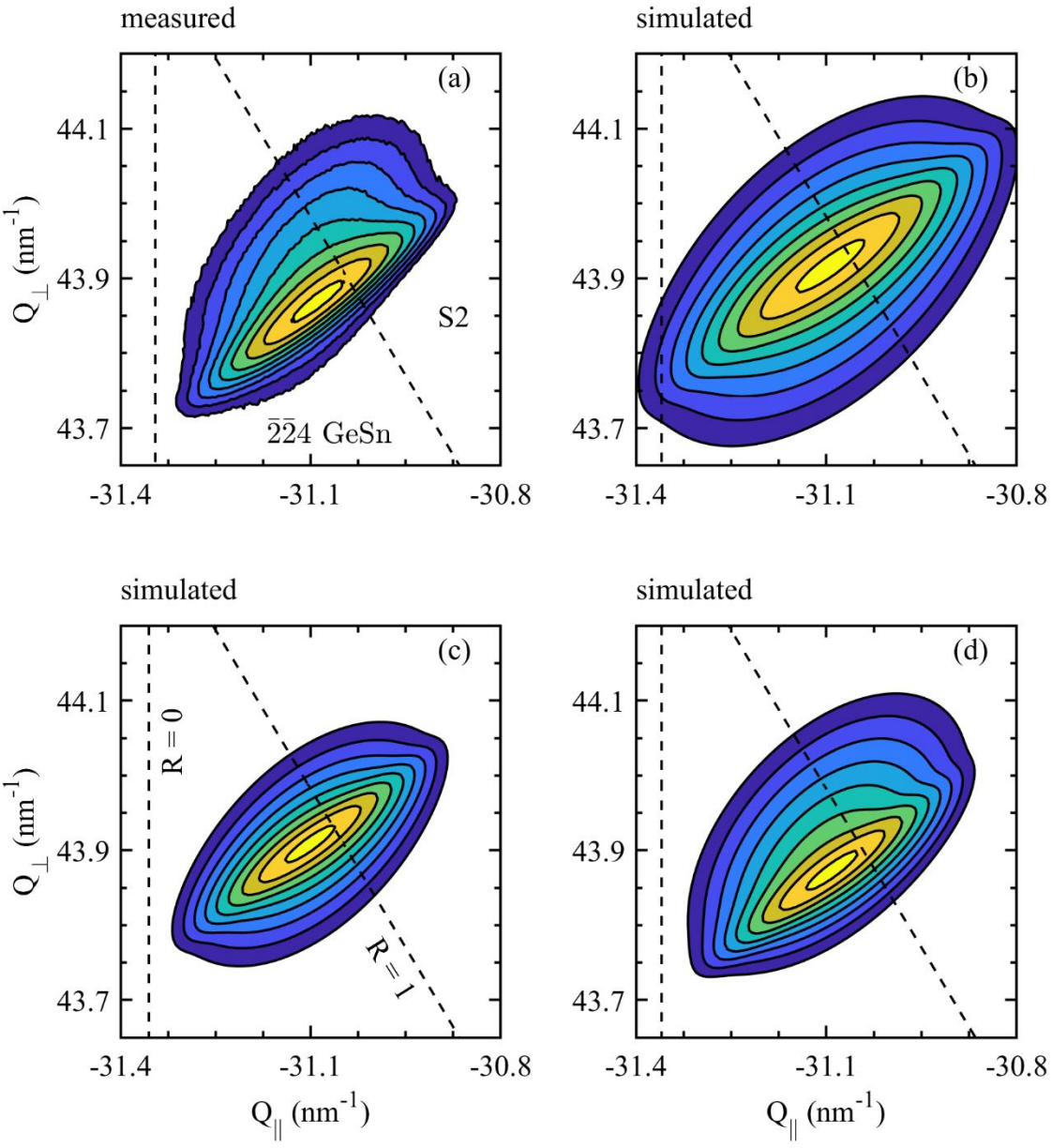


Figure 3.11. Experimental (a) and calculated (b)-(d) XRD RSMs from the GeSn layer of sample S2.

The RSM of sample S3 was simulated following the same procedure as for sample S2. The comparison of the measured RSM of sample S3 with its best fit is shown in Figure 3.12. For sample S1, the negligible strain relaxation in the GeSn layer is related to a small density of misfit

dislocations, which does not allow using the theory of X-ray diffuse scattering. However, as can be seen from Figure 3.9a, the GeSn peak shape of sample S1 is relatively narrow, which suggests the uniform distribution of Sn.

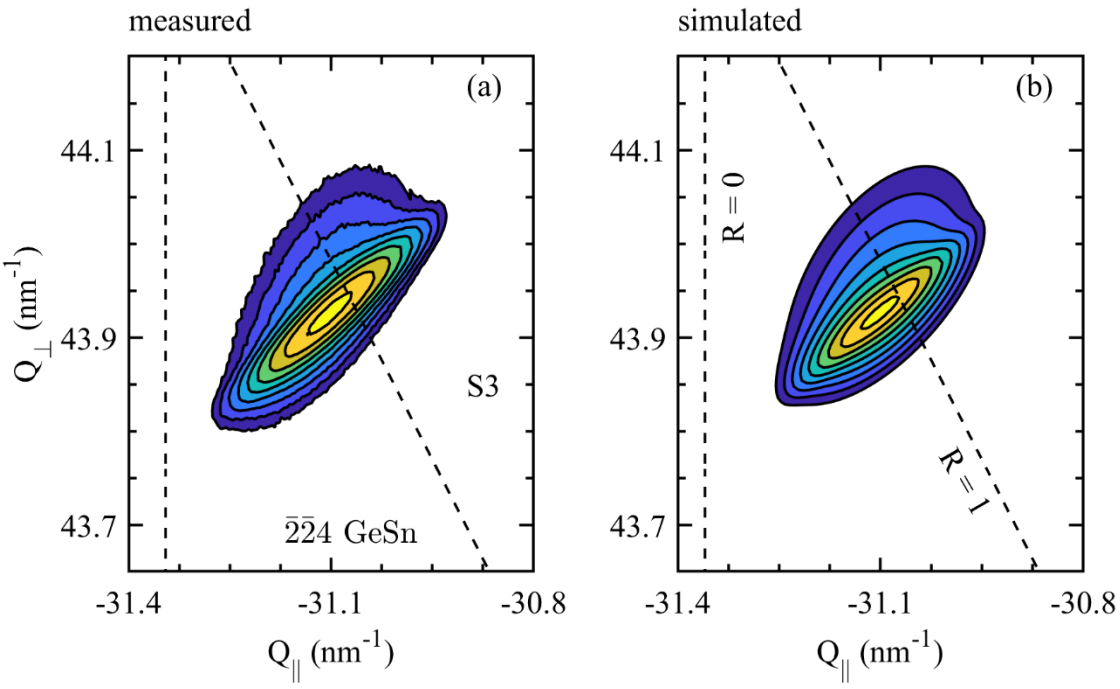


Figure 3.12. Experimental (a) and calculated (b)-(d) XRD RSMs from the GeSn layer of sample S3 [71].

Figure 3.13 compares the secondary ion mass spectrometry (SIMS) profiles measured for samples S1, S2, and S3, which in particular show the depth distribution of Sn in the GeSn layers. Evidently, the 125 nm thick GeSn layer of sample S1 can be characterized with a uniform Sn composition of 6.6 at. %. At the same time, three regions with distinct Sn composition can be seen for samples S2 and S3. Specifically, the thickness of the GeSn bottom region (BL) is close to 100 nm, and this has a uniform Sn content of ~6.9 and ~6.5 at. % for sample S2 and S3, respectively. For these samples, a 150 ± 20 nm thick region with graded Sn content follows the BL layer. The GeSn top region (TL) has a uniform Sn composition of 7.7

and 7.2 at. % for sample S2 and S3 and extends towards the surface over ~450 and ~850 nm, respectively. Figure 3.13 also compares the Sn composition determined from XRD measurements (solid black lines), which shows a good match between the XRD and SIMS results.

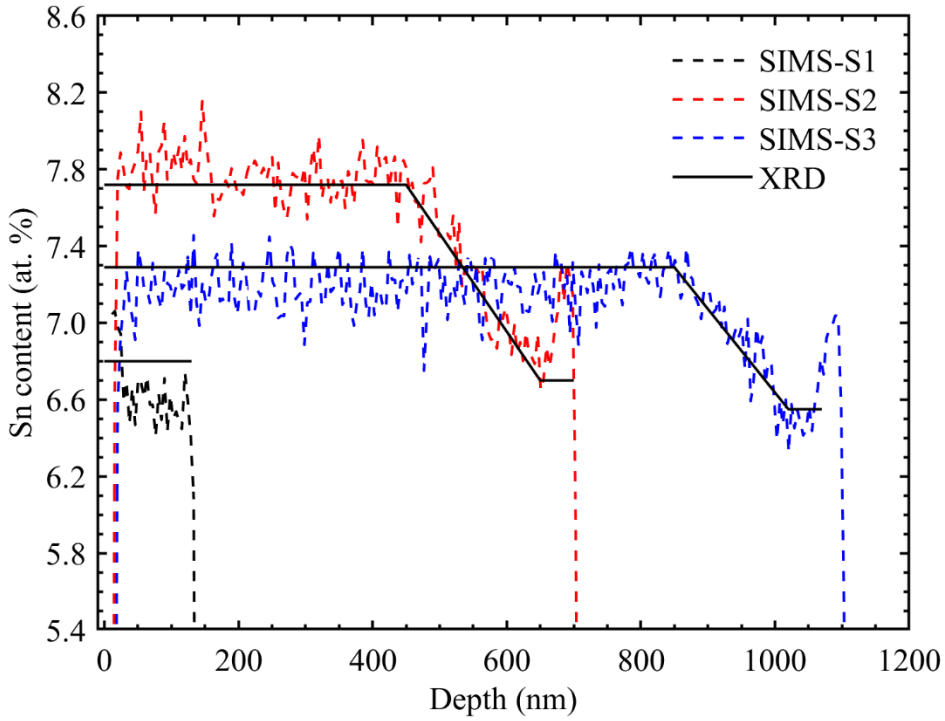


Figure 3.13. Concentration profiles of Sn across the GeSn layer obtained from SIMS (dashed line) and XRD RSMs (solid line) for samples S1, S2, and S3 [71].

## 3.4 X-ray diffraction characterization of Sn incorporation in GeSn layers under compressive strain

The strain-dependent Sn incorporation is quantified in more detail by studying several GeSn layers with different strain states and Sn compositions. For example, Figure 3.14 compares the RSMs of samples S1, S4, and S5, for which the GeSn peak is shifting along the isocomposition line (solid red line) as the compressive strain in the GeSn layer decreases. This is a companied with the splitting of the GeSn peak, which indicates the formation of a region

with higher Sn composition in the GeSn layer. On the RSM, the Sn-rich peak is located at the lower $Q_z$ values and its intensity increases due to the increasing layer thickness.

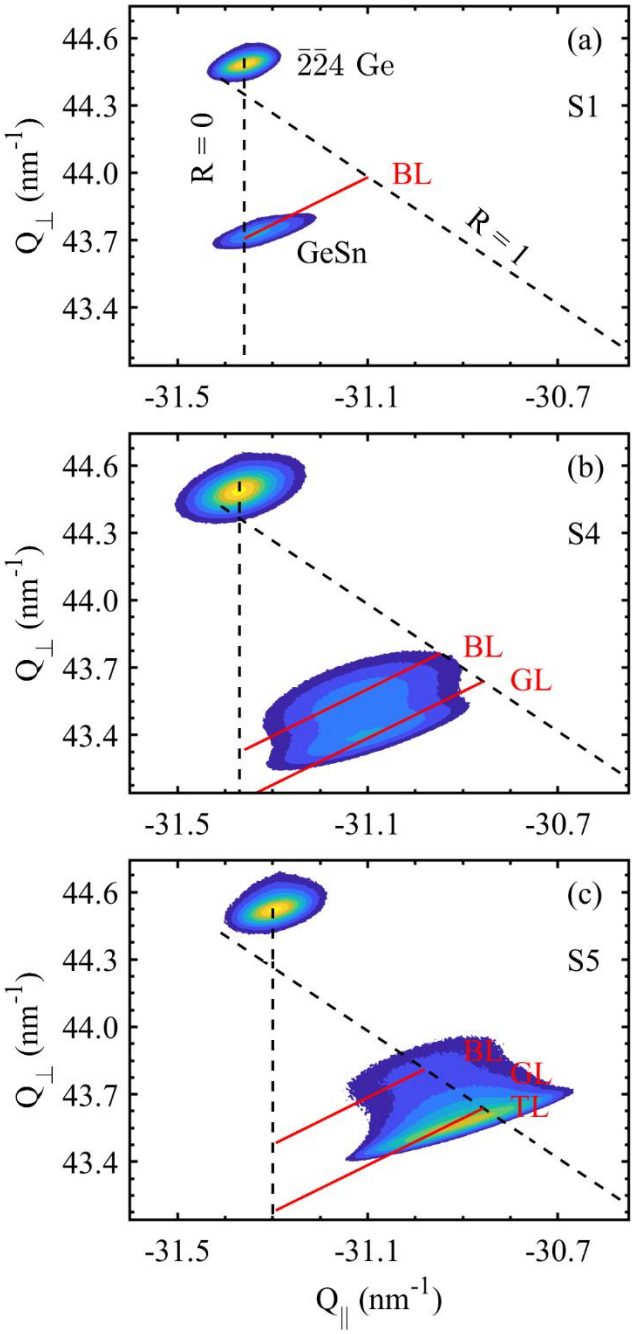


Figure 3.14. Measured $\bar{2}\bar{2}4$ RSMs for sample S1 (a), S4 (b), and S5 (c). The dashed vertical (R = 0) and inclined (R = 1) lines denote the fully strained and fully relaxed $Ge_{1-x}Sn_x$ alloys. The inclined red solid lines are the isocomposition lines.

The splitting of the GeSn peak on the RSM is saturated after the GeSn layer is completely relieved of strain. Accordingly, the GeSn peaks were associated with the BL region for sample S1, the BL and GL regions for sample S4, and the BL, GL, and TL regions for sample S5. The location of the BL, GL, and TL peaks on the RSMs suggested that most MDs were located at the BL/Ge interface, which is reflected in the large shift of the BL peak for samples S4 and S5. On the contrary, the minor shift of the GL and TL spots with respect to the BL indicated the low density of dislocations at the interfaces between BL and GL and between GL and TL.

For all samples, the degree of strain relaxation and the corresponding density of dislocations are shown in Figure 3.15 for the BL GeSn layers. In particular, the degree of strain relaxation was defined as follows,

$$R_{BL} = 100 \times \frac{a_{\parallel} - a_s}{a_0 - a_s} \qquad \text{(Equation 3.24)}$$

where $a_{\parallel}$ is the measured lateral lattice parameter of the GeSn BL layer, $a_0$ is the lattice parameter of a bulk GeSn BL, and $a_s$ is the lateral lattice parameter of the Ge buffer. Accordingly, $R_{BL} = 0\%$ and $R_{BL} = 100\%$ correspond to a fully relaxed and fully strained GeSn layer, respectively. Figure 3.15a shows that the magnitude of $R_{BL}$ for different samples spans over a wide range from 10 to 95%. Also, the increase of $R_{BL}$ is accompanied by an increase in the density of MDs, $\rho$. For strongly relaxed GeSn layers, the magnitude of $\rho$ approaches the dashed line in Figure 3.15b, which projects the density of MDs in a fully relaxed ($\varepsilon_{res} = 0$) GeSn layer and was calculated according to the following expression [65],

$$\varepsilon_{res} = f - b_x \rho \qquad \text{(Equation 3.25)}$$

where $\varepsilon_{res}$ is the residual strain, $f$ is the lattice mismatch, and $b_x = a_s/2\sqrt{2}$ is the strain relieving component of Burger's vector for a 60° MD.

For completeness, Figure 3.16 shows the lattice parameters of the GeSn BL in response

to strain relaxation. It can be seen that, under compressive strain, the unit cell in the GeSn layer is tetragonally distorted so that the vertical lattice parameter, $a_{\perp}$, is larger than the lateral lattice parameter, $a_{\parallel}$. With the increase of strain relaxation, both $a_{\perp}$ and $a_{\parallel}$ approach the calculated dashed line, which depicts the lattice parameter for the unstrained GeSn alloy.

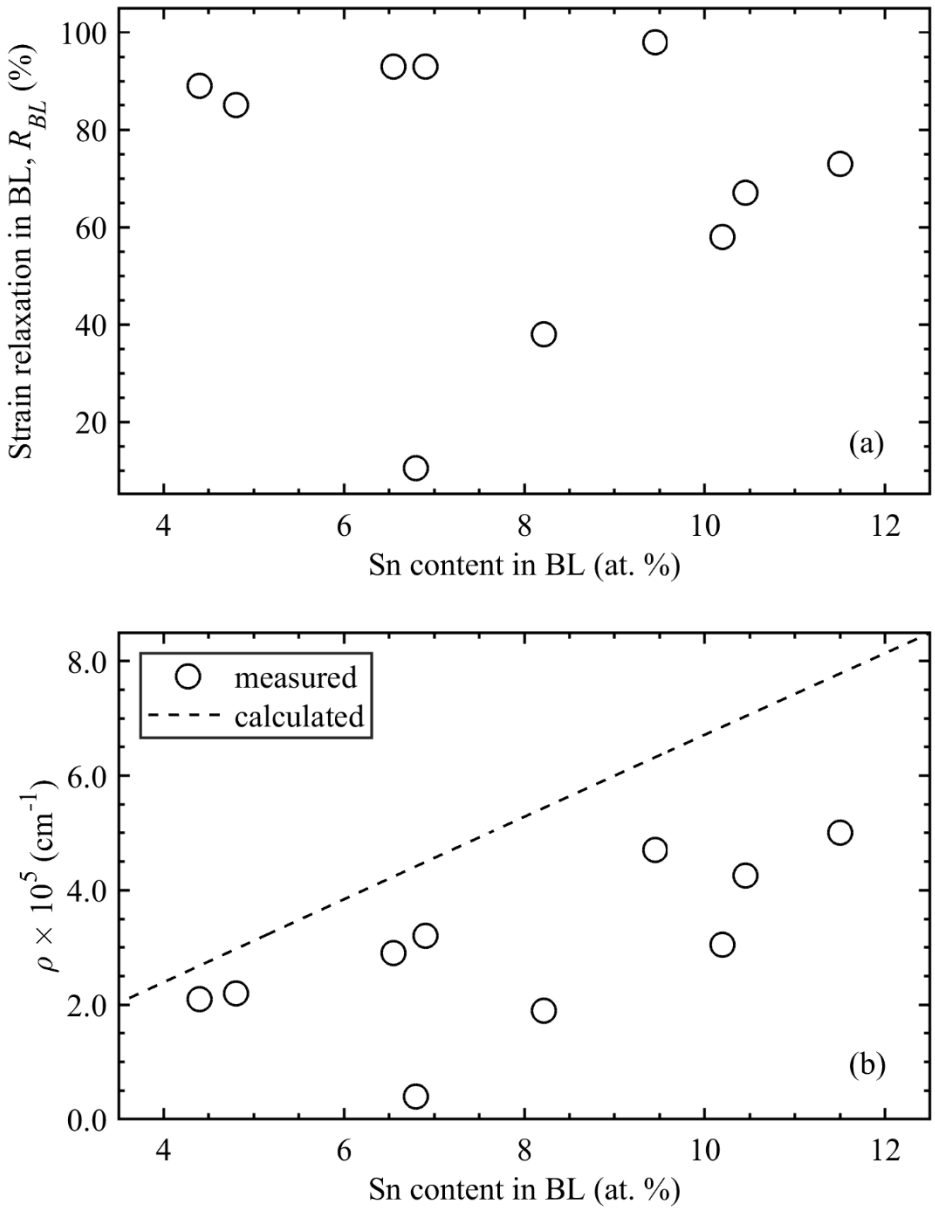


Figure 3.15. The percentage relaxation of strain (a) and the misfit dislocations density (b) in the bottom region of GeSn epilayers [74].

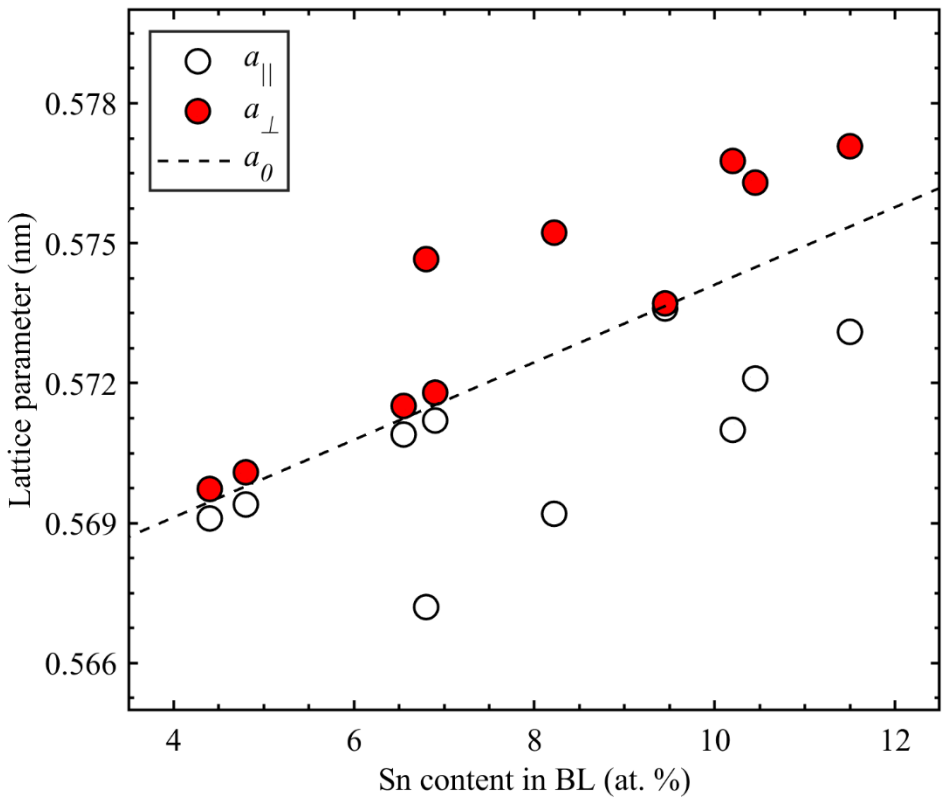


Figure 3.16. Measured lattice parameter for the GeSn BL layers.

For all samples, the surplus of Sn concentration (ΔSn) in the GeSn TL with respect to the BL can be seen in Figure 3.17a. As can be seen, the magnitude of ΔSn increases from 0.5 to 4.8 at. % with the increasing Sn composition in the GeSn TL from 5 to 15 at. %, respectively. Moreover, the Sn content in the GeSn layer strongly depends on the degree of strain relaxation of the BL, as previously observed elsewhere [33], [63]. The maximum excess of Sn in a GeSn layer ($\Delta Sn^{max}$) is expected at $R_{BL}$ = 100%. Therefore, for the GeSn layers under larger residual compressive strain, the surplus of Sn is reduced by a factor of $R_{BL}$, which roughly can be described by the following equation $\Delta Sn = \Delta Sn^{max} \times R_{BL}$. Accordingly, for partially relaxed GeSn layers, the anticipated ΔSn at $R_{BL}$ = 100% was approximated as $\Delta Sn/R_{BL}$ (filled square symbols in Figure 3.17a).

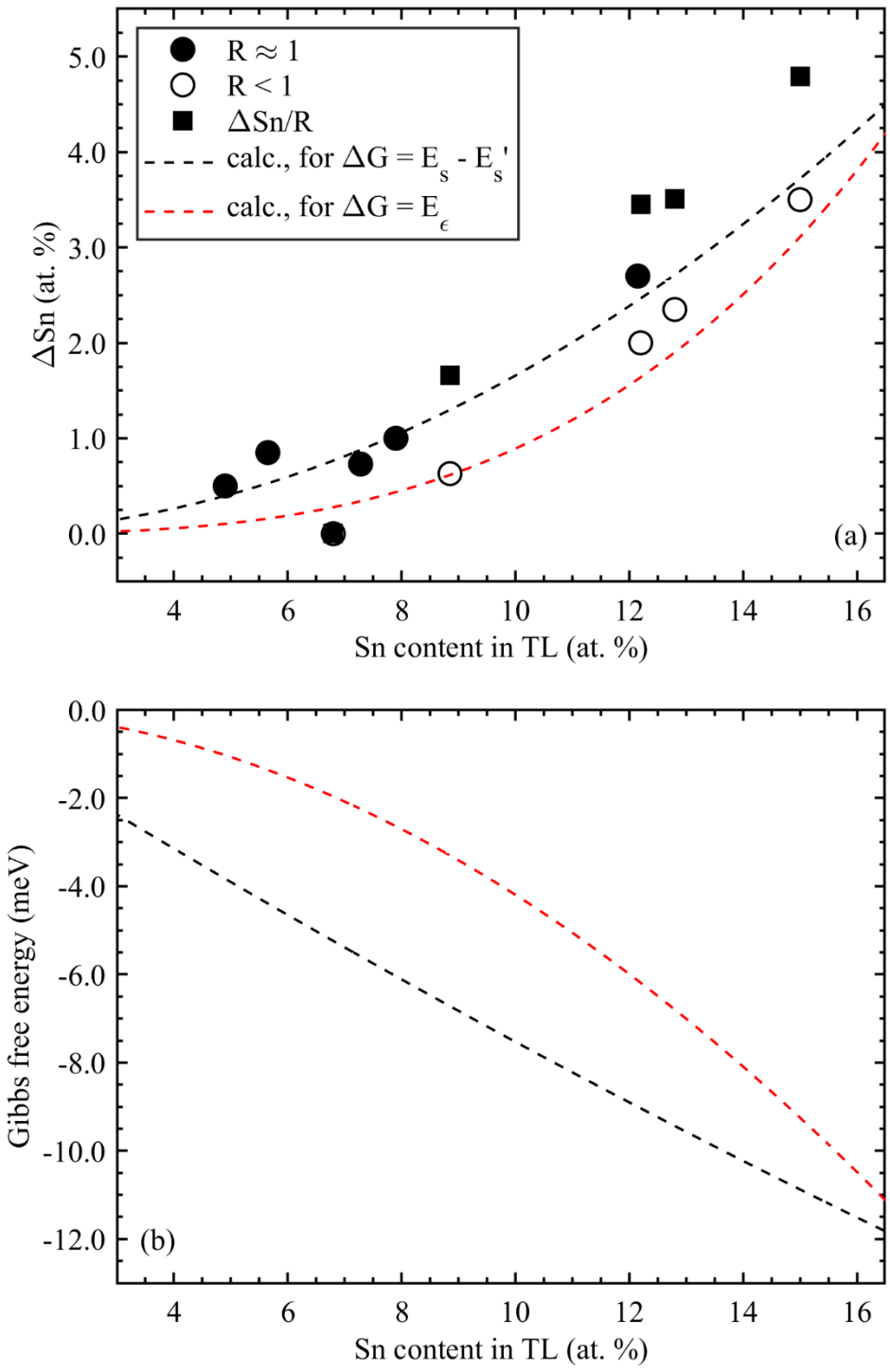


Figure 3.17. (a) The measured excess of Sn in the GeSn TL layers (symbols) of all samples and the calculated Sn segregation from compressively strained GeSn layer (dashed lines) as a function of Sn composition. The filled and empty symbols correspond to the GeSn layers with complete and partial strain relaxation, respectively. (b) The Gibbs free energy in compressively strained GeSn alloys [74].

Given the unchanged growth conditions of the GeSn during the layer deposition, it is more appropriate to focus the discussion on the suppressed Sn incorporation in the highly strained GeSn BL region. For a fully strained GeSn layer on Ge substrate, Sn can be considered as an oversized solute atom in the Ge matrix. Therefore, the high compressive strain in the BL may prevent the efficient incorporation of Sn in comparison with the incorporation into the strain relaxed TL. Consequently, the Sn atoms may segregate towards the sample surface during the growth of the BL.

An appropriate model that accounts for the segregation of Sn was presented in Ref. [75] for Sn-doped GaAs layers. It was shown that under equilibrium conditions, the surface concentration of Sn ($x_s$) is related with the bulk concentration ($x$) by the following equation,

$$x_s = x \exp\left(-\frac{\Delta G_{seg}^0}{kT}\right) \qquad \text{(Equation 3.26)}$$

where $\Delta G_{seg}^0$ is the total Gibbs free energy of Sn segregation, $k$ is the Boltzmann constant, and $T$ is the growth temperature of the GeSn layer. The total Gibbs free energy in Equation 3.26 is generally composed of the bond-breaking and strain energy terms. However, due to the low melting point of Sn (232 °C) and the high growth temperature of the GeSn layer (300 °C), the bond-breaking contribution to the $\Delta G_{seg}^0$ was omitted. Therefore, the total Gibbs free is solely associated with the strain state of the GeSn layer. The strain energy for substitutional Sn in the strained lattice ($a_{GeSn} = a_{Ge}$) of the GeSn BL is given in Ref. [75] as follows,

$$E_s = -\frac{24 K_{Sn} G_{GeSn} r_{Sn} r_{GeSn} (r_{Sn} - r_{Ge})^2}{3K_{Sn} r_{Sn} + 4G_{GeSn} r_{GeSn}} \qquad \text{(Equation 3.27)}$$

where $K_{Sn}$ = 4.25 × $10^{10}$ N/m$^2$ is the bulk modulus of Sn, $G_{GeSn}$ is the shear modulus of GeSn with $G_{Ge}$ = 4.10 × $10^{10}$ N/m$^2$ and $G_{Sn}$ = 1.99 × $10^{10}$ N/m$^2$, $r_{Sn}$ = 0.139 nm is the covalent radius of Sn, and $r_{Ge}$ = 0.120 nm is the covalent radius of Ge.

According to Equation 3.27, the segregation of Sn is expected from both the strained BL and relaxed TL regions of the GeSn layer due to the covalent radii difference term. However, the measured ΔSn in Figure 3.17 only reflects the relative difference of Sn composition between the TL and BL layers due to the distinct strain state. Therefore, the strain energy term $E_s'$ that contains the covalent radii difference ($r_{Sn} - r_{GeSn}$), which in practice describes the Sn segregation from a strain relaxed GeSn layer, is additionally subtracted from the total Gibbs free energy, so that $\Delta G_{seg}^0 = E_s - E_s'$, and

$$E_s' = -\frac{24K_{Sn}G_{GeSn}r_{Sn}r_{GeSn}(r_{Sn} - r_{GeSn})^2}{3K_{Sn}r_{Sn} + 4G_{GeSn}r_{GeSn}} \qquad \text{(Equation 3.28)}$$

where $r_{GeSn}$ is the average covalent radius in the GeSn TL layer. Alternatively, the strain energy per atom in a compressively strained GeSn lattice on Ge can be approximated using Equation 1.2 in the following form [65],

$$E_\varepsilon = -\frac{1}{N}\frac{2G_{GeSn}(1+\nu)}{(1-\nu)}\varepsilon_\parallel^2 V \qquad \text{(Equation 3.29)}$$

where $N$ = 8 is the number of atoms in the unit cell; $\nu$ = 0.27 is the Poisson's ratio, and $V = a_0^3$ is the volume of the unit cell.

The calculated Sn segregation ($\Delta Sn = x_s - x$) from compressively strained GeSn BL layers is shown in Figure 3.17a. The magnitude of ΔSn is calculated according to Equation 3.26 for both $\Delta G_{seg}^0 = E_s - E_s'$ and $\Delta G_{seg}^0 = E_\varepsilon$, which are shown with the black and red dashed lines, respectively. As can be seen, the segregation model accurately describes the measured excess of Sn in the GeSn TL. This close agreement indicated that the excess of Sn in the strain relaxed GeSn TLs is indeed connected with the Sn content that is not incorporated in the GeSn BL that is under large compressive strain. The corresponding Gibbs free energies $\Delta G_{seg}^0 = E_s - E_s'$ and $\Delta G_{seg}^0 = E_\varepsilon$ used for simulating the segregation of Sn are additionally compared in Figure 3.17b.

The magnitude of $\Delta G_{seg}^{0}$ in compressively strained $Ge_{1-x}Sn_x$ alloys increases with the Sn composition due to the increasing covalent radii and lattice mismatch in Equations 3.27 and 3.29, respectively. The good correlation between the Gibbs free energies $\Delta G_{seg}^{0} = E_s - E_s'$ and $\Delta G_{seg}^{0} = E_\varepsilon$, as well as between the measured and calculated ΔSn, justified the adequacy of the model for Sn segregation.

The demonstrated interplay between the Sn incorporation and compressive strain relaxation in GeSn layers is extremely important. For instance, it can be utilized for designing GeSn/Ge heterostructures with enhanced Sn composition and improved structural quality, as well as predictable optical and electronic properties. The model also explains the uniform Sn composition in a compressively strained GeSn layer with a thickness lower than the critical thickness. The enhanced incorporation of Sn is initiated once the strain relaxation begins, which results in a compositionally GL above the BL. Moreover, after the compressive strain in GeSn is relaxed to an equilibrium value, which corresponds to the TL region, the incorporation of Sn becomes uniform and enhanced with respect to the strained BL.

The thickness of the BL region of the GeSn was estimated within the framework of the Matthews and Blakeslee (MB) [56] and People and Bean (PB) [57] models according to Equations 1.5 and 1.7, respectively. The calculated critical thicknesses are shown in Figure 3.18. Additionally, the thicknesses of the BL layers for several samples were measured from the SIMS profiles (symbols in Figure 3.18), which tend to align along the curve calculated using the People and Bean model. The agreement of the PB model with the experimental data is often reported elsewhere [76]. According to the PB model, the thickness of the GeSn BL of all samples is expected in the range from 580 to 40 nm, which corresponds to the measured range of lattice mismatches from 0.49 to 1.51%.

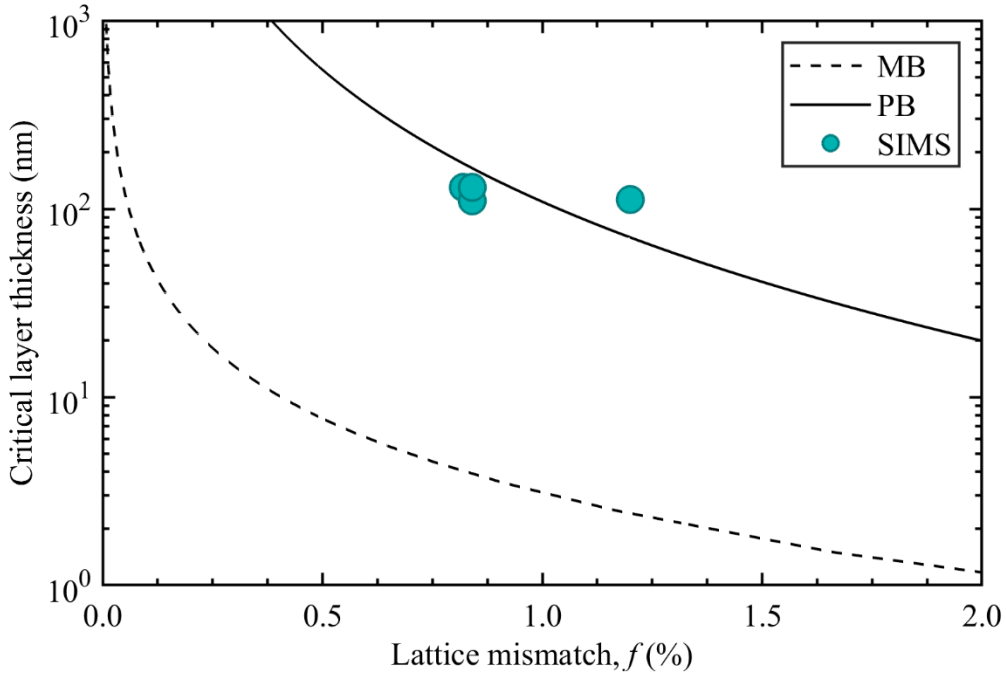


Figure 3.18. The critical thickness for strain relaxation according to the Matthews and Blakeslee (MB) [56] (dashed line) and People and Bean (PB) [57] (solid line) models. Symbols show the thickness of the GeSn BL layers from the SIMS profiles of several samples [74].

The thickness of the GL region ($h_{GL}$) of the GeSn was estimated from the SIMS profiles in Figure 3.13 as well as from the SIMS profiles in Ref. [63]. For the given range of Sn composition, the GL region extends above the BL by about 160 ± 25 nm, which is followed by a uniform Sn content TL layer. Because of only a small variation of $h_{GL}$ and the large change of ΔSn (Figure 3.17a) for a large compositional range (from about 4 to 12 at. %), the gradient of Sn composition ($\beta$) in the GeSn GL layer is also a function of the nominal Sn composition and can be estimated by, $\beta = \Delta Sn/h_{GL}$.

## 3.5 Summary

X-ray diffraction was shown for characterization of Sn content, strain state, and density of defects in GeSn layers. It was demonstrated that the BL and GL regions of the GeSn layer are

correlated with the specific thicknesses for strain relaxation, where the strain relieving misfit dislocations are localized. The TL region of the GeSn layer was considered relatively free of structural defects. The large compressive strain in the GeSn BL resulted in a suppressed Sn incorporation, which was shown to agree well with the model of solute atom segregation. Therefore, the spontaneously formed regions with distinct Sn compositions are the fingerprint for the strain state in the GeSn layers.

# Chapter 4: Structural stability of GeSn/Ge heterostructures under thermal annealing

## 4.1 Introduction

Germanium-tin alloys are exciting semiconductors for CMOS compatible photonic applications due to their direct bandgap at Sn concentrations larger than 8-10 at. % [24]. At the same time, under the equilibrium growth conditions, the solid solubility of Sn in Ge is less than 1.1 at. % and the eutectic temperature is as low as 231.1 °C. Nonetheless, the use of non-equilibrium growth techniques, such as MBE and CVD, makes it possible to grow GeSn structures with higher Sn content [30], [63].

The device fabrication process typically involves several rounds of thermal treatment, such as during dopant activation and deposition of contacts. Given the low eutectic point of GeSn, its crystalline structure may undergo severe transformations at elevated temperatures. Recently, good thermal stability was shown for the pseudomorphic GeSn layers grown by CVD on Ge at temperatures below 400 °C [77]. The noticeable Sn diffusion was reported for annealing temperatures above 500 °C, while the annealing for 30 min below 450 °C did not affect the structural integrity of the GeSn layers. This is in good agreement with the Ge-Sn interdiffusion at 500 °C in Ref. [78]. Similarly, the onset of strain relaxation for annealing temperatures higher than 440 °C was reported in Ref. [79] for GeSn/Ge heterostructures grown by MBE at 150 °C, while Sn surface segregation and clustering was observed for temperatures above 580 °C. In contrast, a sudden Sn segregation in GeSn layers was reported in Ref. [80] for annealing temperatures higher than 400 °C, provided that the strain relaxation in the GeSn layer is larger than 79%. This result is counterintuitive, however, if considering the enhanced Sn incorporation in the GeSn layers with compressive strain relaxation during the growth [33], [63].

Apparently, the high and low temperature for Sn diffusion in pseudomorphic and relaxed samples, respectively, suggest the key role of the density of structural defects, such as dislocations, on the Sn migration processes.

The role of threading dislocations (TDs) on the migration of Sn atoms in GeSn layers was investigated in Ref. [81]. It was shown that the propagating TDs toward the surface are the pathways for Sn transport that also facilitate the phase separation. Therefore, a quantitative analysis between the strain relaxation, density of dislocations, and Sn segregation during thermal annealing is reported below.

## 4.2 Sample descriptions

The samples were grown on Si(001) substrates by CVD using an ASM Epsilon 2000 Plus reduced pressure system. Initially, a 700 nm thick Ge buffer layer was deposited on the Si substrate. The GeSn layers with 8 and 9 at. % nominal Sn composition were grown at ~300 °C using $GeH_4$ and $SnCl_4$ as germanium and tin gaseous precursors, respectively. The deposition time was controlled to achieve GeSn layers with different thicknesses and varying strain state. After the growth, each sample was diced into pieces. Different pieces were annealed at 300 °C in a vacuum furnace for 2, 4, or 8 hours. Table 4.1 shows the structure of all samples.

Table 4.1. The measured structural parameters of the GeSn layer of all samples.

| | Sn content (at. %) | | | Strain relaxation in BL (%) | | GeSn thickness (nm) | | |
|---|---|---|---|---|---|---|---|---|
| | BL | GL | TL | as-grown | annealed | BL | GL | TL |
| A1 | 7.8 | - | - | 5.4 | 34.5 | 90 | - | - |
| A2 | 9.1 | - | - | 19.5 | 45.5 | 120 | - | - |
| A3 | 8.8 | 8.8 - 9.8 | - | 44.1 | 80.5 | 130 | 170 | - |
| A4 | 9.4 | 9.4 - 12.2 | 12.2 | 91.0 | - | 130 | 170 | 450 |

## 4.3 Characterization of the strain state, Sn segregation, and density of defects in GeSn/Ge heterostructures subjected to thermal annealing

As was shown in the previous chapter, the growth of compressively strained GeSn layers is typically accompanied by a spontaneous change of composition with the beginning of strain relaxation above the critical layer thickness. This resulted in GeSn BL, GL, and TL regions, for which the Sn composition was uniform-suppressed, graded, and uniformed-enhanced, respectively. As was discussed, GeSn epitaxy on Ge suffers from surface segregation of Sn atoms during the growth, which explains the formation of distincnt-composition GeSn regions. This phenomenom is dictated by the magnitude of compressive strain and is considered spontaneous.

The effect of thermal annealing on the structural quality of the GeSn layers was initially studied by measuring the X-ray diffraction $\omega/2\theta$ spectra from 004 planes. Figure 4.1 compares the $\omega/2\theta$ spectra measured before and after annealing captured within a wide angular range. The solid and dashed vertical lines on the measured spectra indicate the positions of the Ge and GeSn peaks, respectively, on the $\omega/2\theta$ scans measured before the annealing. After each annealing treatment, the Ge peak is seen in the same angular position, which indicates that the strain state of the Ge buffer was not influenced by the annealing treatment.

The GeSn peaks on the $\omega/2\theta$ scans of the as-grown samples reflect the uniform composition BL region for samples A1 (Figure 4.1a) and A2 (Figure 4.1b), the BL and graded composition GL regions for sample A3 (Figure 4.1c), and the BL, GL, and uniform composition TL regions for sample A4 (Figure 4.1d). Accordingly, the observed bifurcation of the GeSn peak for sample A4 was related to the Sn-rich and low-Sn TL, GL, and BL, respectively, so that the TL peak was seen at lower scattering angles due to the higher Sn content. Since the total

thickness of the BL and GL regions was much smaller than that of TL (Table 4.1), the intensity of the BL/GL peak was also significantly lower.

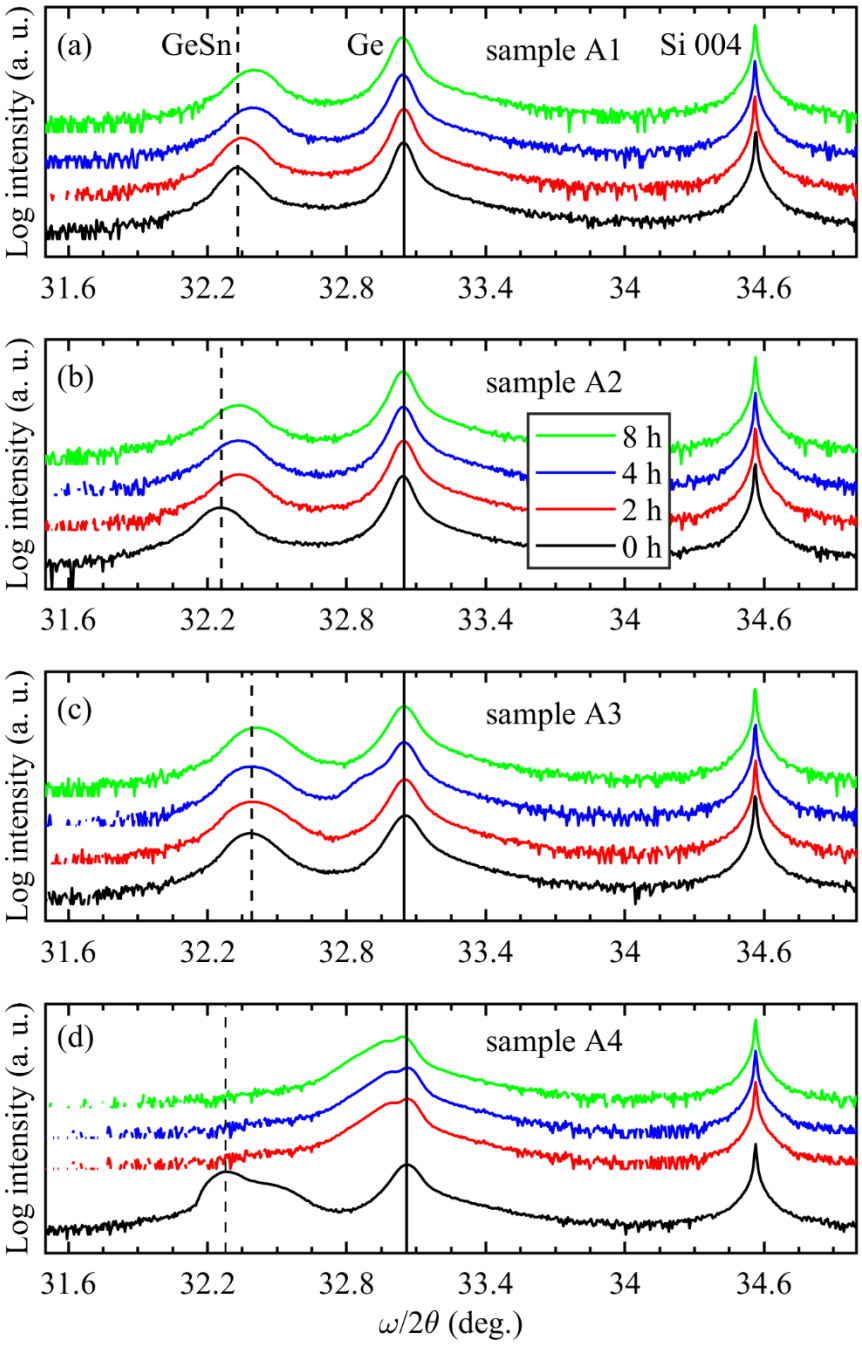


Figure 4.1. X-ray diffraction ω/2θ scans measured across the symmetrical 004 reflection of the as-grown and annealed samples A1 (a), A2 (b), A3 (c), and A4 (d). The vertical solid and dashed lines mark the positions of the Ge and GeSn peaks on the spectra of the as-grown samples.

After the annealing of samples A1, A2, and A3, the GeSn peak was slightly shifted toward the larger scattering angles with respect to the GeSn peak of the as-grown sample (vertical dashed line) in response to decreasing vertical lattice parameter, $a_{\perp}$. The annealing of sample A4 for two, four, and eight hours led to a much larger shift of the GeSn peak, which was found close to the peak from the Ge buffer. Evidently, this signifies the severe loss of Sn from the GeSn layer of sample A4. A similar peak corresponding to the GeSn region with low Sn content was seen on the ω/2θ scan for sample A3 annealed for four hours. However, unlike for sample A4, the GeSn region with high Sn content was also observed. The formation of the regions with low Sn content after the annealing of samples A4 and A3 suggested Sn segregation for those samples. Interestingly, Sn segregation was not identified for sample A3 annealed for two and eight hours.

The Sn composition and strain state evolution in the GeSn layers were resolved from the XRD RSMs from the asymmetrical $(\bar{2}\bar{2}4)$ planes. Figure 4.2 shows the measured RSMs in the order of increasing annealing time from left to right. The GeSn layers on the RSMs of samples A1 (Figure 4.2a) and A2 (Figure 4.2b) are seen as single peaks close to the vertical dashed line (R = 0). The GeSn peak for these samples is marked as BL, and are correlated to a uniform composition GeSn region. For sample A3 shown in Figure 4.2c, the GeSn peak is located at a larger $Q_{\parallel}$ with respect to the vertical dashed line (R = 0), indicating compressive strain relaxation. Moreover, the GeSn peak is slightly broadened in the $Q_{\perp}$ direction due to the contribution from the BL and GL areas of the GeSn layer that have distinct Sn composition. An additional GeSn peak corresponding to a GeSn region with the Sn molar fraction below 1 at. % is seen for sample A3 annealed for four hours, which agrees with the observations on the ω/2θ scan in Figure. 4.1c.

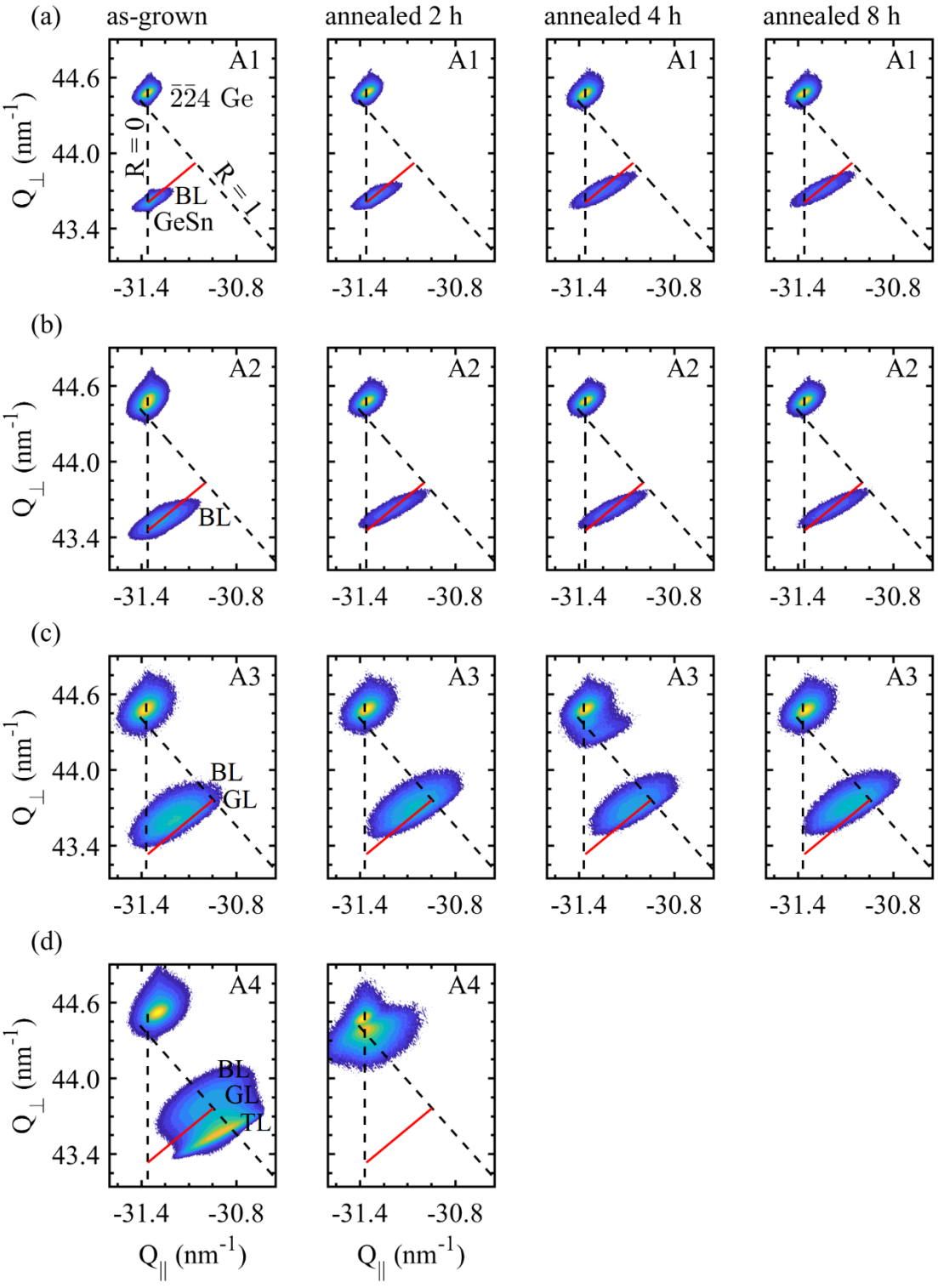


Figure 4.2. X-ray diffraction RSMs measured across the Ge $\bar{2}\bar{2}4$ reflection for sample A1 (a), A2 (b), and A3 (c), and A4 (d) before and after annealing [82].

The RSMs of sample A4 are shown in Figure 4.1d. The GeSn peak on the RSM measured before the annealing treatment is located on the line of complete strain relaxation (R = 1). As on the RSM of sample A3, the GeSn peak is composed of different composition regions, which are marked on the RSM as BL, GL, and TL. After annealing for two hours, only the GeSn peak corresponding to Sn composition of 1 at. % was seen on the RSM. The RSMs for sample A4 annealed for four and eight hours were not measured since the ω/2θ scans for these samples are identical to that annealed for two hours.

For all samples, the positions of the GeSn peaks corresponding to the BL regions are summarized in Figure 4.3. As can be seen, the thermal annealing resulted in the peak shift along the isocomposition lines Sn = 8 at. % for sample A1 and Sn = 9 at. % for samples A2 and A3. This indicates that the Sn composition was not altered during the annealing. It should be noted that the data for sample A3 annealed for four hours belong to the dark area in Figure 4.4a.

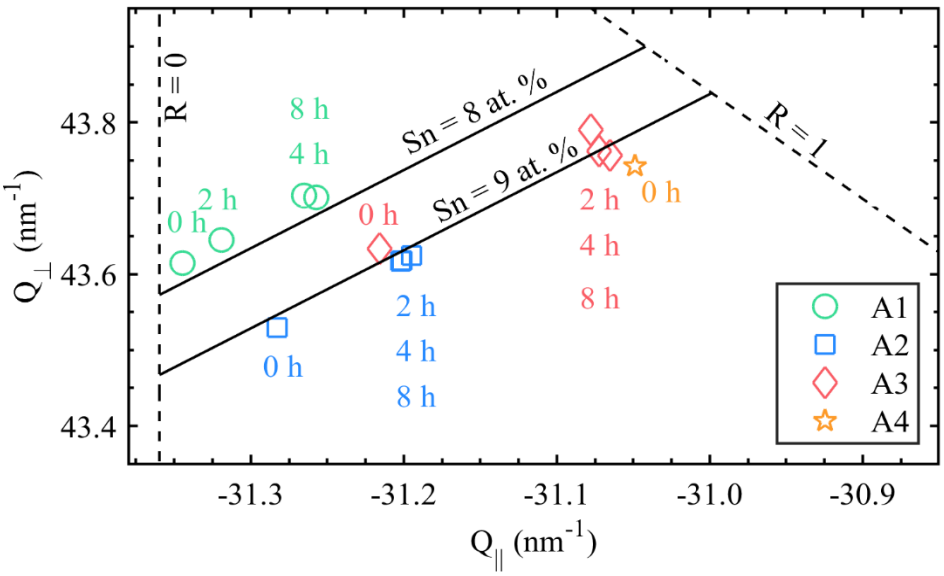


Figure 4.3. The measured positions of the GeSn BL peaks on the $\bar{2}\bar{2}4$ RSMs. The dashed vertical (R = 0) and inclined (R = 1) lines denote the fully strained and fully relaxed $Ge_{1-x}Sn_x$ alloys. The inclined solid lines are the isocomposition lines.

Selective XRD measurements were performed in order to identify the origin of low Sn content peak on the RSM of sample A3 annealed for four hours. The optical micrograph for this sample is shown in Figure 4.3a. As can be seen, several bright spots, presumably related to Sn segregation [81], appeared on the sample surface after the annealing treatment. Therefore, the sample was diced into smaller pieces, so that the spot area was separated from the dark region. Thereafter, the XRD measurements were performed for each sample piece separately.

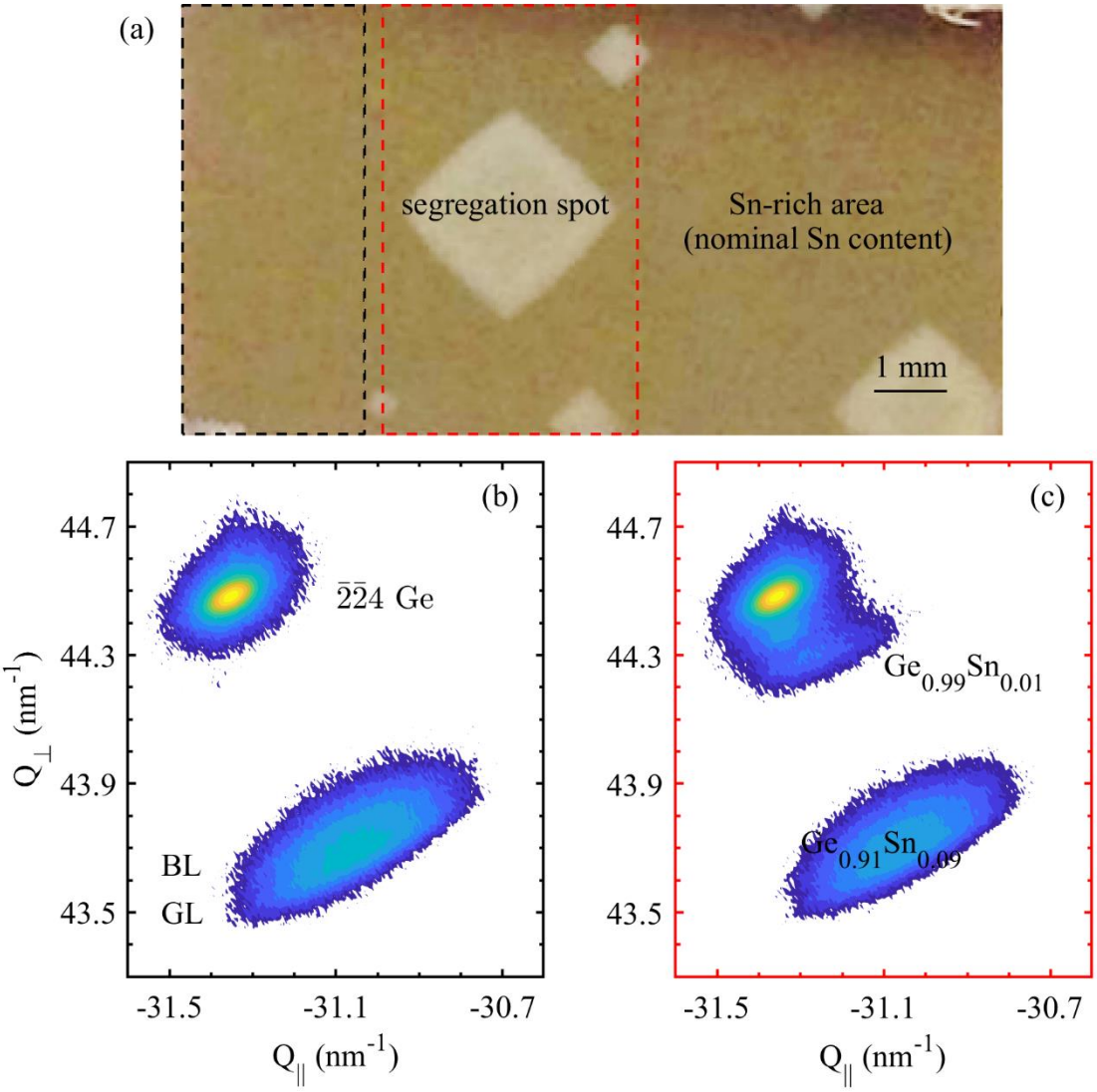


Figure 4.4. The optical micrograph of sample A3 annealed for four hours (a) and the $\bar{2}\bar{2}4$ RSMs measured within the dark (b) and spotted (c) areas.

Figure 4.4b shows the corresponding $\bar{2}\bar{2}4$ RSM measured inside the dark region on the sample surface, which on the optical micrograph is enclosed with the dashed black line. Expectedly, only the GeSn peaks corresponding to the BL and GL with nominal Sn content can be seen on the RSM. In contrast, on the RSM measured within the area enclosed with the dashed red line, which contain both the bright and dark regions, the low Sn content $Ge_{0.99}Sn_{0.01}$ peak can be seen along with the nominal Sn composition BL and GL peaks. This unambiguously allowed the emergence of the bright spots on the sample surface to be assigned with Sn out-diffusion from the GeSn layer. According to the absence of Sn segregation for samples A1 and A2, as well as the occasional Sn segregation for sample A3 and the complete loss of Sn for sample A4, it was concluded that the onset of Sn segregation is strongly related with the compressive strain relief in the GeSn layer, which on the RSMs is reflected on the GeSn peak shift toward the relaxation line (R = 1).

The surface morphology within the dark area and the segregation spot of sample A3 annealed for four hours was studied using AFM. Additionally, Figure 4.5a shows the surface of the as-grown sample A3, which was used as a reference image. Hereby, the surface of the as-grown sample was characterized with the root mean square (RMS) roughness of 0.8 nm and a crosshatch pattern that is typical for strain relaxation in planar films grown on mismatched substrates [83], [84]. The crosshatch pattern for an epitaxial layer grown on the (001) plane is composed of troughs and ridges that propagate along the <110> crystallographic directions (as marked in Figure 4.5a with white arrows), which agrees with the line directions of misfit dislocations (MDs) that are typically located at the film/substrate interface. Accordingly, the formation of these surface undulations was attributed to the varying strain field produced by the MDs [84].

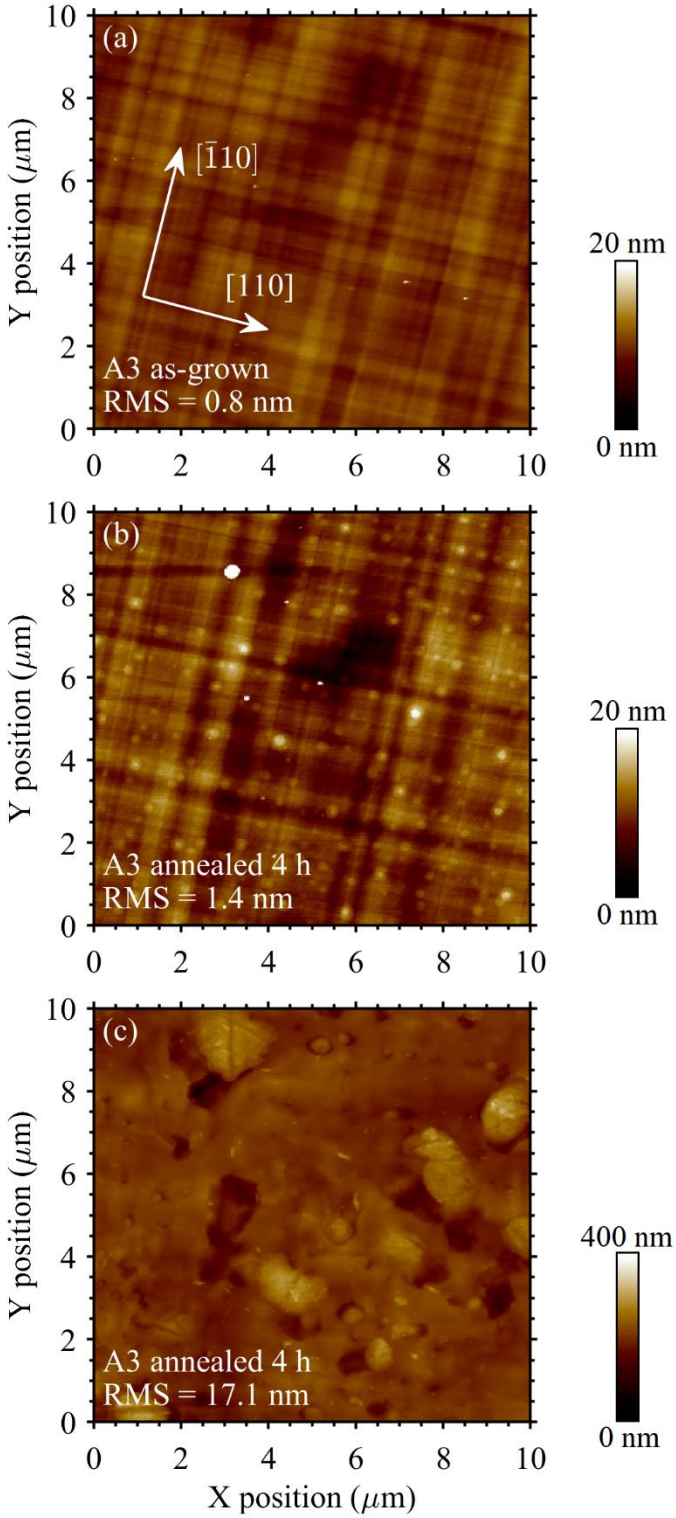


Figure 4.5. The surface morphology for sample A3 obtained by AFM for the (a) as-grown sample and (b), (c) after the annealing for four hours [82].

Figure 4.5b shows the AFM image for sample A3 annealed for four hours and measured within the off-spot area (the dark region in Figure 4.4a). The observed crosshatch pattern on the sample surface suggested the preserved planar structure of the GeSn layer after the annealing that also agreed with the observation of the GeSn peak with nominal Sn content on the RSM in Figure 4.2b and on the $\omega/2\theta$ spectrum in Figure 4.1c. Moreover, the thermal annealing resulted in only a slight increase of the RMS roughness up to 1.4 nm, which was attributed to the appearance of elevated circular spots on the surface. The density of the spots was ~$10^8$ $cm^{-2}$, which is the typical density of threading dislocations (TDs) for mismatched epitaxial layers [60].

Figure 4.5c shows the AFM image measured within the on-spot area (the bright region in Figure 4.4a) for sample A3 annealed for four hours. For this region, the surface is characterized by large droplet-like features located near the holes of comparable sizes. Moreover, a large distribution in size among the holes was also observed, which was presumably due to the coalescence of closely located smaller holes. It was concluded that the density of holes and circular spots on the AFM images in Figure 4.5c and Figure 4.5b, respectively, are in close agreement. Accordingly, the onset of droplet formation upon the annealing was correlated with the coalescence of circular spots (likely TDs), which in turn depends on their local density.

The elemental composition near the surface region of all samples was studied at the microscale using Raman spectroscopy. The small diameter of the laser spot of 1 μm and the shallow penetration depth of less than 50 nm is in contrast with XRD measurements, which provide statical averaged information over the large sample volume. For instance, the Raman spectra for the as-grown samples A1, A2, A3, and A4 are shown in Figure 4.6, where the most intensive peaks are seen near the vertical dashed line that corresponds to Ge-Ge frequency for bulk Ge at 301 $cm^{-1}$ [85]. These peaks were attributed to the Ge-Ge mode in the GeSn since

their intensity is strongly related to the Sn content in the $Ge_{1-x}Sn_x$ layer. This can be seen by comparing the Ge-Ge modes on the Raman spectra of all samples. Accordingly, the Ge-Ge peaks for samples A1 and A4 have the highest and lowest intensities, respectively, which agreed with the Sn content of 7.8 at. % and 12.2 at. % in the subsurface regions of the GeSn layers of sample A1 and A4, respectively. Moreover, the increase of Sn composition is also accompanied by a shift of the Ge-Ge mode toward the lower frequencies. The peak at ~280 $cm^{-1}$ was assigned in Ref. [86] to disorder-activated (DA) Ge-acoustic phonons, and the peak at ~260 $cm^{-1}$ corresponds to the G-Sn mode.

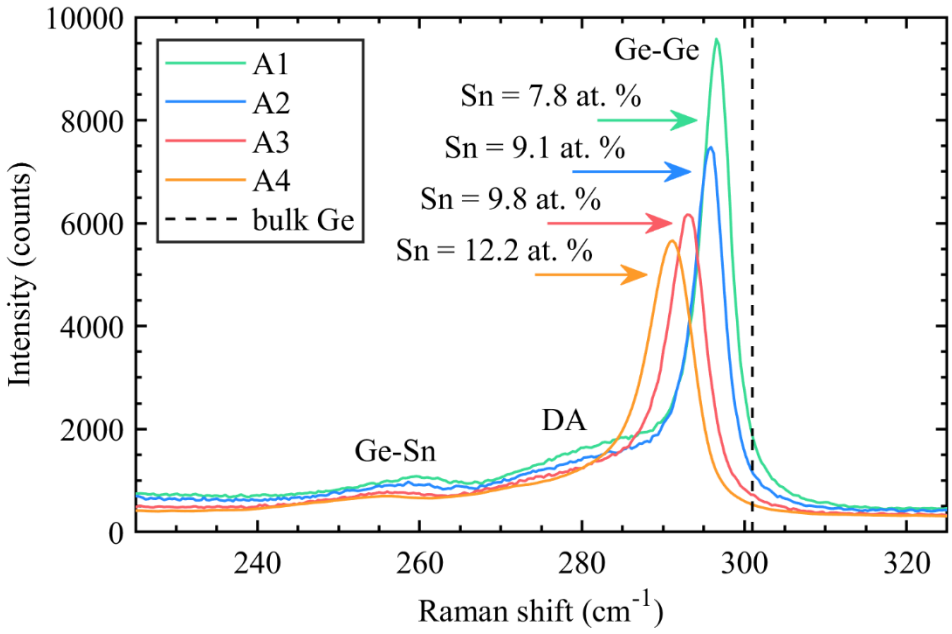


Figure 4.6. Measured Raman spectra for the as-grown samples A1, A2, A3, and A4. The dashed line marks the reference frequency of the Ge-Ge mode for Ge.

The Raman spectra measured before and after annealing are compared in Figure 4.7. For samples A1, A2, and A3, the Ge-Ge mode is slightly shifted towards the lower frequencies after the annealing, as expected for compressive strain relaxation. At the same time, for sample A3 annealed for four hours, the Ge-Ge mode on the Raman spectrum measured within the

segregation spot (Figure 4.4a) is seen at larger frequencies close to the position of bulk Ge. A similar shift is also observed for sample A4 after each annealing treatment. Apparently, this signified the severe loss of Sn from the GeSn layer. In fact, the decrease of Sn content is in agreement with the increase of the peak intensity corresponding to the Ge-Ge mode as well as with the XRD data in Figure 4.2.

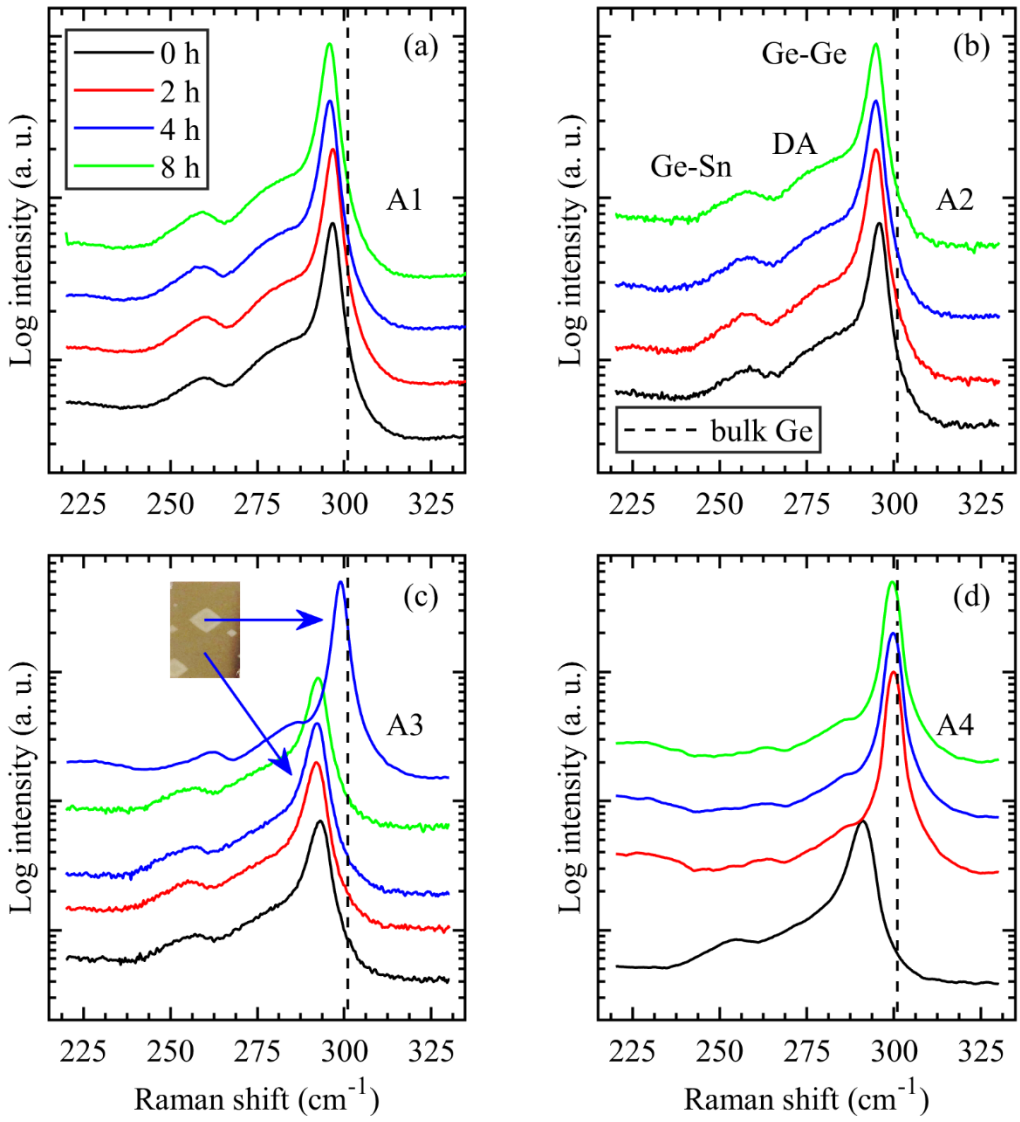


Figure 4.7. Raman spectra measured for samples A1 (a), A2 (b), A3 (c), and A4 (d) before (0 h) and after annealing (2 h, 4 h, and 8 h). The dashed line marks the reference frequency of the Ge-Ge mode for Ge. The inset in (c) shows the optical micrograph of the surface for sample A4 annealed for four hours.

For all samples, the position of the Ge-Ge mode was resolved from a fit of the Raman spectra with the following expression [85], [87],

$$I(\omega) = I_0(\omega) + I_{EMG}^{Ge-Ge}(\omega) + I_{EMG}^{DA}(\omega) + I_{EMG}^{Ge-Sn}(\omega) \quad \text{(Equation 4.1)}$$

where $\omega$ is the Raman frequency, $I_0(\omega)$ is the background intensity, and $I_{EMG}(\omega)$ are exponentially modified gaussian functions corresponding to the Ge-Ge, DA, and Ge-Sn modes. The $I_0(\omega)$ and $I_{EMG}(\omega)$ are given by the following expressions,

$$I_0(\omega) = b_1 + b_2\omega^{-m} \quad \text{(Equation 4.2)}$$

and

$$I_{EMG}(\omega) = \frac{A}{2t}\exp\left(\frac{1}{2}\left[\frac{W}{t}\right]^2 + \frac{\omega-\omega_c}{t}\right)\left(\text{erf}\left[-\frac{\omega-\omega_c}{\sqrt{2}W} - \frac{W}{\sqrt{2}t}\right] + 1\right) \quad \text{(Equation 4.3)}$$

where $A$ is the peak area, $t$ is the peak asymmetry, $W$ is the peak width, and $\omega_c$ is the central frequency. For example, the fitted Raman spectra are shown in Figure 4.8 for the as-grown sample A1.

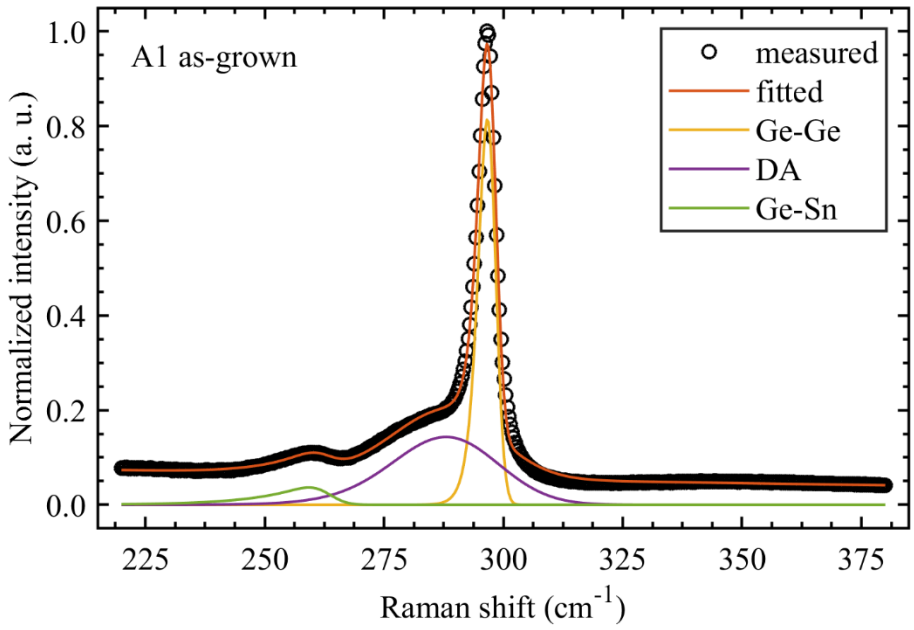


Figure 4.8. Measured (black symbols) and fitted (orange line) Raman spectrum for the as-grown sample A1.

The behavior of the Ge-Ge peak position is plotted in Figure 4.9 versus the strain determined from XRD RSMs. For samples A1 and A2, the Ge-Ge mode decreases towards the lower wavenumbers with the decrease of compressive strain during the thermal annealing. These experimental data points were compared with the following two-dimensional linear regression (dashed line in Figure 4.9),

$$\omega = \omega_0 + ax + b\varepsilon_{\parallel} \qquad \text{(Equation 4.4)}$$

where $\omega_0$ = 304 ± 0.9 cm$^{-1}$ is the Raman frequency for bulk Ge, $a$ = -84 ± 8 cm$^{-1}$ is the composition shift coefficient, and $b$ = -491 ± 52 cm$^{-1}$ is the strain shift coefficient [87]. In Figure 4.9, the experimental data for samples A1 and A2 are well aligned with the calculated dependencies for $x$ = 0.08 and $x$ = 0.09, respectively, which confirmed the Sn composition determined from the RSMs.

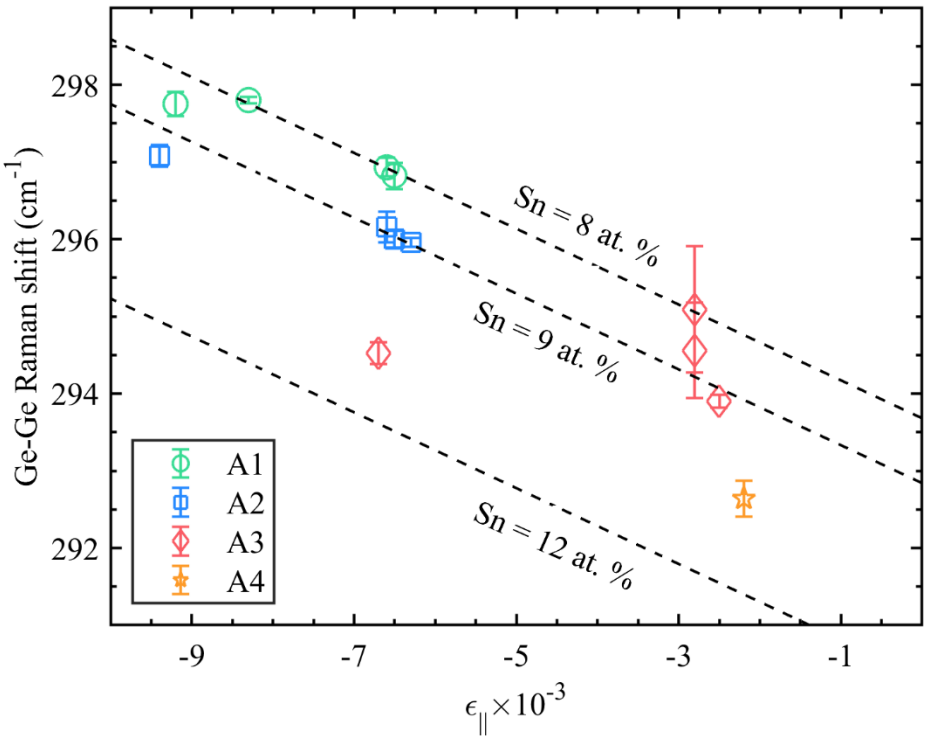


Figure 4.9. The Raman shift for the Ge-Ge mode versus compressive strain. The symbols and the dashed lines represent the measurement and calculations, respectively [82].

A lower degree of correlation between the Sn content determined from XRD and Raman measurements is seen in Figure 4.9 for samples A3 and A4. For sample A3, this discrepancy was attributed to the presence of the graded composition GeSn GL near the surface, which contributes to the Raman signal. At the same time, the compositional gradient in the GeSn layer resulted in a relatively low intensity and not well-defined peak on the RSM. Moreover, the Ge-Ge peak on the Raman spectrum is perturbed by the closely located DA peak. Accordingly, since the intensity of the Ge-Ge peak decreases as the Sn composition increases, the DA peak has a stronger effect on the shape of the Ge-Ge peak.

The chemical characterization of sample A3 after annealing for four hours was additionally carried out using SEM and EDX measurements. Figure 4.10a shows the SEM image measured within the region that was not affected by the segregation spot. Apparently, after annealing for four hours there were no noticeable changes in the surface morphology, which also agrees with the observations on the AFM images in Figure 4.5b. In addition, a uniform distribution of Sn and Ge for this region can be observed on the EDX maps in Figure 4.10b and 4.10c, respectively, while the Sn composition in the GeSn layer, which is close to the nominal value of ~9.8 at. % was confirmed by XRD and Raman measurements. In contrast, the SEM image of the area that corresponds to the segregation spot (Figure 4.10d) is characterized by droplet-like features with a density on the order of $10^7$ $cm^{-1}$. According to the EDX maps in Figure 4.10e, these were attributed to Sn precipitates. Simultaneously, the low Ge content within the droplets is seen on the EDX map in Figure 4.10f. Moreover, the varying droplet volume indicates their surface migration and coalescence. It was concluded that the area in between the droplets corresponded to a GeSn layer with the Sn composition less than 1 at. %, which corresponded to an equilibrium Sn content in a GeSn alloy. Moreover, this also explained the

emergence of the low Sn content peak on the XRD RSMs as well as the shift of the Ge-Ge peak on Raman spectra toward higher frequencies. According to the XRD, AFM, Raman, and SEM-EDX measurements, it was concluded that the segregation of Sn, the compressive strain relaxation, and the density of defects are closely related.

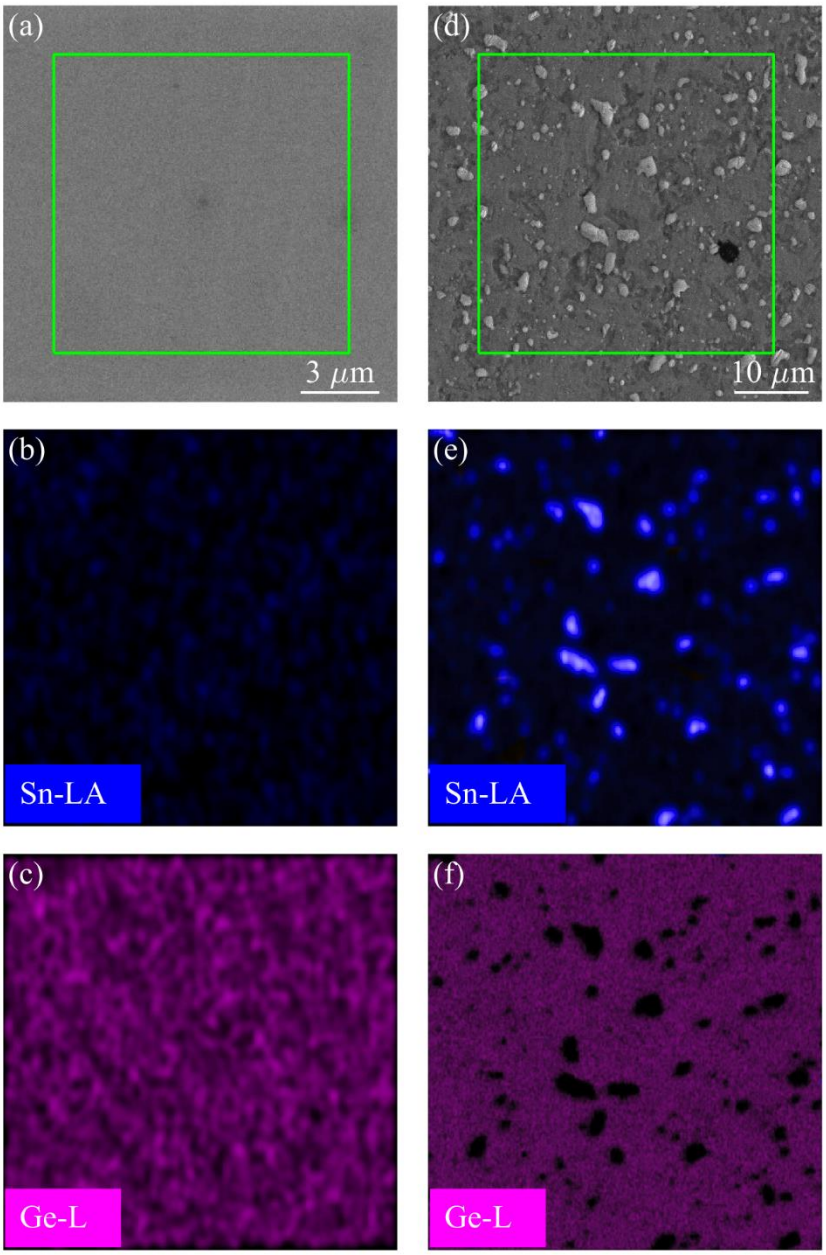


Figure 4.10. The SEM and EDX images measured for the on-spot (a) – (c) and off-spot (d) – (f) areas of sample A3 annealed for four hours [82].

The magnitude of strain and the density of misfit dislocations were estimated from RSM simulations (Figure 4.11), and are shown in Figures 4.12 and 4.13 only for the GeSn BL of each sample. The rationality for showing the data for the BL is related to the shifts of the GeSn peaks on the RSMs in Figure. 4.2c and 4.2d with respect to Ge peak. As can be seen, the BL peak is the most shifted toward the relaxation line, which indicated that most of the strain relieving MDs were located at the interface between the BL and the Ge buffer. At the same time, the $Q_{\parallel}$ shifts between the BL and GL as well as between the GL and TL peaks on the RSMs are hardly noticeable, which signified a low density of MDs for these regions of the GeSn layer. In other words, the lateral lattice parameter $a_{\parallel}$ in the GL and TL regions was nearly equal to that in the BL before and after the annealing. Accordingly, the strain relaxation in the GL layer of sample A3 before and after annealing was proportional to the strain relief in the BL region.

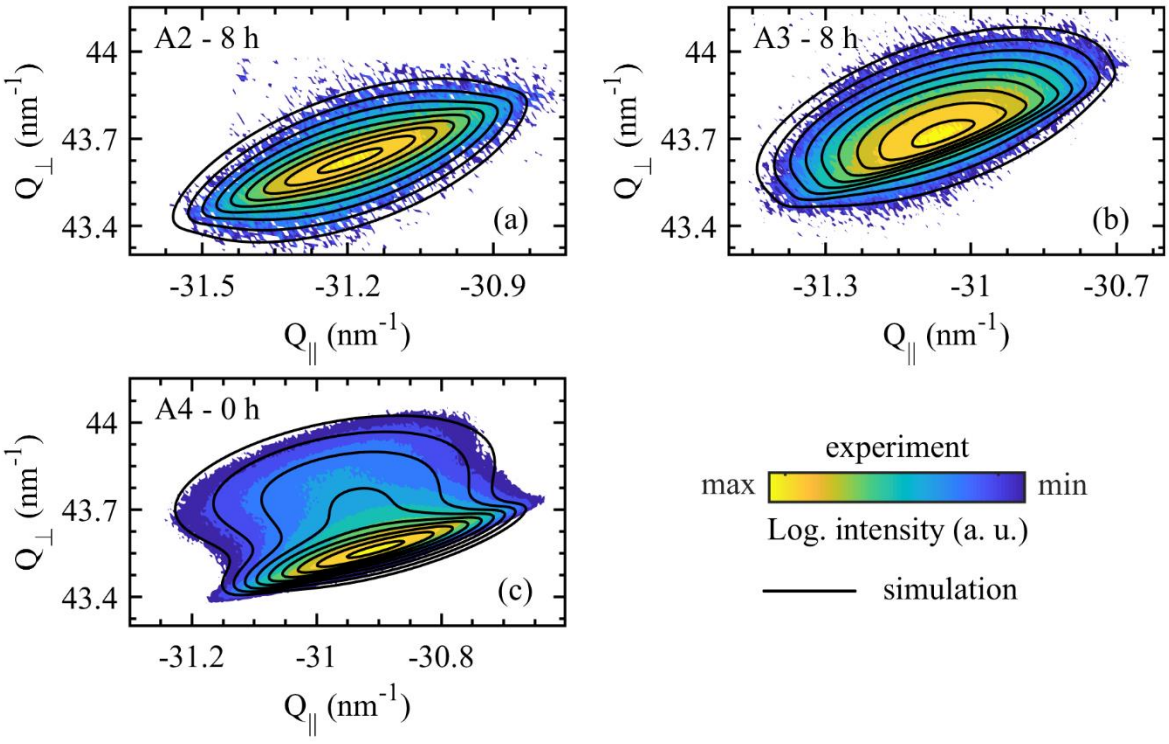


Figure 4.11. Experimental (color) and calculated (line) $\bar{2}\bar{2}4$ RSMs for samples A2 (a), A3 (b), and A4 (c).

Figure 4.12 shows that for samples A1 and A2, the compressive strain in the BL regions of the GeSn layer was -9.5 × $10^{-3}$ before annealing. This also relates to a degree of strain relief of 5.4 and 19.5%, respectively. The magnitude of strain decreased with increasing GeSn layer thickness for samples A3 and A4 down to -6.3 × $10^{-3}$ and -1.1 × $10^{-3}$, and the degree of strain relaxation increased to 44.1 and 91.0%, respectively.

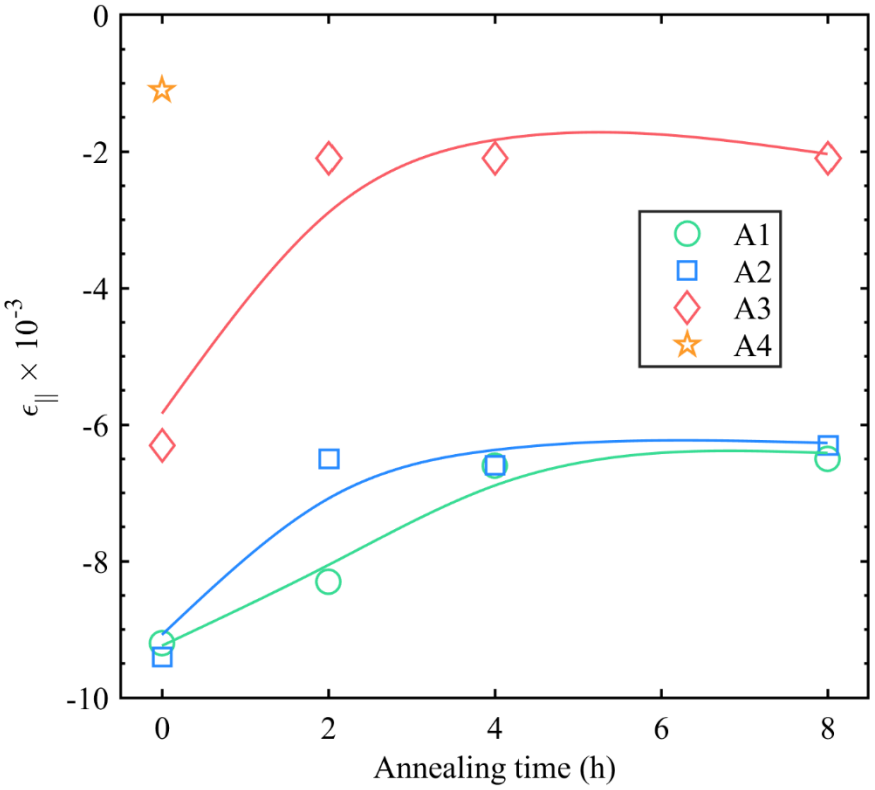


Figure 4.12. The compressive strain in the bottom region of GeSn layer for samples A1, A2, A3, and A4 versus the annealing time [82].

Figure 4.13 shows that the GeSn BL regions have a density of dislocations that increased proportionally with the degree of strain relaxation. The density of dislocations was lower for sample A1 due to the smaller lattice mismatch between the BL and the Ge buffer. The BL of the as-grown sample A4 had the largest density of MDs at 4.1 × $10^{5}$ $cm^{-1}$, which was considered as the limiting value for a GeSn layer with the Sn molar fraction of 9 at. %. It also should be

emphasized that, while the line length of a threading dislocation is limited by the layer thickness, a misfit segment usually extends in the plane of the interface over several microns. Therefore, the effect of the strain field related with MDs on the diffuse X-ray scattering prevails over that arising from TDs, which practically prevents determination of the density of TDs from the RSM. However, for an idealized situation, each MD can be characterized by two threading arms that run toward the sample surface.

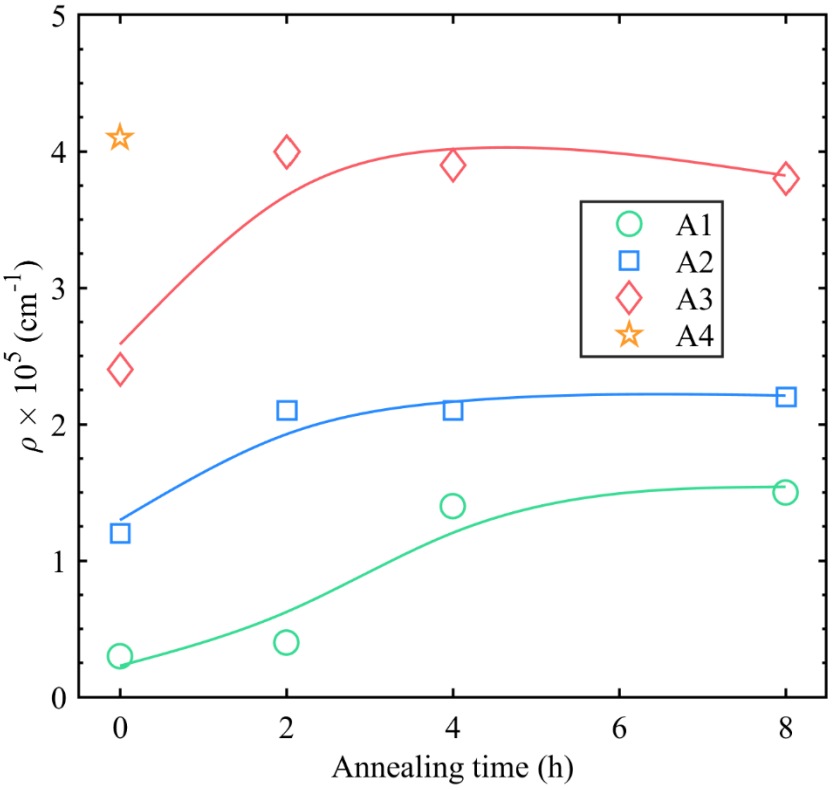


Figure 4.13. The density of misfit dislocations measured in the bottom region of GeSn layer for samples A1, A2, A3, and A4 versus the annealing time [82].

The magnitude of compressive strain in the GeSn layers decreased by about a factor of two after annealing for two hours samples A2 and A3, and after annealing for four hours sample A1. Annealing for longer periods did not induce a significant change in the strain state. The density of MDs in the GeSn layers of the annealed samples increased in agreement with the

strain relaxation. According to these observations, it was concluded that the extent of strain relaxation under the post-growth annealing of the GeSn layer is determined by the density of dislocations in the as-grown samples. The strain for the GeSn layers of the annealed samples A4 is not shown in Figure 4.12 due to the strong Sn segregation and the deviation of Sn composition from the nominal value.

The saturation of strain relief in the GeSn layers of the annealed samples was explained by considering the fact that the residual strain in an epitaxial layer of thickness $h$ is governed by the balance between the energy associated with elastic strain, $E_\varepsilon \sim h\varepsilon_\parallel^2$, and the energy of a grid of strain relieving misfit dislocations [52]. In other words, the nucleation of new dislocations is energetically favorable if the strain energy increases. According to the expression for $E_\varepsilon$, the increase of $E_\varepsilon$ implies an increase of the layer thickness or the magnitude of compressive strain. Since the GeSn layer thickness does not change during the annealing, the relaxation results may be explained by an additional strain due to the thermal expansivity of GeSn, which was shown to increase as a function of Sn content [88]. Under these conditions, the movement of preexisting TDs from the Ge buffer and gliding of dislocation half-loops in the (111) plane of the GeSn layer toward the GeSn/Ge interface aid to form additional misfit segments [56].

Given the low compressive strain in the GeSn layers for samples A3 and A4, as well as the observed segregation of Sn for these samples, there was an apparent interplay between the strain relaxation and Sn outdiffusion. At the same time, this conclusion is counterintuitive if considering the previous results, where it was shown that the relaxation of compressive strain in a GeSn layer is accompanied by an enhanced Sn incorporation. Moreover, the presence of regions with nominal Sn content alongside those with Sn composition of 1 at. % for sample A3 annealed at 300 °C is in contrast with gradual diffusion of Sn reported elsewhere for

temperatures not lower than 400 °C [77]–[79].

At the same time, the interaction of solute atoms with crystalline defects is present in many materials. For instance, an increased concentration of solute atoms at stacking faults was shown in Ref. [89] from the first-principles calculations as well as from an experimental analysis. It was shown that the segregation phenomenon can be attributed to a change of thermodynamic properties in the vicinity of a nanoscale defect. Moreover, in Ref. [90], it was theoretically shown that segregation of solute atoms effectively reduced the dislocation line energy. Also, the accumulation of Sn atoms at the dislocation sites in GeSn layers was recently revealed using atom probe tomography in Ref. [81], suggesting that the TDs may act as channels that facilitate the transport of Sn toward the surface.

Considering the interaction of solute atoms with the dislocations, it can be argued that the TD and MD sites are enriched with Sn at the stage of epitaxial layer deposition. Moreover, examination of the GeSn GL region in the previous chapter revealed an enhanced Sn incorporation with the onset of compressive strain relief at fixed growth conditions. In practice, the substitutional Sn atoms in the relaxed lattice of GeSn have a lower strain energy, which results in their reduced segregation toward the surface during the growth. According to these observations, it can be assumed that the incorporation of Sn is even more enhanced near the dislocation core where the lattice expansion is the largest, and that corresponds to a lower strain energy of substitutional Sn atoms. Therefore, the MDs and TDs can be considered as region with enriched Sn composition, which start to form with the onset of compressive strain relaxation when the thickness of the GeSn layer is above the critical thickness. For example, a schematic illustration of a dislocation half-loop is shown in Figure 4.14, where the misfit and threading segments are shown with red and blue lines, respectively.

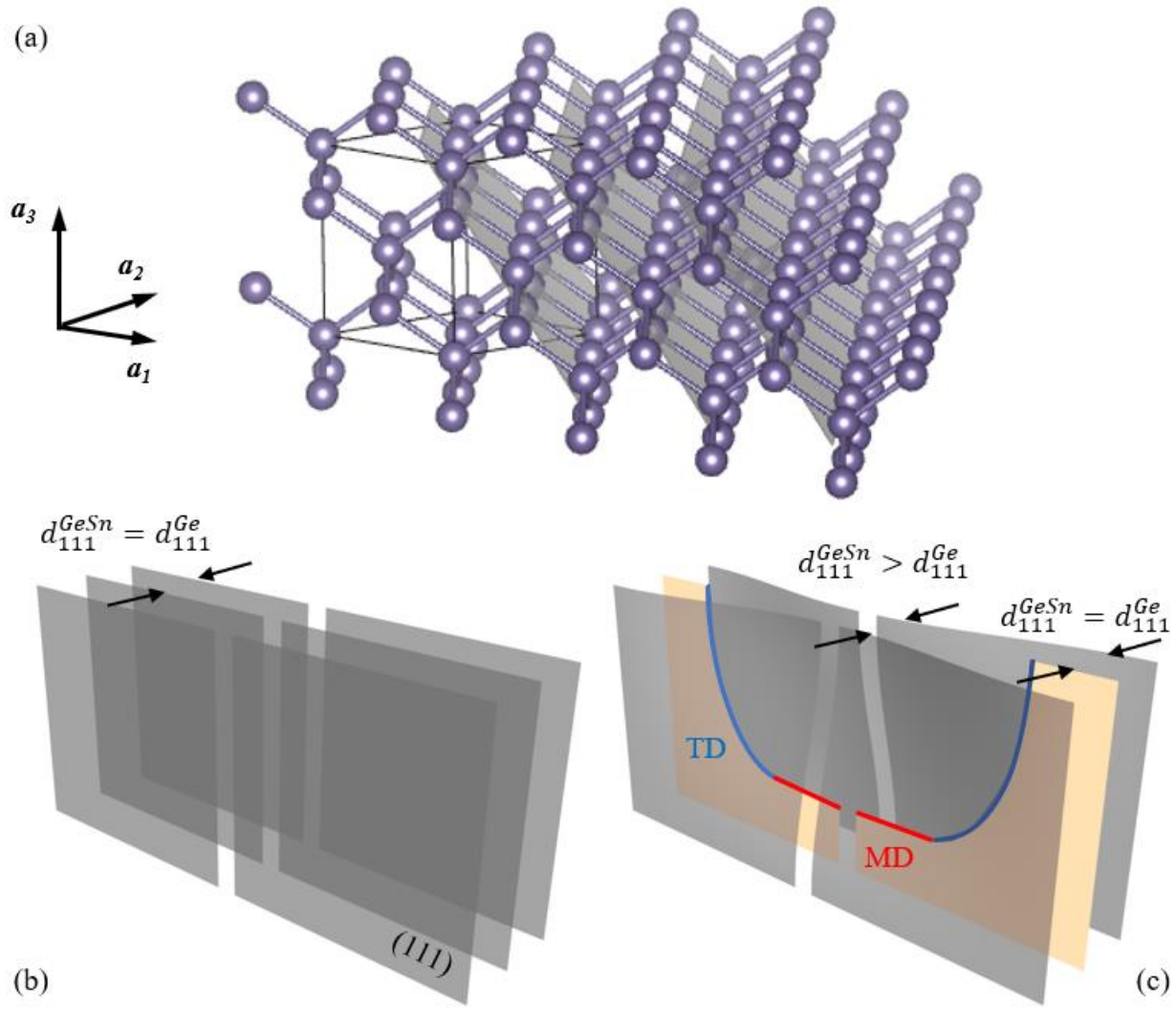


Figure 4.14. (a) Schematic illustration of the Ge lattice and the (111) crystal planes. (b) The comparison of the (111) planes in the absence and presence of a dislocation loop.

By following the discussion above, the higher density of MDs in the GeSn layers of the as-grown samples A3 and A4 was associated with a higher density of TDs penetrating through the GL layer. Moreover, as the density of dislocations increases, the average distance between the dislocations decreases, which leads to Sn gathering in regions located closer to each other. Therefore, diffusion of Sn atoms from these regions during the annealing at 300 °C can lead to Sn precipitation with a higher probability for strongly dislocated GeSn layers. Furthermore, the

melted Sn within the precipitates can assist further decomposition of the GeSn layer, as observed for sample A4 for which the density of MDs after the growth was ~$4 \times 10^5$ $cm^{-1}$. The appearance of segregation spots for sample A3, for which the density of MDs after the growth was ~$2 \times 10^5$ $cm^{-1}$, can be adequately attributed to an inhomogeneous distribution of dislocations within the epitaxial layer and their pile-up [91].

The preferential pathways for migration of Sn precipitates in the form of melted droplets can be qualitatively studied by considering the atomic arrangement of the diamond cubic crystal. Due to the different atomic configurations within the different crystallographic planes, the density of bonds per surface area that must be broken for the droplet migration also varies for different crystallographic directions. In practice, the density of bonds per surface area can be associated with an energy barrier for droplet propagation.

Figure 4.15 shows the bond configuration for the (001) crystallographic plane, in which each lattice point (red sphere) is covalently bonded with two nearest neighbors underneath (blue spheres). The bonds that must be broken to form a new surface are shown with red color. The right-hand side of Figure 4.15 emphasizes the arrangement of the lattice points within the (001) plane. As can be seen, the (001) plane contains only two atoms, since the four atoms at the corners of the plane are shared by four neighboring planes and the atom at the center completely belongs to the (001) plane. For each atom in the (001) plane, two bonds must be broken to form a new surface. Therefore, for the (001) plane, the density of broken bonds per unit area can be given by the following expression,

$$n_{(001)} = \frac{N_{(001)}^{atoms} \times N_{(001)}^{bonds}}{S_{(001)}} = \frac{4}{a^2} \qquad \text{(Equation 4.5)}$$

where $N_{(001)}^{atoms} = 2$ is the number of atoms in the (001) plane, $N_{(001)}^{bonds} = 2$ is the number of bonds per atom, $S_{(001)} = a^2$ is the surface area of the (001) plane, and $a$ is the lattice parameter.

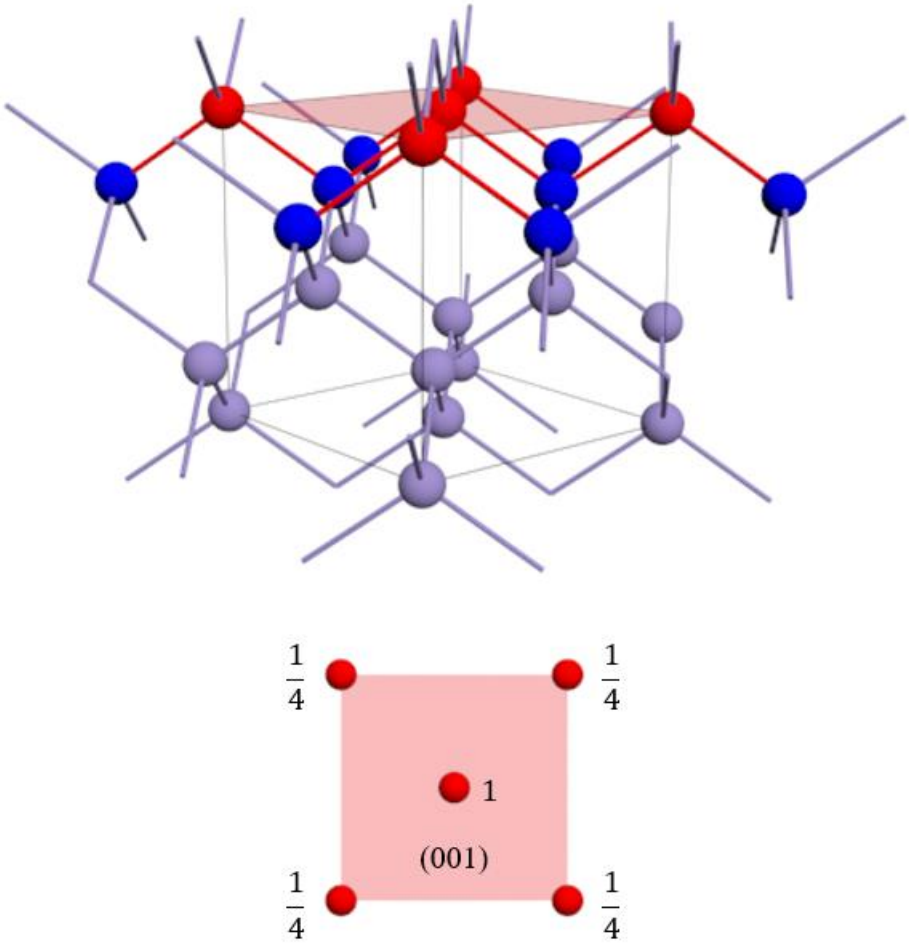


Figure 4.15. The unit cell of a diamond cubic crystal and its (001) plane. Fractions indicate the portions of the lattice points shared by the (001) plane.

The (110) plane in Figure 4.16 contains four atoms, each of which is single-bonded with an atom in the nearest plane. Therefore, for the (110) plane, $N_{(110)}^{atoms} = 4$, $N_{(110)}^{bonds} = 1$, and $S_{(110)} = \sqrt{2}a^2$, which according to Equation 4.5 gives a bond density $n_{(110)} = \sqrt{8}/a^2 \approx 2.8/a^2$. Ultimately, Figure 4.17 shows the (111) plane of the diamond cubic crystal, which has the highest density of lattice points. However, only three atoms of the (111) plane form single bonds with the nearest plane, so that $N_{(111)}^{atoms} = 3$, $N_{(111)}^{bonds} = 1$, and $S_{(111)} = \left(\sqrt{3}/2\right)a^2$, which results in a bond density $n_{(111)} = 2\sqrt{3}/a^2 \approx 3.5/a^2$.

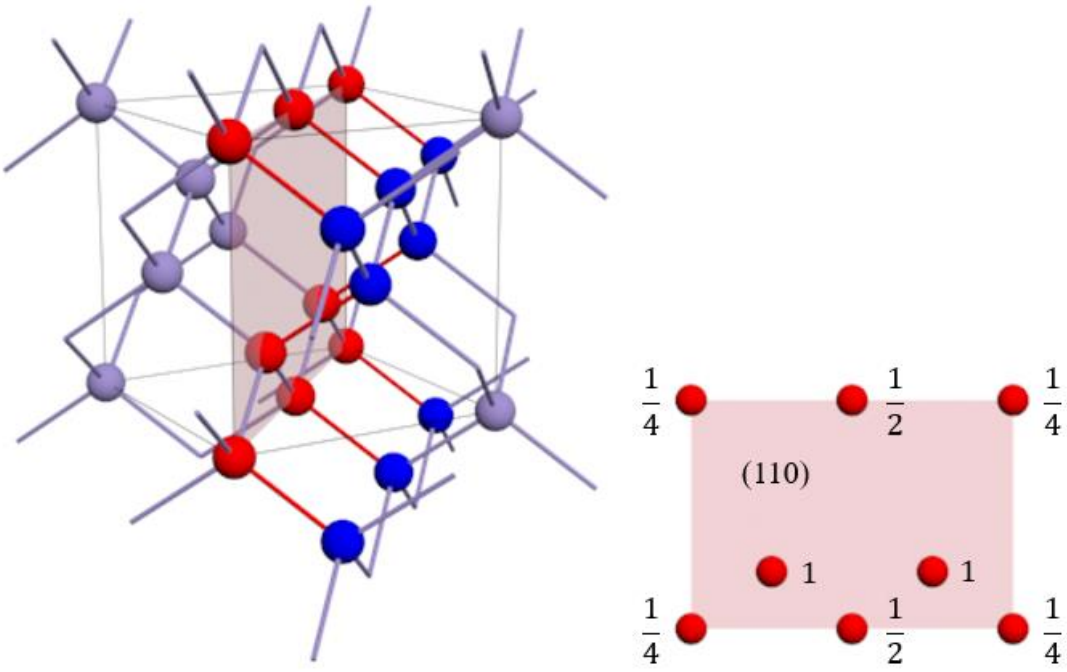


Figure 4.16. The unit cell of a diamond cubic crystal and its (110) plane. Fractions indicate the portions of the lattice points shared by the (110) plane.

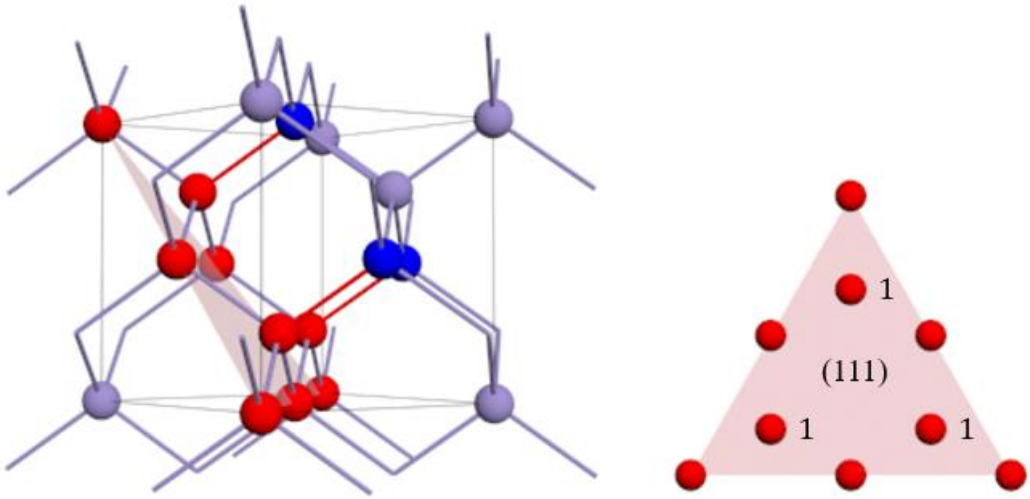


Figure 4.17. The unit cell of a diamond cubic crystal and its (111) plane. Fractions indicate the portions of the lattice points shared by the (111) plane.

It was concluded that for a diamond cubic crystal the binding energy is the highest across the [001] direction. Therefore, the propagation of the melted droplet should be more easy along

the [111] direction and particularly along the [110]. Indeed, migration of droplet precipitates is often observed on the surface of GeSn layers, where their trails are predominantly oriented along the <110> directions [30]. At the same time, their propagation along [111] can explain the droplet migration from the BL region of the GeSn layer toward the surface.

## 4.4 The effect of annealing treatment on photoluminescence of compressively strained GeSn layers

The low density of defects and the high Sn content in GeSn layers are key parameters for efficient optoelectronic devices. At the same time, the large lattice mismatch of about 15% between α-Sn and Ge implies an increase of compressive strain with increasing Sn composition in GeSn layers grown on Ge substrates. The compressive strain is released by MDs, which form above the critical layer thickness for strain relaxation. An enhancement of photoluminescence properties can be foreseen with the compressive strain relaxation, as this approaches the direct conduction Γ valley closer to the indirect conduction L valley. Practically, this limits carrier thermalization from the Γ valley into the indirect conduction L valley, which must enhance the recombination intensity [92].

The MDs formation is accompanied by an increase in the density of TDs, which propagate through the epitaxial layer toward the surface. Both MDs and TDs are sources of non-radiative processes that are detrimental to the emission properties. Therefore, for compressively strained GeSn layers with the Sn composition near the indirect-to-direct bandgap transition, the photoluminescence efficiency is a tradeoff between the compressive strain relief and the densities of structural defects. Besides, the GeSn layers with high Sn composition are metastable alloys, and annealing at temperatures above the eutectic point (231.1 °C) may have a severe

impact on their optical properties.

The photoluminescence characterization study was conducted to describe the effect of thermal treatment on the emissive performance of GeSn/Ge heterostructures. The PL measurements were performed at 10 K using a pulsed laser with 1064 nm wavelength for samples A1 and A2, and a continuous wave (CW) laser with 532 nm wavelength for sample A3 to reduce the light penetration depth. The penetration depth was estimated by considering that the absorption coefficient (α) of a GeSn alloy is close to that of bulk Ge. Accordingly, the absorption coefficients for 532 and 1064 nm light are taken as $6.7 \times 10^5$ $cm^{-1}$ and $1.9 \times 10^3$ $cm^{-1}$, respectively [93]. Hence, the intensity of 532 and 1064 nm light drops to 36% at about 15 nm and 5 μm below the sample surface, respectively. Therefore, the PL spectra for sample A3 are representative of only the subsurface GL region of the GeSn layer, while the different Sn composition BL region does not contribute to the PL emission. Sample A4 was not considered for PL investigation due to the strong Sn outdiffusion from the GeSn layer after the annealing procedure.

The PL spectra for samples A1, A2, and A3 before and after annealing are shown in Figure 4.18. For samples A1 (Figure. 4.18b) and A3 (Figure 4.18c), the photoluminescence was dominated by a low-energy peak $L^{HH}$, which for an indirect bandgap GeSn alloy corresponds to the recombination of conduction band electrons at the L point with the valence band heavy holes (HH) [94]. It is well known that the compressive strain in the GeSn layers splits the degeneracy of the valence bands so that the heavy hole (HH) band with the larger density of states is above the light hole (LH) band [95]. For samples A1 and A3, the $L^{HH}$ peaks are seen at 0.63 and 0.56 eV, respectively. For sample A3, the lower bandgap energy (energy position of the $L^{HH}$ peak) seemingly corresponds to the higher Sn content and lower compressive strain in the GL region of

the GeSn layer (Figure 4.12).

The $\Gamma^{HH}$ peak at higher energies on the PL spectra of samples A1 and A3 was attributed to the recombination of conduction band electrons at the Γ point with the valence band heavy holes. The $\Gamma^{HH}$ peak is not seen for sample A2 due to the low integral PL for this sample so that the $\Gamma^{HH}$ peak height must be comparable with the background intensity. It should be noted that the PL signal for sample A3 was acquired by focusing the laser spot on the surface area that was not affected by the segregation spots.

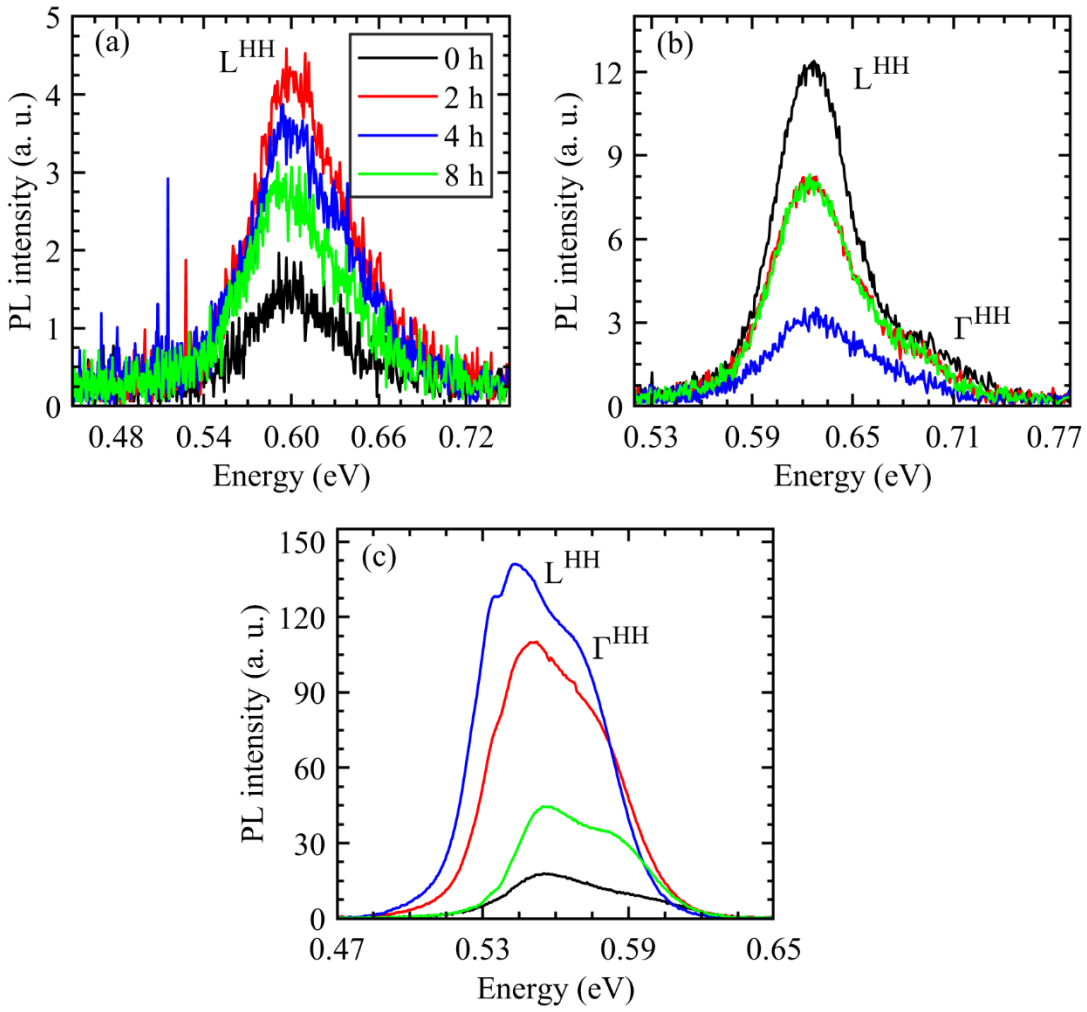


Figure 4.18. The PL spectra from the GeSn layers of samples A2 (a), A1 (b), and A3 (c) measured at 10 K before and after annealing.

For all samples, the evolution of PL intensity with time is compared in Figure 4.19, where the integral PL was calculated as the area under the peak. In particular, the PL from the GeSn layer of sample A1 has a stronger PL emission before the annealing treatment and a decrease of the PL intensity with the increasing annealing time. In contrast, a slight increase of the integral PL with increasing annealing time is seen for sample A2, and a remarkable enhancement of PL emission is observed for sample A3. The dissimilar behavior of PL emission for samples A1, A2, and A3 was attributed to an increase of bandgap directness (decreasing energy separation $\Delta E$ between the $L^{HH}$ and $\Gamma^{HH}$ peaks), as dictated by the Sn content and compressive strain relaxation in the GeSn layers.

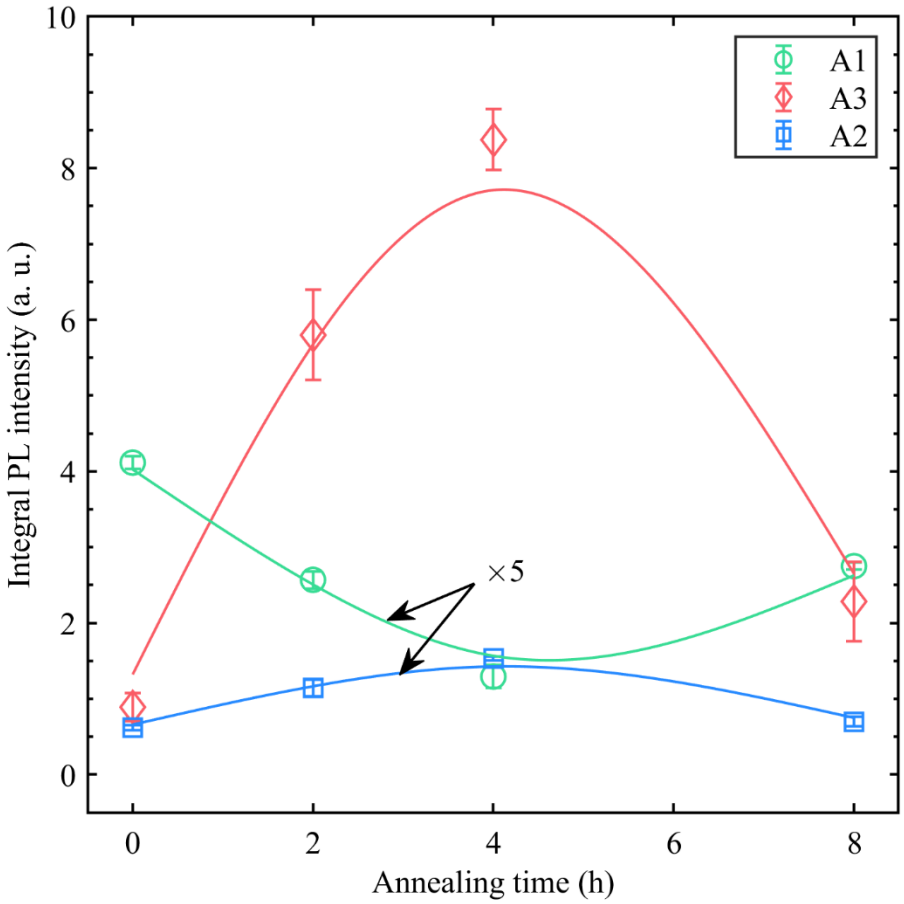


Figure 4.19. The evolution of integral PL intensity of samples A1, A2, and A3 as a function of annealing time.

The magnitude of peak separation, ΔE, was determined for samples A1 and A3 after each annealing cycle by fitting the PL spectra with two Gaussian functions. For example, the deconvoluted PL spectra into Gaussian components are shown in Figure 4.20 for the as-grown samples A1 and A3.

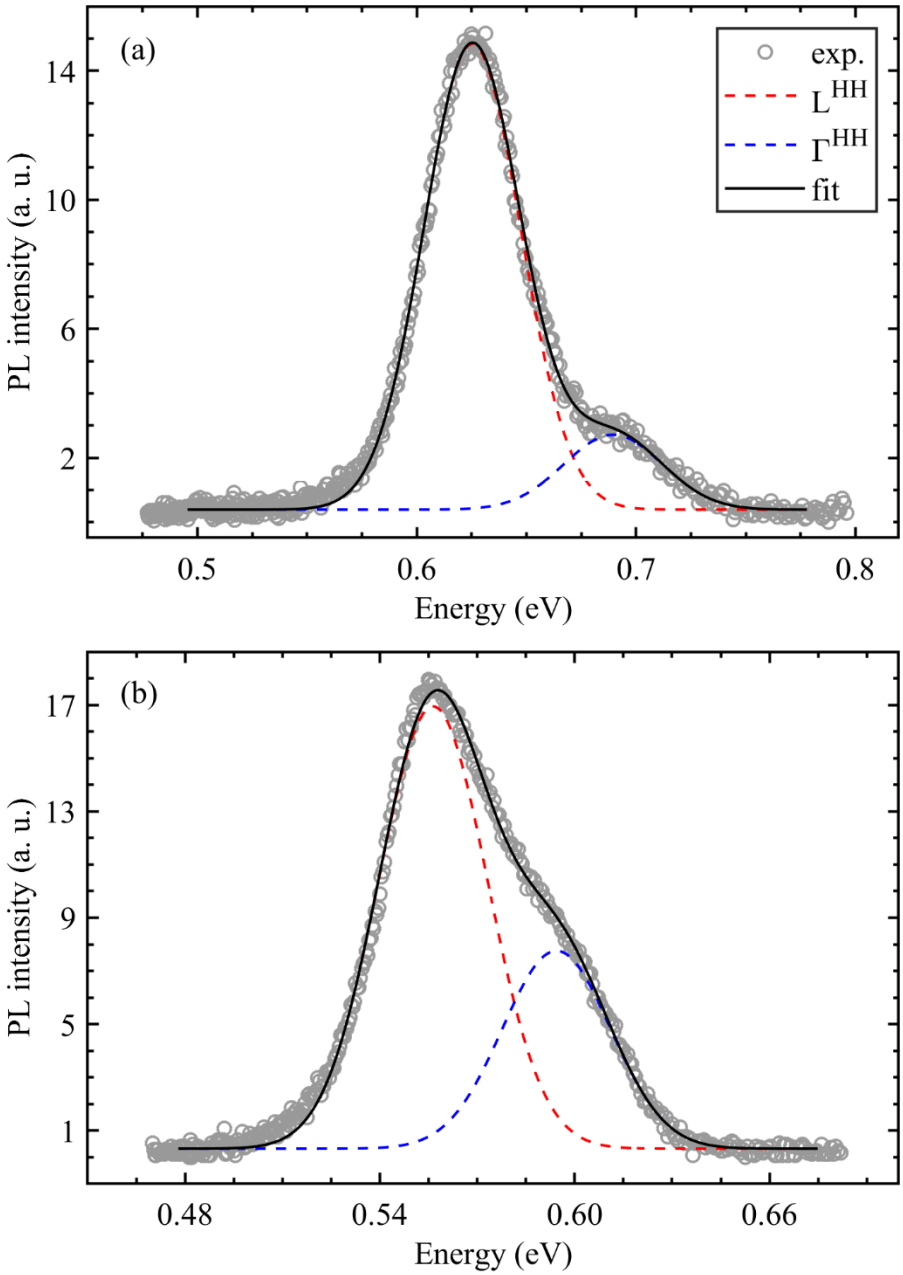


Figure 4.20. The measured (symbol) and fitted (line) PL spectra from the GeSn layers of as-grown samples A1 (a) and A3 (b).

Figure 4.21 shows the evolution of energy separation between the $L^{HH}$ and $\Gamma^{HH}$ peaks on the PL spectra of samples A1 and A3 as a function of annealing time. As can be seen, the magnitude of ΔE is larger for sample A1, which indicates a more indirect bandgap GeSn layer for this sample. The larger ΔE for sample A1 corresponds to the relatively low Sn composition of 7.8 at. % and the larger compressive strain (Figure 4.12) in the GeSn BL of this sample as compared with the GeSn GL of sample A3. The magnitude of ΔE decreased after four and two hours of annealing for sample A1 and A3, respectively, while annealing for longer periods did not induce a significant change of ΔE, which is similar to the relaxation of compressive strain in Figure 4.12.

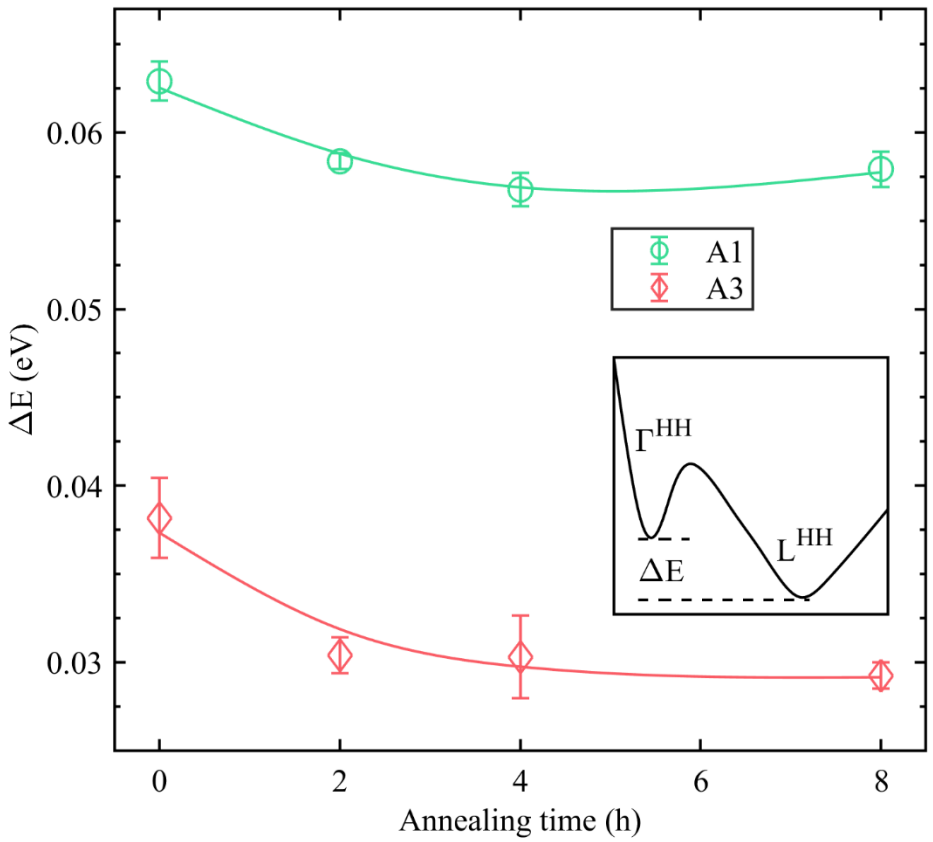


Figure 4.21. The energy separation between the conduction band minima at Γ and L points as a function of annealing time. Inset shows the schematic illustration of the energy band diagram for an indirect bandgap GeSn semiconductor.

This decrease of ΔE additionally indicated that the previously assigned $L^{HH}$ and $\Gamma^{HH}$ peaks on the measured PL spectra in Figure 4.18 indeed correspond to indirect and direct interband transitions, respectively, since the conduction band minimum at the Γ point decreases faster with the compressive strain relaxation than that at the L point [2].

According to Figure 4.21 and Figure 4.19, the magnitude of ΔE and the integral PL are strongly correlated. Therefore, considering the similar compressive strain in the GeSn layers of samples A1 and A2, as well as the higher Sn content in the GeSn layer of sample A2, one may expect even a smaller ΔE and, thus, a stronger PL signal for sample A2 in comparison with that of sample A1. However, the GeSn layer of sample A2 was of poorer optical quality due to the higher density of misfit dislocations, which could be the reason for the low integral PL for this sample (Figure 4.19).

On the other hand, the PL intensity for sample A3 was strongly enhanced despite the higher density of dislocations (~$2 \times 10^5$ $cm^{-1}$). Therefore, the overall PL from the GeSn layers can be understood as a net result related to the non-radiative processes due to defects and the radiative interband transitions. Moreover, an increased fraction of direct interband transitions with the decreasing energy separation, ΔE, can be seen in Figure 4.22a, which shows the ratio between the intensities of the $\Gamma^{HH}$ and $L^{HH}$ peaks on each PL spectrum. This additionally was considered to explain the stronger integral PL for sample A3.

Figure 4.22b shows a schematic model of indirect bandgap GeSn semiconductors with different energy separation, ΔE, between the L and Γ valleys of the conduction band. It shows that in the case of a larger ΔE, the photoexcited electrons are mostly thermalized in the L valley since the highest occupied electronic states in the L valley lie below the Γ valley minimum (Figure 4.22c). However, with the decreasing magnitude of ΔE, a larger fraction of photoexcited

electrons can occupy electronic states near the Γ minimum if the states in the L valley that are lower than the Γ valley are occupied (Figure 4.22b) [96]. Accordingly, the direct interband transitions with the decrease of bandgap energy were concluded responsible for the stronger PL of sample A3.

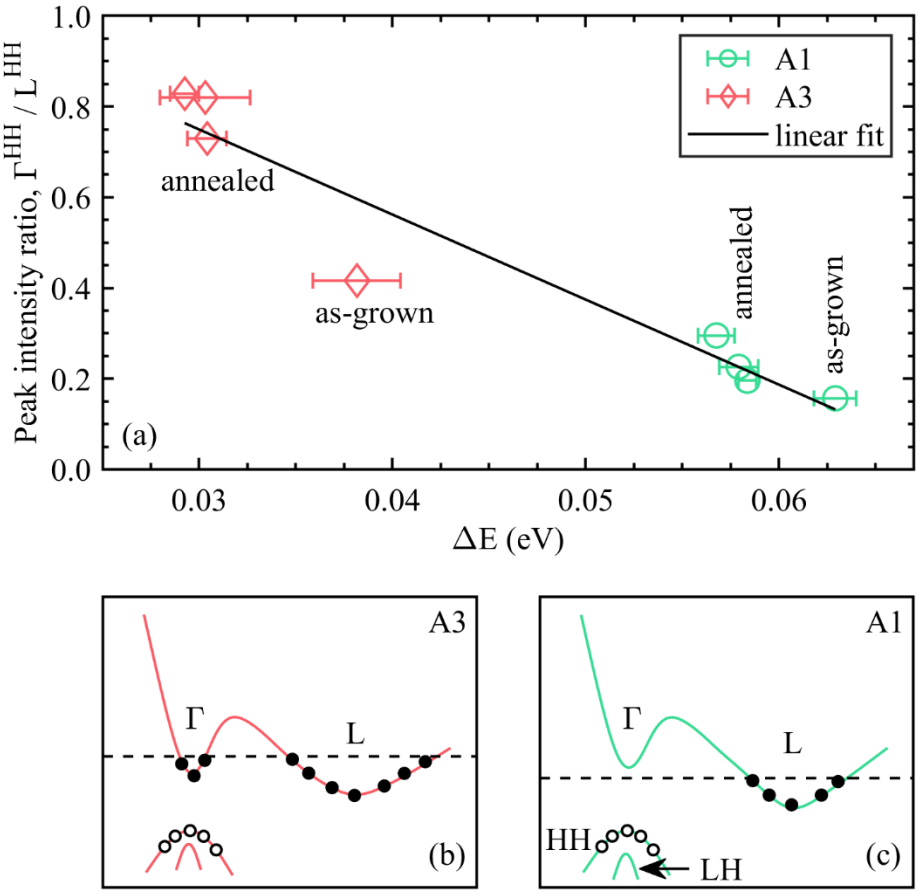


Figure 4.22. The intensity ratio between the $\Gamma^{HH}$ and $L^{HH}$ peaks as a function of energy separation ΔE (a) and the schematic band structure of samples A3 (b) and A1 (c). The dashed line shows the highest occupied electronic state in the L valley.

Figure 4.22b and 4.22c schematically show that the decrease of compressive strain brings the LH band closer to the HH band [95], which is similar to the decrease of ΔE in Figure 4.21. Thus, for an indirect bandgap GeSn layer, the splitting of the PL spectra into two peaks (Figure 4.18) can also be attributed to the energy difference between the L valley of the conduction band

and the valence HH and LH bands. Nonetheless, the occurrence of both L-HH and L-LH transitions cannot explain the strongly enhanced integral PL (Figure 4.19) after the annealing of sample A3.

## 4.5 Summary

In conclusion, the structural stability of the GeSn layers during temperature annealing at 300 °C was correlated with the density of misfit/threading dislocations. It was shown that the magnitude of compressive strain in the GeSn layers decreased by a factor of two after the annealing for four hours, with no effect on the strain state after more prolonged temperature treatment. The strain relaxation behavior was explained by the elongation of pre-existing MDs in the GeSn layers. Moreover, the density of pre-existing dislocations was correlated with the onset of Sn precipitation, which corresponded to a critical MD density of $\sim 2 \times 10^5$ $cm^{-1}$. According to these results, it was concluded that the thermal stability of GeSn layers can be improved by lowering the lattice mismatch between the epitaxial layer and the underlying substrate to reduce the density of dislocations.

A compromise between the increasing density of defects and the decreasing L-Γ energy separation (ΔE) during the annealing was shown to determine the emission properties of indirect bandgap GeSn layers. Particularly, a higher integral PL was shown for the GeSn layers with a smaller ΔE, for which the PL intensity was significantly enhanced after the annealing due to an increased fraction of direct interband transitions. In contrast, a decrease of PL intensity was observed after the annealing of the GeSn layers with a larger ΔE, for which the indirect interband transitions were dominating.

# Chapter 5: Conclusion and outlook

In this dissertation, the thermal stability, structural, and optical properties of the GeSn/Ge/Si(001) heterostructures were investigated by XRD, PL, AFM, EDX, SIMS, Raman spectroscopy, and x-ray diffraction simulations.

Simulations of x-ray diffuse scattering from the GeSn layers were exploited for rapid and accurate determination of the Sn composition, strain state, and density of misfit dislocations in each region of the GeSn layer. It was shown that the Sn incorporation during the growth of the GeSn layer is suppressed due to the built-in compressive strain. A spontaneous enhancement of Sn incorporation in the thick GeSn layers was attributed to the onset of compressive strain relaxation when the epitaxial layer thickness is above the critical thickness for strain relaxation. Accordingly, the GeSn layers that are grown on Ge substrates typically display three regions with distinct Sn composition that correspond to the transition from a fully strained to a completely strain relaxed layer. The Sn composition determined from XRD calculations was in good agreement with the experimental data obtained from SIMS measurements.

The thermal stability of the GeSn/Ge heterostructures was studied by annealing the samples under vacuum conditions at 300 °C for two, four, and eight hours. The thermal treatment of the GeSn layers revealed a close connection between the density of pre-existing dislocations in the GeSn layer and the Sn segregation during the annealing. It was shown that the Sn segregation in a dislocated GeSn layer occurs at lower temperatures than for a sample with relatively less defects, which led to a conclusion that the activation energy for Sn diffusion in the presence of dislocations is also lower. A critical density of misfit dislocations of about $2 \times 10^5$ $cm^{-1}$ was correlated with the onset of Sn segregation. It was suggested that the misfit/threading dislocations in the GeSn layers act as preferential sites for Sn gathering during

the layer growth. Accordingly, the increase of the density of dislocations was translated into a higher density of sites with elevated Sn content, which during the annealing facilitates the formation of melted Sn droplets. The melted Sn was held responsible for the GeSn layer decomposition.

The suggested strategies for improving the thermal stability of the GeSn layers imply a reduction of the densities of dislocations by the deposition of the GeSn layers on substrates with lower lattice mismatch such as on InGaAs. Alternatively, a high melting point Ge layer can be introduced during the growth of the GeSn layer to separate the GeSn regions with high and low densities of defects.

References


[1] L. Chrostowski and M. E. Hochberg, *Silicon photonics design*. Cambridge, United Kingdom: Cambridge University Press, 2015, pp. 5–16.

[2] M. J. Deen and P. Kumar Basu, *Silicon Photonics : Fundamentals and Devices*. New York, NY, USA: Wiley, 2012, pp. 1–11.

[3] L. Pavesi, "Will silicon be the photonic material of the third millenium?," *Journal of Physics Condensed Matter*, vol. 15, no. 26. IOP Publishing, pp. 1169–1196, Jul. 09, 2003, doi: 10.1088/0953-8984/15/26/201.

[4] J. D. Sau and M. L. Cohen, "Possibility of increased mobility in Ge-Sn alloy system," *Phys. Rev. B*, vol. 75, no. 4, p. 045208, Jan. 2007, doi: 10.1103/PhysRevB.75.045208.

[5] S. Wirths, Z. Ikonic, A. T. Tiedemann, B. Holländer, T. Stoica, G. Mussler, U. Breuer, J. M. Hartmann, A. Benedetti, S. Chiussi, D. Grützmacher, S. Mantl, and D. Buca, "Tensely strained GeSn alloys as optical gain media," *Appl. Phys. Lett.*, vol. 103, no. 19, p. 192110, Nov. 2013, doi: 10.1063/1.4829360.

[6] R. Geiger, T. Zabel, and H. Sigg, "Group IV direct band gap photonics: Methods, challenges, and opportunities," *Frontiers in Materials*, vol. 2. Frontiers Media S.A., pp. 1–18, Jun. 15, 2015, doi: 10.3389/fmats.2015.00052.

[7] G. Sun, "Intersubband approach to silicon based lasers—circumventing the indirect bandgap limitation," *Adv. Opt. Photonics*, vol. 3, no. 1, p. 53, Mar. 2011, doi: 10.1364/AOP.3.000053.

[8] P. Moontragoon, R. A. Soref, and Z. Ikonic, "The direct and indirect bandgaps of unstrained $Si_xGe_{1-x-y}Sn_y$ and their photonic device applications," *J. Appl. Phys.*, vol. 112, no. 7, p. 073106, Oct. 2012, doi: 10.1063/1.4757414.

[9] M. Fox, *Optical properties of solids*, Second edi. Oxford, [England]: Oxford University Press, Incorporated, 2010, pp. 62–84.

[10] S. Fukatsu, H. Sunamura, Y. Shiraki, and S. Komiyama, "Phononless radiative recombination of indirect excitons in a Si/Ge type-II quantum dot," *Appl. Phys. Lett.*, vol. 71, no. 2, pp. 258–260, Jul. 1997, doi: 10.1063/1.119514.

[11] M. De Kersauson, R. Jakomin, M. El Kurdi, G. Beaudoin, N. Zerounian, F. Aniel, S. Sauvage, I. Sagnes, and P. Boucaud, "Direct and indirect band gap room temperature electroluminescence of Ge diodes," *J. Appl. Phys.*, vol. 108, no. 2, p. 023105, Jul. 2010, doi: 10.1063/1.3462400.

[12] K. P. Homewood and M. A. Lourenço, "Optoelectronics: The rise of the GeSn laser," *Nature Photonics*, vol. 9, no. 2. Nature Publishing Group, pp. 78–79, Feb. 17, 2015, doi:

10.1038/nphoton.2015.1.

[13] G. Grzybowski, L. Jiang, J. Mathews, R. Roucka, C. Xu, R. T. Beeler, J. Kouvetakis, and J. Meńndez, "Photoluminescence from heavily doped GeSn:P materials grown on Si(100)," *Appl. Phys. Lett.*, vol. 99, no. 17, p. 171910, Oct. 2011, doi: 10.1063/1.3655679.

[14] C. G. Van De Walle, "Band lineups and deformation potentials in the model-solid theory," *Phys. Rev. B*, vol. 39, no. 3, pp. 1871–1883, Jan. 1989, doi: 10.1103/PhysRevB.39.1871.

[15] T. D. Eales, I. P. Marko, S. Schulz, E. O'Halloran, S. Ghetmiri, W. Du, Y. Zhou, S.-Q. Yu, J. Margetis, J. Tolle, E. P. O'Reilly, and S. J. Sweeney, "$Ge_{1-x}Sn_x$ alloys: Consequences of band mixing effects for the evolution of the band gap Γ-character with Sn concentration," *Sci. Rep.*, vol. 9, no. 1, p. 14077, Dec. 2019, doi: 10.1038/s41598-019-50349-z.

[16] X. Sun, J. Liu, L. C. Kimerling, and J. Michel, "Direct gap photoluminescence of n -type tensile-strained Ge-on-Si," *Appl. Phys. Lett.*, vol. 95, no. 1, p. 011911, Jul. 2009, doi: 10.1063/1.3170870.

[17] C. Boztug, J. R. Sánchez-Pérez, J. Yin, M. G. Lagally, and R. Paiella, "Mechanically flexible photonic-crystal cavities on strained-germanium nanomembranes," in *2014 Conference on Lasers and Electro-Optics (CLEO) - Laser Science to Photonic Applications*, Jun. 2014, pp. 1–2, doi: 10.1364/CLEO_SI.2014.STu2H.4.

[18] J. Mathews, R. Roucka, J. Xie, S.-Q. Yu, J. Menéndez, and J. Kouvetakis, "Extended performance GeSn/Si(100) p-i-n photodetectors for full spectral range telecommunication applications," *Appl. Phys. Lett.*, vol. 95, no. 13, p. 133506, Sep. 2009, doi: 10.1063/1.3238327.

[19] J. Michel, J. Liu, and L. C. Kimerling, "High-performance Ge-on-Si photodetectors," *Nat. Photonics*, vol. 4, no. 8, pp. 527–534, Aug. 2010, doi: 10.1038/nphoton.2010.157.

[20] D. Liang and J. E. Bowers, "Recent progress in lasers on silicon," *Nat. Photonics*, vol. 4, no. 8, pp. 511–517, 2010, doi: 10.1038/nphoton.2010.167.

[21] S. F. Fang, K. Adomi, S. Iyer, H. Morkoç, H. Zabel, C. Choi, and N. Otsuka, "Gallium arsenide and other compound semiconductors on silicon," *J. Appl. Phys.*, vol. 68, no. 7, pp. R31–R58, Oct. 1990, doi: 10.1063/1.346284.

[22] T. F. Kuech, L. J. Mawst, and A. S. Brown, "Mixed Semiconductor Alloys for Optical Devices," *Annu. Rev. Chem. Biomol. Eng.*, vol. 4, no. 1, pp. 187–209, Jun. 2013, doi: 10.1146/annurev-chembioeng-061312-103359.

[23] V. R. D'Costa, Y.-Y. Fang, J. Tolle, J. Kouvetakis, and J. Menéndez, "Ternary GeSiSn alloys: New opportunities for strain and band gap engineering using group-IV semiconductors," *Thin Solid Films*, vol. 518, no. 9, pp. 2531–2537, Feb. 2010, doi:

10.1016/j.tsf.2009.09.149.

[24] S. A. Ghetmiri, W. Du, J. Margetis, A. Mosleh, L. Cousar, B. R. Conley, L. Domulevicz, A. Nazzal, G. Sun, R. A. Soref, J. Tolle, B. Li, H. A. Naseem, and S.-Q. Yu, "Direct-bandgap GeSn grown on silicon with 2230 nm photoluminescence," *Appl. Phys. Lett.*, vol. 105, no. 15, p. 151109, Oct. 2014, doi: 10.1063/1.4898597.

[25] G. Sun, R. A. Soref, and H. H. Cheng, "Design of an electrically pumped SiGeSn/GeSn/SiGeSn double-heterostructure midinfrared laser," *J. Appl. Phys.*, vol. 108, no. 3, p. 033107, Aug. 2010, doi: 10.1063/1.3467766.

[26] P. R. Pukite, A. Harwit, and S. S. Iyer, "Molecular beam epitaxy of metastable, diamond structure $Sn_xGe_{1-x}$ alloys," *Appl. Phys. Lett.*, vol. 54, no. 21, pp. 2142–2144, 1989, doi: 10.1063/1.101152.

[27] E. Kasper, J. Werner, M. Oehme, S. Escoubas, N. Burle, and J. Schulze, "Growth of silicon based germanium tin alloys," in *Thin Solid Films*, Feb. 2012, vol. 520, no. 8, pp. 3195–3200, doi: 10.1016/j.tsf.2011.10.114.

[28] R. W. Olesinski and G. J. Abbaschian, "The Ge-Sn (Germanium-Tin) system," *Bull. Alloy Phase Diagrams*, vol. 5, no. 3, pp. 265–271, Jun. 1984, doi: 10.1007/BF02868550.

[29] S. Wirths, D. Buca, and S. Mantl, "Si-Ge-Sn alloys: From growth to applications," *Progress in Crystal Growth and Characterization of Materials*, vol. 62, no. 1. Elsevier Ltd, pp. 1–39, Mar. 01, 2016, doi: 10.1016/j.pcrysgrow.2015.11.001.

[30] H. Groiss, M. Glaser, M. Schatzl, M. Brehm, D. Gerthsen, D. Roth, P. Bauer, and F. Schäffler, "Free-running Sn precipitates: an efficient phase separation mechanism for metastable $Ge_{1-x}Sn_x$ epilayers," *Sci. Rep.*, vol. 7, no. 1, p. 16114, 2017, doi: 10.1038/s41598-017-16356-8.

[31] S. Takeuchi, A. Sakai, K. Yamamoto, O. Nakatsuka, M. Ogawa, and S. Zaima, "Growth and structure evaluation of strain-relaxed $Ge_{1-x}Sn_x$ buffer layers grown on various types of substrates," *Semicond. Sci. Technol.*, vol. 22, no. 1, p. S231, Jan. 2007, doi: 10.1088/0268-1242/22/1/S54.

[32] J. Tolle, A. V. G. Chizmeshya, Y. Y. Fang, J. Kouvetakis, V. R. D'Costa, C. W. Hu, J. Menéndez, and I. S. T. Tsong, "Low temperature chemical vapor deposition of Si-based compounds via $SiH_3SiH_2SiH_3$: Metastable SiSn/GeSn/Si(100) heteroepitaxial structures," *Appl. Phys. Lett.*, vol. 89, no. 23, p. 231924, 2006, doi: 10.1063/1.2403903.

[33] S. Assali, J. Nicolas, and O. Moutanabbir, "Enhanced Sn incorporation in GeSn epitaxial semiconductors via strain relaxation," *J. Appl. Phys.*, vol. 125, no. 2, p. 025304, Jan. 2019, doi: 10.1063/1.5050273.

[34] Y. G. Sadofyev, V. P. Martovitsky, A. V. Klekovkin, V. V. Saraikin, and I. S.

Vasil'Evskii, "Thermal stability of Ge/GeSn nanostructures grown by MBE on (001) Si/Ge virtual wafers," in *Physics Procedia*, 2015, vol. 72, pp. 411–418, doi: 10.1016/j.phpro.2015.09.078.

[35] O. Gurdal, P. Desjardins, J. R. A. Carlsson, N. Taylor, H. H. Radamson, J. E. Sundgren, and J. E. Greene, "Low-temperature growth and critical epitaxial thicknesses of fully strained metastable $Ge_{1-x}Sn_x$ ($x \lesssim 0.26$) alloys on Ge(001)2×1," *J. Appl. Phys.*, vol. 83, no. 1, pp. 162–170, Jan. 1998, doi: 10.1063/1.366690.

[36] S. Wirths, R. Geiger, N. von den Driesch, G. Mussler, T. Stoica, S. Mantl, Z. Ikonic, M. Luysberg, S. Chiussi, J. M. Hartmann, H. Sigg, J. Faist, D. Buca, and D. Grützmacher, "Lasing in direct-bandgap GeSn alloy grown on Si," *Nat. Photonics*, vol. 9, no. 2, pp. 88–92, Feb. 2015, doi: 10.1038/nphoton.2014.321.

[37] S. Su, B. Cheng, C. Xue, W. Wang, Q. Cao, H. Xue, W. Hu, G. Zhang, Y. Zuo, and Q. Wang, "GeSn p-i-n photodetector for all telecommunication bands detection," *Opt. Express*, vol. 19, no. 7, p. 6400, Mar. 2011, doi: 10.1364/OE.19.006400.

[38] D. Stange, N. von den Driesch, D. Rainko, S. Roesgaard, I. Povstugar, J.-M. Hartmann, T. Stoica, Z. Ikonic, S. Mantl, D. Grützmacher, and D. Buca, "Short-wave infrared LEDs from GeSn/SiGeSn multiple quantum wells," *Optica*, vol. 4, no. 2, p. 185, Feb. 2017, doi: 10.1364/optica.4.000185.

[39] J. P. Gupta, N. Bhargava, S. Kim, T. Adam, and J. Kolodzey, "Infrared electroluminescence from GeSn heterojunction diodes grown by molecular beam epitaxy," *Appl. Phys. Lett.*, vol. 102, no. 25, p. 251117, Jun. 2013, doi: 10.1063/1.4812747.

[40] J. Xie, A. V. G. Chizmeshya, J. Tolle, V. R. Dcosta, J. Menendez, and J. Kouvetakis, "Synthesis, stability range, and fundamental properties of Si-Ge-Sn semiconductors grown directly on Si(100) and Ge(100) platforms," *Chem. Mater.*, vol. 22, no. 12, pp. 3779–3789, Jun. 2010, doi: 10.1021/cm100915q.

[41] W. A. Harrison, "Electronic Structure and the Properties of Solids - The Physics of the Chemical Bond." Dover Publications, pp. 61–288, [Online]. Available: https://app.knovel.com/hotlink/toc/id:kpESPSTPC1/electronic-structure/electronic-structure.

[42] M. S. Dutta, M. K. Pathak, and P. Mahto, "Bulk modulus of group- IV and its compound semiconductors," *J. Alloys Compd.*, vol. 695, pp. 3547–3551, 2017, doi: https://doi.org/10.1016/j.jallcom.2016.11.415.

[43] E. Kasper and H. J. Herzog, "Structural properties of silicon-germanium (SiGe) nanostructures," in *Silicon-Germanium (SiGe) Nanostructures*, Woodhead Publishing, Cambridge, 2011, pp. 3–25.

[44] J. Hornstra, "Dislocations in the diamond lattice," *J. Phys. Chem. Solids*, vol. 5, no. 1–2, pp. 129–141, Jan. 1958, doi: 10.1016/0022-3697(58)90138-0.

[45] M. Moore, “Diamond: Natural,” Elsevier, 2001, pp. 2133–2143, doi: 10.1016/B0-08-0431 52-6/00385-5.

[46] J. Jeon, T. Asano, Y. Shimura, W. Takeuchi, M. Kurosawa, M. Sakashita, O. Nakatsuka, and S. Zaima, “Effect of in situ Sb doping on crystalline and electrical characteristics of n-type $Ge_{1-x}Sn_x$ epitaxial layer,” *Jpn. J. Appl. Phys.*, vol. 55, no. 4S, p. 04EB13, Apr. 2016, doi: 10.7567/JJAP.55.04EB13.

[47] D. Hull and D. J. Bacon, *Introduction to Dislocations*, 5th ed. Saint Louis: Elsevier Science, 2011, pp. 109–136.

[48] P. Moontragoon, P. Pengpit, T. Burinprakhon, S. Maensiri, N. Vukmirovic, Z. Ikonic, and P. Harrison, “Electronic properties calculation of $Ge_{1-x-y}Si_xSn_y$ ternary alloy and nanostructure,” in *Journal of Non-Crystalline Solids*, Sep. 2012, vol. 358, no. 17, pp. 2096–2098, doi: 10.1016/j.jnoncrysol.2012.01.025.

[49] R. Beeler, R. Roucka, A. V. G. Chizmeshya, J. Kouvetakis, and J. Menéndez, “Nonlinear structure-composition relationships in the $Ge_{1-y}Sn_y$/Si(100) ($y < 0.15$) system,” *Phys. Rev. B*, vol. 84, no. 3, p. 035204, Jul. 2011, doi: 10.1103/PhysRevB.84.035204.

[50] F. Gencarelli, B. Vincent, J. Demeulemeester, A. Vantomme, A. Moussa, A. Franquet, A. Kumar, H. Bender, J. Meersschaut, W. Vandervorst, R. Loo, M. Caymax, K. Temst, and M. Heyns, “Crystalline Properties and Strain Relaxation Mechanism of CVD Grown GeSn,” *ECS J. Solid State Sci. Technol.*, vol. 2, no. 4, pp. P134–P137, Jan. 2013, doi: 10. 1149/2.011304jss.

[51] R. Hull and J. C. Bean, “Misfit Dislocations in Lattice-Mismatched Epitaxial Films,” *Crit. Rev. Solid State Mater. Sci.*, vol. 17, no. 6, pp. 507–546, Jan. 1992, doi: 10.1080/1040843 9208244585.

[52] W. Wegscheider, “Effect of compressive and tensile strain on misfit dislocation injection in SiGe epitaxial layers,” *J. Vac. Sci. Technol. B Microelectron. Nanom. Struct.*, vol. 11, no. 3, p. 1056, May 1993, doi: 10.1116/1.587007.

[53] “One-dimensional dislocations. I. Static theory,” *Proc. R. Soc. London. Ser. A. Math. Phys. Sci.*, vol. 198, no. 1053, pp. 205–216, Aug. 1949, doi: 10.1098/rspa.1949.0095.

[54] J. M. Burgers, U. Dehlinger, J. Frenkel, T. Kontorowa, and R. Garber, “One-dimensional dislocations. II. Misfitting monolayers and oriented overgrowth,” *Proc. R. Soc. London. Ser. A. Math. Phys. Sci.*, vol. 198, no. 1053, pp. 216–225, Aug. 1949, doi: 10.1098/rspa. 1949.0096.

[55] “One-dimensional dislocations - III. Influence of the second harmonic term in the potential representation, on the properties of the model,” *Proc. R. Soc. London. Ser. A. Math. Phys. Sci.*, vol. 200, no. 1060, pp. 125–134, Dec. 1949, doi: 10.1098/rspa.1949.

0163.

[56] J. W. Matthews and A. E. Blakeslee, “Defects in epitaxial multilayers: I. Misfit dislocations,” *J. Cryst. Growth*, vol. 27, pp. 118–125, Dec. 1974, doi: 10.1016/S0022-02 48(74)80055-2.

[57] R. People and J. C. Bean, “Calculation of critical layer thickness versus lattice mismatch for GexSi1−x/Si strained-layer heterostructures,” *Appl. Phys. Lett.*, vol. 47, no. 3, pp. 322–324, 1985, doi: 10.1063/1.96206.

[58] M. A. Moram and M. E. Vickers, “X-ray diffraction of III-nitrides,” *Reports Prog. Phys.*, vol. 72, no. 3, p. 036502, Mar. 2009, doi: 10.1088/0034-4885/72/3/036502.

[59] M. A. Krivoglaz, *Theory of X-ray and thermal-neutron scattering by real crystals*. New York: Plenum Press, 1969, pp. 249–277.

[60] S. Daniš and V. Holý, “Diffuse x-ray scattering from misfit and threading dislocations in PbTe/$BaF_2$/Si (111) thin layers,” *Phys. Rev. B*, vol. 73, no. 1, p. 014102, Jan. 2006, doi: 10.1103/PhysRevB.73.014102.

[61] V. M. Kaganer, R. Köhler, M. Schmidbauer, R. Opitz, and B. Jenichen, “X-ray diffraction peaks due to misfit dislocations in heteroepitaxial structures,” *Phys. Rev. B*, vol. 55, no. 3, pp. 1793–1810, Jan. 1997, doi: 10.1103/PhysRevB.55.1793.

[62] V. S. Kopp, V. M. Kaganer, G. Capellini, M. De Seta, and P. Zaumseil, “X-ray diffraction study of plastic relaxation in Ge-rich SiGe virtual substrates,” *Phys. Rev. B*, vol. 85, no. 24, p. 245311, Jun. 2012, doi: 10.1103/PhysRevB.85.245311.

[63] W. Dou, M. Benamara, A. Mosleh, J. Margetis, P. Grant, Y. Zhou, S. Al-Kabi, W. Du, J. Tolle, B. Li, M. Mortazavi, and S.-Q. Yu, “Investigation of GeSn Strain Relaxation and Spontaneous Composition Gradient for Low-Defect and High-Sn Alloy Growth,” *Sci. Rep.*, vol. 8, no. 1, p. 5640, Dec. 2018, doi: 10.1038/s41598-018-24018-6.

[64] P. F. Fewster, *X-ray Scattering from Semiconductors*. 2nd ed. London: Imperial College Press, 2003, pp. 108–111.

[65] C. Ferrari and C. Bocchi, “Strain and composition determination in semiconducting heterostructures by high-resolution x-ray diffraction,” in *Characterization of Semiconductor Heterostructures and Nanostructures*, Elsevier, 2008, pp. 93–132.

[66] M. Albani, S. Assali, M. A. Verheijen, S. Koelling, R. Bergamaschini, F. Pezzoli, E. P. A. M. Bakkers, and L. Miglio, “Critical strain for Sn incorporation into spontaneously graded Ge/GeSn core/shell nanowires,” *Nanoscale*, vol. 10, no. 15, pp. 7250–7256, Apr. 2018, doi: 10.1039/c7nr09568f.

[67] P. M. Mooney, F. K. LeGoues, J. Tersoff, and J. O. Chu, “Nucleation of dislocations in

SiGe layers grown on (001)Si," *J. Appl. Phys.*, vol. 75, no. 8, pp. 3968–3977, Apr. 1994, doi: 10.1063/1.356992.

[68] V. Srikant, J. S. Speck, and D. R. Clarke, "Mosaic structure in epitaxial thin films having large lattice mismatch," *J. Appl. Phys.*, vol. 82, no. 9, p. 4286, Nov. 1997, doi: 10.1063/1.366235.

[69] H. F. Liu, L. Zhang, S. J. Chua, and D. Z. Chi, "Crystallographic tilt in GaN-on-Si (111) heterostructures grown by metal–organic chemical vapor deposition," *J. Mater. Sci.*, vol. 49, no. 9, pp. 3305–3313, Jan. 2014, doi: 10.1007/s10853-014-8025-6.

[70] J. Aubin, J. M. Hartmann, A. Gassenq, J. L. Rouviere, E. Robin, V. Delaye, D. Cooper, N. Mollard, V. Reboud, and V. Calvo, "Growth and structural properties of step-graded, high Sn content GeSn layers on Ge," *Semicond. Sci. Technol.*, vol. 32, no. 9, p. 094006, Sep. 2017, doi: 10.1088/1361-6641/aa8084.

[71] H. Stanchu, A. V Kuchuk, Y. I. Mazur, J. Margetis, J. Tolle, J. Richter, S.-Q. Yu, and G. J. Salamo, "X-ray diffraction study of strain relaxation, spontaneous compositional gradient, and dislocation density in GeSn/Ge/Si(100) heterostructures," *Semicond. Sci. Technol.*, vol. 35, no. 7, p. 075009, Jul. 2020, doi: 10.1088/1361-6641/ab883c.

[72] T. Liu, L. Wang, G. Zhu, X. Hu, Z. Dong, Z. Zhong, Q. Jia, X. Yang, and Z. Jiang, "Dislocation-related photoluminescence of GeSn films grown on Ge (001) substrates by molecular beam epitaxy," *Semicond. Sci. Technol.*, vol. 33, no. 12, p. 125022, Dec. 2018, doi: 10.1088/1361-6641/aaed82.

[73] T. Ulyanenkova, M. Myronov, A. Benediktovitch, A. Mikhalychev, J. Halpin, A. Ulyanenkov, and IUCr, "Characterization of SiGe thin films using a laboratory X-ray instrument," *J. Appl. Crystallogr.*, vol. 46, no. 4, pp. 898–902, Aug. 2013, doi: 10.1107/S0021889813010492.

[74] H. V. Stanchu, A. V. Kuchuk, Y. I. Mazur, J. Margetis, J. Tolle, S.-Q. Yu, and G. J. Salamo, "Strain suppressed Sn incorporation in GeSn epitaxially grown on Ge/Si(001) substrate," *Appl. Phys. Lett.*, vol. 116, no. 23, p. 232101, Jun. 2020, doi: 10.1063/5.0011842.

[75] A. Rockett, T. J. Drummond, J. E. Greene, and H. Morkoc, "Surface segregation model for Sn-doped GaAs grown by molecular beam epitaxy," *J. Appl. Phys.*, vol. 53, no. 10, pp. 7085–7087, Oct. 1982, doi: 10.1063/1.330013.

[76] W. Wang, Q. Zhou, Y. Dong, E. S. Tok, and Y.-C. Yeo, "Critical thickness for strain relaxation of $Ge_{1-x}Sn_x$ ($x \leq 0.17$) grown by molecular beam epitaxy on Ge(001)," *Appl. Phys. Lett.*, vol. 106, no. 23, p. 232106, 2015, doi: 10.1063/1.4922529.

[77] N. Von Den Driesch, S. Wirths, R. Troitsch, G. Mussler, U. Breuer, O. Moutanabbir, D. Grützmacher, and D. Buca, "Thermally activated diffusion and lattice relaxation in

(Si)GeSn materials," *Phys. Rev. Mater.*, vol. 4, no. 3, p. 033604, Mar. 2020, doi: 10.1103/PhysRevMaterials.4.033604.

[78] B. Vincent, F. Gencarelli, H. Bender, C. Merckling, B. Douhard, D. H. Petersen, O. Hansen, H. H. Henrichsen, J. Meersschaut, W. Vandervorst, M. Heyns, R. Loo, and M. Caymax, "Undoped and in-situ B doped GeSn epitaxial growth on Ge by atmospheric pressure-chemical vapor deposition," *Appl. Phys. Lett.*, vol. 99, no. 15, p. 152103, Oct. 2011, doi: 10.1063/1.3645620.

[79] H. Li, Y. X. Cui, K. Y. Wu, W. K. Tseng, H. H. Cheng, and H. Chen, "Strain relaxation and Sn segregation in GeSn epilayers under thermal treatment," *Appl. Phys. Lett.*, vol. 102, no. 25, p. 251907, Jun. 2013, doi: 10.1063/1.4812490.

[80] P. Zaumseil, Y. Hou, M. A. Schubert, N. Von Den Driesch, D. Stange, D. Rainko, M. Virgilio, D. Buca, and G. Capellini, "The thermal stability of epitaxial GeSn layers," *APL Mater.*, vol. 6, no. 7, p. 076108, Jul. 2018, doi: 10.1063/1.5036728.

[81] J. Nicolas, S. Assali, S. Mukherjee, A. Lotnyk, and O. Moutanabbir, "Dislocation Pipe Diffusion and Solute Segregation during the Growth of Metastable GeSn," *Cryst. Growth Des.*, vol. 20, no. 5, pp. 3493–3498, May 2020, doi: 10.1021/acs.cgd.0c00270.

[82] H. V Stanchu, A. V Kuchuk, Y. I. Mazur, K. Pandey, F. M. de Oliveira, M. Benamara, M. D. Teodoro, S.-Q. Yu, and G. J. Salamo, "Quantitative Correlation Study of Dislocation Generation, Strain Relief, and Sn Outdiffusion in Thermally Annealed GeSn Epilayers," *Cryst. Growth Des.*, Jan. 2021, doi: 10.1021/acs.cgd.0c01525.

[83] M. Albrecht, S. Christiansen, J. Michler, W. Dorsch, H. P. Strunk, P. O. Hansson, and E. Bauser, "Surface ripples, crosshatch pattern, and dislocation formation: Cooperating mechanisms in lattice mismatch relaxation," *Appl. Phys. Lett.*, vol. 67, no. 9, p. 1232, Aug. 1995, doi: 10.1063/1.115017.

[84] E. A. Fitzgerald, "Relaxed $Ge_xSi_{1-x}$ structures for III–V integration with Si and high mobility two-dimensional electron gases in Si," *J. Vac. Sci. Technol. B Microelectron. Nanom. Struct.*, vol. 10, no. 4, p. 1807, Jul. 1992, doi: 10.1116/1.586204.

[85] V. R. D'Costa, J. Tolle, R. Roucka, C. D. Poweleit, J. Kouvetakis, and J. Menéndez, "Raman scattering in Ge1-ySny alloys," *Solid State Commun.*, vol. 144, no. 5–6, pp. 240–244, Nov. 2007, doi: 10.1016/j.ssc.2007.08.020.

[86] T. S. Perova, E. Kasper, M. Oehme, S. Cherevkov, and J. Schulze, "Features of polarized Raman spectra for homogeneous and non-homogeneous compressively strained $Ge_{1-y}Sn_y$ alloys," *J. Raman Spectrosc.*, vol. 48, no. 7, pp. 993–1001, 2017, doi: 10.1002/jrs.5160.

[87] É. Bouthillier, S. Assali, J. Nicolas, and O. Moutanabbir, "Decoupling the effects of composition and strain on the vibrational modes of GeSn semiconductors," *Semicond. Sci. Technol.*, vol. 35, no. 9, p. 095006, Sep. 2020, doi: 10.1088/1361-6641/ab9846.

[88] R. Roucka, Y.-Y. Fang, J. Kouvetakis, A. V. G. Chizmeshya, and J. Menéndez, “Thermal expansivity of $Ge_{1-y}Sn_y$ alloys,” *Phys. Rev. B*, vol. 81, no. 24, p. 245214, Jun. 2010, doi: 10.1103/PhysRevB.81.245214.

[89] M. S. Titus, R. K. Rhein, P. B. Wells, P. C. Dodge, G. B. Viswanathan, M. J. Mills, A. Van Der Ven, and T. M. Pollock, “Solute segregation and deviation from bulk thermodynamics at nanoscale crystalline defects,” *Sci. Adv.*, vol. 2, no. 12, p. e1601796, Dec. 2016, doi: 10.1126/sciadv.1601796.

[90] R. Kirchheim, “Reducing grain boundary, dislocation line and vacancy formation energies by solute segregation. II. Experimental evidence and consequences,” *Acta Mater.*, vol. 55, no. 15, pp. 5139–5148, Sep. 2007, doi: 10.1016/j.actamat.2007.05.033.

[91] V. Kaganer, T. Ulyanenkova, A. Benediktovitch, M. Myronov, and A. Ulyanenkov, “Bunches of misfit dislocations on the onset of relaxation of Si0.4Ge0.6/Si(001) epitaxial films revealed by high-resolution x-ray diffraction,” *J. Appl. Phys.*, vol. 122, no. 10, p. 105302, Sep. 2017, doi: 10.1063/1.4990135.

[92] M. El Kurdi, T. Kociniewski, T.-P. Ngo, J. Boulmer, D. Débarre, P. Boucaud, J. F. Damlencourt, O. Kermarrec, and D. Bensahel, “Enhanced photoluminescence of heavily n-doped germanium,” *Appl. Phys. Lett.*, vol. 94, no. 19, p. 191107, May 2009, doi: 10.106 3/1.3138155.

[93] T. Amotchkina, M. Trubetskov, D. Hahner, and V. Pervak, “Characterization of e-beam evaporated Ge, YbF3, ZnS, and LaF3 thin films for laser-oriented coatings,” *Appl. Opt.*, vol. 59, no. 5, pp. A40--A47, Feb. 2020, doi: 10.1364/AO.59.000A40.

[94] F. Pezzoli, A. Giorgioni, D. Patchett, and M. Myronov, “Temperature-Dependent Photoluminescence Characteristics of GeSn Epitaxial Layers,” *ACS Photonics*, vol. 3, no. 11, pp. 2004–2009, Nov. 2016, doi: 10.1021/acsphotonics.6b00438.

[95] Y.-C. Tai, P.-L. Yeh, S. An, H.-H. Cheng, M. Kim, and G.-E. Chang, “Strain-free GeSn nanomembranes enabled by transfer-printing techniques for advanced optoelectronic applications,” *Nanotechnology*, vol. 31, no. 44, p. 445301, Oct. 2020, doi: 10.1088/1361-6528/aba6b1.

[96] J. R. Jain, A. Hryciw, T. M. Baer, D. A. B. Miller, M. L. Brongersma, and R. T. Howe, “A micromachining-based technology for enhancing germanium light emission via tensile strain,” *Nat. Photonics*, vol. 6, no. 6, pp. 398–405, 2012, doi: 10.1038/nphoton.2012.111.

Appendix A: Description of Research for Popular Publication

## Estimation of chemical composition and deformation at nanoscale

At present days, silicon is the key element for most electronic devices, partly owing to its semiconducting properties and the fact that silicon is the second most abundant element on the Earth's crust. Over the years silicon technology was advancing at a fast pace, which ultimately resulted in low-cost manufacturing and affordable electronics. At the same time, silicon exhibits poor optical properties that hinder its prospects for active photonic devices, which include light emitting and sensing applications. There are many other materials with excellent optical properties. For example, such materials as gallium arsenide (GaAs), gallium phosphide (GaP), as well as their alloys, have been extensively used for light-emitting applications. Nonetheless, their integration with silicon electronics is cumbersome since these are chemically dissimilar materials.

From the point of view of electron configuration, germanium and tin are similar to silicon. Moreover, the addition of Sn atoms into germanium crystal was shown to result in alloys with improved optical properties. Accordingly, the optoelectronic devices based on Si, Ge, and Sn can be monolithically integrated. In particular, these are suitable for photonic devices operating in the mid-infrared spectral region.

Nowadays, optoelectronics is based on harnessing the properties that occur in materials of nanoscale dimensions, which practically allows tunable mechanical, optical, and electronic properties as a function of size. Therefore, developing techniques for nanostructural analysis is indispensable for material growth and device fabrication.

X-ray diffraction is an established technique for rapid and non-destructive structural

characterization of crystalline materials and was used in this work extensively. X-rays are high-energy light with a wavelength of the order on the distance between the atoms in a solid. Accordingly, X-ray diffraction unambiguously provides the atomic distances. Moreover, since the atomic distance is proportional to the atomic radius and the applied strain, X-ray diffraction analysis additionally delivers precise information about the chemical composition and the strain state of an alloy. Therefore, in this dissertation X-ray diffraction methods were applied to study the incorporation of Sn into compressively strained GeSn alloys as well as their structural stability during the thermal treatment, which is important from the point of view of material growth and device processing.

Appendix B: Executive Summary of Newly Created Intellectual Property

Germanium-tin alloys with the Sn content above 8 at. % were extensively studied as prospective quasi direct bandgap semiconductors for optoelectronics on Si substrate. The bandgap directness of GeSn was tightly correlated to the alloy composition and the strain state, which has an ultimate effect on the optical properties. The structural stability of GeSn under annealing treatment was correlated with the Sn segregation, strain relaxation, and the density of defects. The major results obtained in the course of this research are summarized below.

1. Experimental and theoretical X-ray diffraction analysis was demonstrated as a precise and non-destructive technique for the rapid assessment of the chemical composition, strain state, and density of defects in GeSn alloys.
2. The suppressed Sn incorporation in the GeSn layers during the epitaxial growth on Ge was quantitatively correlated to the built-in compressive strain.
3. The structural stability of the GeSn layer under thermal treatment was quantitatively correlated with the density of misfit/threading dislocations. A critical density of misfit dislocations of $2 \times 10^5$ $cm^{-1}$ was found responsible for the onset of Sn segregation.
4. It was shown that the annealing treatment of compressively strained indirect bandgap GeSn layers results in a more enhanced photoluminescence emission for the GeSn layers with a lower L to Γ energy separation.

## Appendix C: Potential Patent and Commercialization Aspects of Listed Intellectual Property Items

### C.1 Patentability of Intellectual Property

The four items listed were considered first from the perspective of whether or not the item could be patented.

1. The X-ray diffraction method developed in this research to measure the chemical composition, strain state, and density of misfit dislocations in the GeSn/Ge/Si(001) heterostructures cannot be patented since it is well known and extensively used for other material systems.
2. The effect of suppressed Sn incorporation in the GeSn layers during the epitaxial growth cannot be patented because it occurs naturally and is not an invention.
3. The discussed role of misfit/threading dislocations on structural stability of the GeSn layer under thermal treatment cannot be patented as a phenomenom.
4. The correlation of annealing treatment of compressively strained indirect bandgap GeSn layers with the enhanced photoluminescence emission is also a naturally occurring phenomenon that cannot be patented. A process based on the demonstrated phenomenon is yet to be developed.

### C.2 Commercialization Prospects

The four items listed were then considered from the perspective of whether or not the item should be patented.

1. The X-ray diffraction method developed in this research should not be patented since

it does not represent commercial opportunity.

2. NA.

3. NA.

4. NA.

C.3 Possible Prior Disclosure of IP

The following items have published information that could impact the patentability of the listed IP.

1. This X-ray diffraction method developed in this research to measure the chemical composition, strain state, and density of misfit dislocations in the GeSn/Ge/Si(001) heterostructures was published in:

   H. Stanchu, A. V Kuchuk, Y. I. Mazur, J. Margetis, J. Tolle, J. Richter, S.-Q. Yu, and G. J. Salamo, "X-ray diffraction study of strain relaxation, spontaneous compositional gradient, and dislocation density in GeSn/Ge/Si(100) heterostructures," *Semicond. Sci. Technol.*, vol. 35, no. 7, p. 075009, Jul. 2020, doi: 10.1088/1361-6641/ab883c.

2. The effect of suppressed Sn incorporation in the GeSn layers during the epitaxial growth was published in:

   H. V. Stanchu, A. V. Kuchuk, Y. I. Mazur, J. Margetis, J. Tolle, S.-Q. Yu, and G. J. Salamo, "Strain suppressed Sn incorporation in GeSn epitaxially grown on Ge/Si(001) substrate," *Appl. Phys. Lett.*, vol. 116, no. 23, p. 232101, Jun. 2020, doi: 10.1063/5.0011842.

3. The role of misfit/threading dislocations on structural stability of the GeSn layer under thermal treatment was published in:

   H. V Stanchu, A. V Kuchuk, Y. I. Mazur, K. Pandey, F. M. de Oliveira, M. Benamara, M. D. Teodoro, S.-Q. Yu, and G. J. Salamo, "Quantitative Correlation Study of Dislocation Generation, Strain Relief, and Sn Outdiffusion in Thermally Annealed GeSn Epilayers," *Cryst. Growth Des.*, vol. 21, no. 3, p. 1666-1673, Jan. 2021, doi: 10.1021/acs.cgd.0c01525.

4. The correlation of annealing treatment of compressively strained indirect bandgap GeSn layers with the enhanced photoluminescence emission will be published in the future.

Appendix E: Microsoft Project for PhD MicroEP Degree Plan

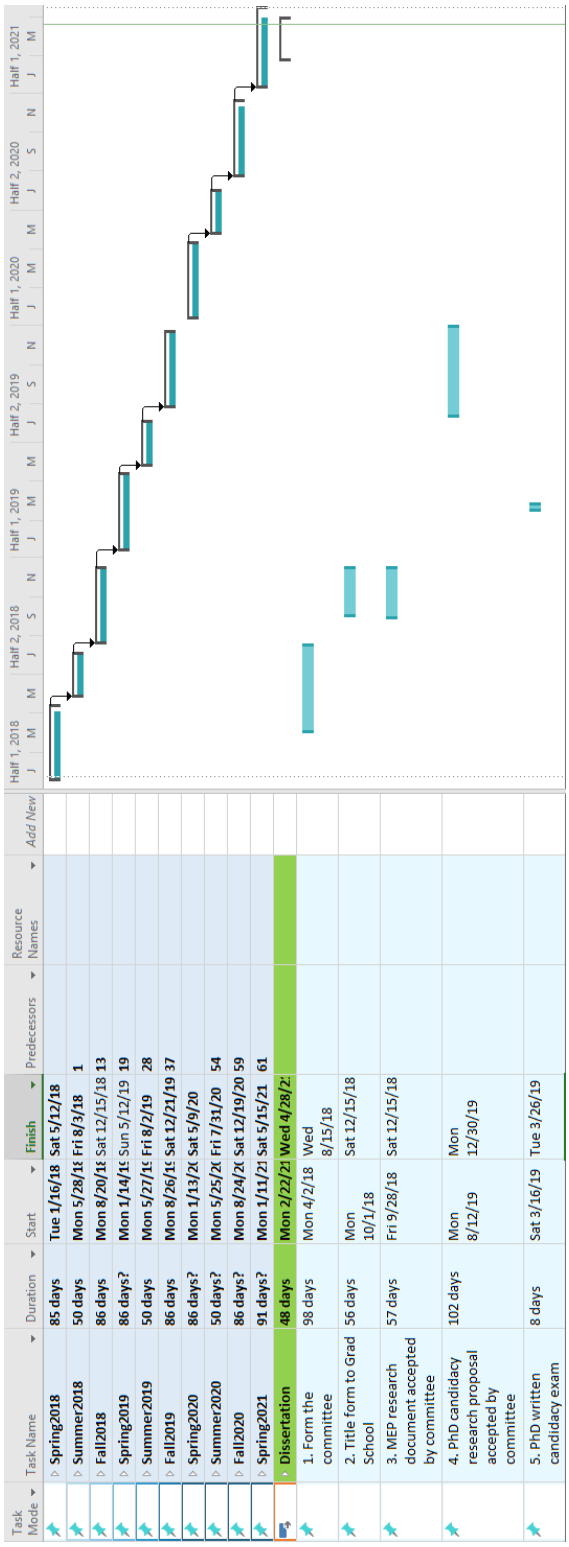

| Task Mode | Task Name | Duration | Start | Finish | Predecessors | Resource Names | Add New |
|---|---|---|---|---|---|---|---|
| | Spring2018 | 85 days | Tue 1/16/18 | Sat 5/12/18 | | | |
| | Summer2018 | 50 days | Mon 5/28/18 | Fri 8/3/18 | 1 | | |
| | Fall2018 | 86 days | Mon 8/20/18 | Sat 12/15/18 | 13 | | |
| | Spring2019 | 86 days? | Mon 1/14/19 | Sun 5/12/19 | 19 | | |
| | Summer2019 | 50 days | Mon 5/27/19 | Fri 8/2/19 | 28 | | |
| | Fall2019 | 86 days | Mon 8/26/19 | Sat 12/21/19 | 37 | | |
| | Spring2020 | 86 days? | Mon 1/13/20 | Sat 5/9/20 | | | |
| | Summer2020 | 50 days? | Mon 5/25/20 | Fri 7/31/20 | 54 | | |
| | Fall2020 | 86 days? | Mon 8/24/20 | Sat 12/19/20 | 59 | | |
| | Spring2021 | 91 days? | Mon 1/11/21 | Sat 5/15/21 | 61 | | |
| | Dissertation | 48 days | Mon 2/22/21 | Wed 4/28/2 | | | |
| | 1. Form the committee | 98 days | Mon 4/2/18 | Wed 8/15/18 | | | |
| | 2. Title form to Grad School | 56 days | Mon 10/1/18 | Sat 12/15/18 | | | |
| | 3. MEP research document accepted by committee | 57 days | Fri 9/28/18 | Sat 12/15/18 | | | |
| | 4. PhD candidacy research proposal accepted by committee | 102 days | Mon 8/12/19 | Mon 12/30/19 | | | |
| | 5. PhD written candidacy exam | 8 days | Sat 3/16/19 | Tue 3/26/19 | | | |

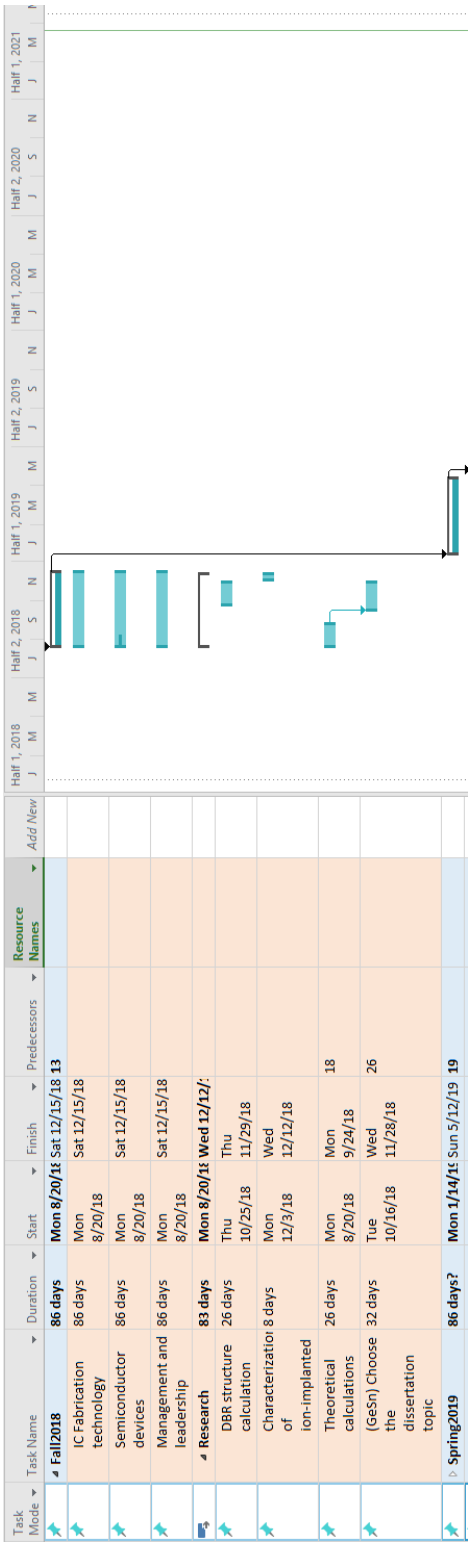

| Task Mode | Task Name | Duration | Start | Finish | Predecessors | Resource Names | Add New |
|---|---|---|---|---|---|---|---|
| | Fall2018 | 86 days | Mon 8/20/18 | Sat 12/15/18 | 13 | | |
| | IC Fabrication technology | 86 days | Mon 8/20/18 | Sat 12/15/18 | | | |
| | Semiconductor devices | 86 days | Mon 8/20/18 | Sat 12/15/18 | | | |
| | Management and leadership | 86 days | Mon 8/20/18 | Sat 12/15/18 | | | |
| | Research | 83 days | Mon 8/20/18 | Wed 12/12/: | | | |
| | DBR structure calculation | 26 days | Thu 10/25/18 | Thu 11/29/18 | | | |
| | Characterizatio of ion-implanted | 8 days | Mon 12/3/18 | Wed 12/12/18 | | | |
| | Theoretical calculations | 26 days | Mon 8/20/18 | Mon 9/24/18 | 18 | | |
| | (GeSn) Choose the dissertation topic | 32 days | Tue 10/16/18 | Wed 11/28/18 | 26 | | |
| | Spring2019 | 86 days? | Mon 1/14/19 | Sun 5/12/19 | 19 | | |

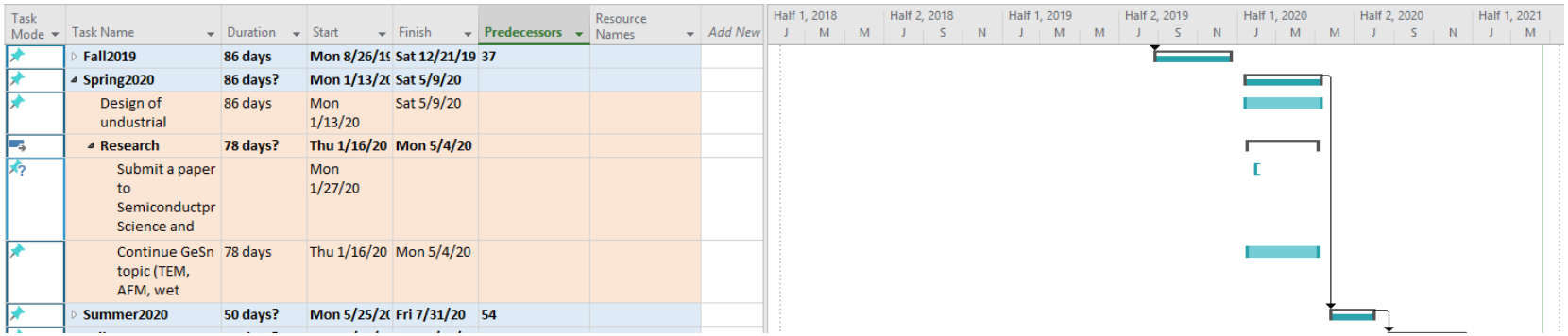

| Task Mode | Task Name | Duration | Start | Finish | Predecessors | Resource Names | Add New |
|---|---|---|---|---|---|---|---|
| | **Fall2019** | **86 days** | **Mon 8/26/19** | **Sat 12/21/19** | **37** | | |
| | **Spring2020** | **86 days?** | **Mon 1/13/20** | **Sat 5/9/20** | | | |
| | Design of undustrial | 86 days | Mon 1/13/20 | Sat 5/9/20 | | | |
| | **Research** | **78 days?** | **Thu 1/16/20** | **Mon 5/4/20** | | | |
| | Submit a paper to Semiconductpr Science and | | Mon 1/27/20 | | | | |
| | Continue GeSn topic (TEM, AFM, wet | 78 days | Thu 1/16/20 | Mon 5/4/20 | | | |
| | **Summer2020** | **50 days?** | **Mon 5/25/20** | **Fri 7/31/20** | **54** | | |

Appendix F: Identification of All Software Used in Research and Dissertation Generation

Computer #1:
- Model Number: Dell Optiplex 9010
- Serial Number: 7038090
- Location: NANO213B
- Owner: Hryhorii Stanchu

Software #1:
- Name: Microsoft Office 365
- Purchased by: University of Arkansas Site License

Software #2:
- Name: Matlab R2018b
- Purchased by: University of Arkansas Site License

Software #3:
- Name: 3ds Max 2019
- Purchased by: University of Arkansas Site License

Software #4:
- Name: Vesta ver. 3.5.2
- Purchased by: free of charge

Software #5:
- Name: Mendeley Desktop ver. 1.19.4
- Purchased by: free of charge

Appendix G: All Publications Published, Submitted and Planned

Published


[1] **H. V Stanchu**, A. V Kuchuk, Y. I. Mazur, K. Pandey, F. M. de Oliveira, M. Benamara, M. D. Teodoro, S.-Q. Yu, and G. J. Salamo, "Quantitative Correlation Study of Dislocation Generation, Strain Relief, and Sn Outdiffusion in Thermally Annealed GeSn Epilayers," *Cryst. Growth Des.*, vol. 21, no. 3, p. 1666-1673, Jan. 2021, doi: 10.1021/acs.cgd.0c01525.

[2] S. V Kondratenko, S. S. Derenko, Y. I. Mazur, **H. Stanchu**, A. V Kuchuk, V. S. Lysenko, P. M. Lytvyn, S.-Q. Yu, and G. J. Salamo, "Impact of defects on photoexcited carrier relaxation dynamics in GeSn thin films," *J. Phys. Condens. Matter*, vol. 33, no. 6, p. 065702, Feb. 2020, doi: 10.1088/1361-648X/abc4ce.

[3] S. K. Saha, R. Kumar, A. Kuchuk, **H. Stanchu**, Y. I. Mazur, S.-Q. Yu, and G. J. Salamo, "GaAs epitaxial growth on R-plane sapphire substrate," *J. Cryst. Growth*, vol. 548, p. 125848, 2020, doi: https://doi.org/10.1016/j.jcrysgro.2020.125848.

[4] **H. Stanchu**, A. V Kuchuk, Y. I. Mazur, J. Margetis, J. Tolle, J. Richter, S.-Q. Yu, and G. J. Salamo, "X-ray diffraction study of strain relaxation, spontaneous compositional gradient, and dislocation density in GeSn/Ge/Si(100) heterostructures," *Semicond. Sci. Technol.*, vol. 35, no. 7, p. 075009, Jul. 2020, doi: 10.1088/1361-6641/ab883c.

[5] **H. V. Stanchu**, A. V. Kuchuk, Y. I. Mazur, J. Margetis, J. Tolle, S.-Q. Yu, and G. J. Salamo, "Strain suppressed Sn incorporation in GeSn epitaxially grown on Ge/Si(001) substrate," *Appl. Phys. Lett.*, vol. 116, no. 23, p. 232101, Jun. 2020, doi: 10.1063/5.0011842.

[6] P. K. Ghosh, **H. V Stanchu**, Y. Maidaniuk, M. Sarollahi, M. Aldawsari, A. V Kuchuk, Y. I. Mazur, G. J. Salamo, and M. E. Ware, "Investigation of the Structural and Optical Properties of Compositionally V-Graded Strained $In_xGa_{1-x}N$ Layers," *Phys. status solidi*, vol. 257, no. 4, p. 1900591, Apr. 2020, doi: https://doi.org/10.1002/pssb.201900591.

[7] **H. Stanchu**, M. Auf der Maur, A. V Kuchuk, Y. I. Mazur, M. Sobanska, Z. R. Zytkiewicz, S. Wu, Z. Wang, and G. Salamo, "Compositionally Graded AlGaN Nanostructures: Strain Distribution and X-ray Diffraction Reciprocal Space Mapping," *Cryst. Growth Des.*, vol. 20, no. 3, pp. 1543–1551, Mar. 2020, doi: 10.1021/acs.cgd.9b01273.

[8] O. I. Liubchenko, V. P. Kladko, **H. V. Stanchu**, T. M. Sabov, V. P. Melnik, S. B. Kryvyi, and A. E. Belyaev, "The effect of ion implantation on structural damage in compositionally graded AlGaN layers," *Semicond. Physics, Quantum Electron. Optoelectron.*, vol. 22, no. 1, 2019, doi: 10.15407/spqeo22.01.119.

[9] **H. V. Stanchu**, A. V. Kuchuk, Y. I. Mazur, C. Li, P. M. Lytvyn, M. Schmidbauer, Y. Maidaniuk, M. Benamara, M. E. Ware, Z. M. Wang, and G. J. Salamo, "Local Strain and Crystalline Defects in GaN/AlGaN/GaN(0001) Heterostructures Induced by Compositionally Graded AlGaN Buried Layers," *Cryst. Growth Des.*, vol. 19, no. 1, 2019, doi: 10.1021/acs.cgd.8b01267.

Planned

[10] Oluwatobi Olorunsola, **Hryhorii Stanchu**, Solomon Ojo, Krishna Pandey, Joe Margetis, John Tolle, Andrian Kuchuk, Yuriy I. Mazur, Gregory Salamo, and Shui-Qing Yu, "Effects of annealing-induced strain on GeSn indirect-to-direct bandgap optical transition".